Three Dimensional Coherent Photoemission Spectroscopy

by

Cong Wang

B. S. in Department of Physics, Jilin University, China, 2010

M. S. in Department of Physics, University of Pittsburgh, United States, 2011

Submitted to the Graduate Faculty of

The Dietrich School of Arts and Sciences in partial fulfillment

of the requirements for the degree of

Doctor of Philosophy

University of Pittsburgh

2017

UNIVERSITY OF PITTSBURGH

THE DIETRICH SCHOOL OF ARTS AND SCIENCES

This thesis was presented

by

Cong Wang

It was defended on

March 31, 2017

and approved by

Hrvoje Petek, Professor, Department of Physics and Astronomy

Tao Han, Professor, Department of Physics and Astronomy

David Snoke, Professor, Department of Physics and Astronomy

Daniel Boyanovsky, Professor, Department of Physics and Astronomy

Sean Alexander Garrett-Roe, Assistant Professor, Department of Chemistry

Thesis Advisor: Hrvoje Petek, Professor, Department of Physics and Astronomy

THREE DIMENSIONAL COHERENT PHOTOEMISSIOIN SPECTROSCOPY

Cong Wang, PhD

University of Pittsburgh, 2017

We integrate interferometric time-delay scanning with angle/momentum resolved photoemission spectroscopy to enable three-dimensional coherent electronic spectroscopy. We apply the method to study optical response of clean and alkali atom modified metal surfaces. The interferometric measurements probe the coherent optical response, which are embodied in coherent polarization oscillations. By Fourier transforming the coherent response, we obtain 2D electronic spectra, which map the dynamical relationship between the coherent polarization in the sample and the multiphoton photoemission spectrum. Also, we apply Optical Bloch Equations as a framework for simulating the coherent polarization dynamics in multiphoton photoemission processes.

With wide-range-wavelength-tunable ultrashort pulse laser, we have found several interesting phenomena. Though bound states like excitons cannot exist in metals due to the strong screening of Coulomb interaction, we find the first experimental evidence of a transient exciton, which exists on Ag(111) surface before screening fully established. Furthermore, the interferometric measurements show that an internal polarization field established by the two-photon resonance between the Shockley (SS) and image potential (IP) surface states dominates the surface response, rather than the external laser field.

On Cu(111), we observe abnormal line shapes of SS state, when laser spectrum overlaps with interband transitions from the top d-bands to the sp-band crossing with the Fermi level. This interband transition creates a polarization field, which builds up with time to sufficient strength to co-excite photoelectrons with external laser field. The same interband polarization causes distortions of the IP state on Cu(100) when the IP state can mediate the multiphoton photoemission process. The energy dependence of hole lifetimes causes the asymmetry of IP state line shape.

Lastly, we model coherent surface processes in multi-electron transitions that are excited in three-photon photoemission via the valence *n*s state of chemisorbed alkali atoms on Cu(111) surface. The two-photon excitation of the *n*s state causes coherent beating at fractional photon frequencies that results from screening-induced multi-electron transitions. The simulation reproduces the experiment in a model where the Coulomb interaction creates local polarization fields associated with transition from the SS state to both the *n*s state and the Fermi level.

TABLE OF CONTENTS

LIST OF FIGURES

LIST OF ABBREVIATIONS

fcc: face-centered cubic

USP: upper sp-bands

LSP: upper sp-bands

SS: Shockley Surface State

IP: Image Potential State

mPP: multi-photon photoemission

ITR-mPP: interferometric time-resolved multiphoton photoemission

NOPA: noncollinear optical parametric amplifier

UHV: ultra-high vacuum

ARPES: angle-resolved photoemission spectroscopy

3DCPES: three dimensional coherent photoemission spectroscopy

fs: femtosecond

SHG: second harmonic generation

SFG: sum frequency generation

BBO: beta-barium borate

o-light: ordinary light

e-light: extraordinary light

SH: second harmonic

TH: third harmonic

WL: white light

MZI: Mach-Zehnder Interferometer

as: attosecond

DLD: delay-line detector

MCP: microchannel plate

ROI: range of interest

API: Application Program Interface

IAC: interferometric autocorrelation

TE: Transient Exciton

CR: count rate

ST1: Slit 1

ST2: Slit 2

VI: virtual instrument

WF: work function

ME: multi-electron

PUBLICATIONS

1. Xuefeng Cui, Cong Wang, Adam Argondizzo, Sean Garrett-Roe, Branko Gumhalter and Hrvoje Petek, “Transient Excitons at Metal Surfaces”, *Nature Phys.* 10, 505 (2014)

2. Adam Argondizzo, Xuefeng Cui, Cong Wang, Huijuan Sun, Honghui Shang, Jin Zhao and Hrvoje Petek, “Ultrafast Multiphoton Pump-Probe Photoemission Excitation Pathways in Rutile TiO_2(110)”, *Phys. Rev. B* 91, 155429 (2015)

3. Shengmin Zhang, Cong Wang, Xuefeng Cui, Yanan Wang, Adam Argondizzo, Jin Zhao and Hrvoje Petek, “Time-Resolved Photoemission Study of the Electronic Structure and Dynamics of Chemisorbed Alkali Atoms on Ru(0001)”, *Phys. Rev. B* 93, 045401 (2016)

4. Shijing Tan, Adam Argondizzo, Cong Wang, Xuefeng Cui, and Hrvoje Petek, “Ultrafast Multiphoton Thermionic Photoemission from Graphite”, *Phys. Rev. X* 7, 011004, (2017)

5. Shengmin Zhang, Cong Wang, Hrvoje Petek, “Attosecond Multi-Electron Coulomb Dynamics in Photoinduced Surface Charge Transfer”, (in Preparation)

ACKNOWLEDGEMENT

I have received valuable help from many people during my Ph.D. research, and I could not have achieved this without their supports. Firstly, my thanks go to all members of my thesis committee: Dr. Hrvoje Petek, Dr. Sean Garrett-Roe, Dr. Han Tao, Dr. David Snoke, and Dr. Daniel Boyanovsky, for their guidance and supervision, encouragement and criticism to make my work possible and make my work better. Especially, I would like to express my sincere gratitude to my advisor Dr. Petek, for his continuous guidance from experiments to theories, and for his motivation and dedication. And I also would like to thank Dr. Garrett-Roe, for his valuable tutoring on data analysis and beneficial discussions.

I also appreciate all the support from my lab mates. It is a wonderful experience to learn with them, work with them, and share joys of discoveries with them. I would like to thank Dr. Xuefeng Cui for his tutoring in experimental skills, and cooperation in discovering. I would like to thank Dr. Shengmin Zhang, for her introducing me to this lab, and collaboration in experiments. I would like to thank Dr. Adam Argondizzo for his helping in laser techniques. Also, I would like to thank Dr. Leiming Wang, Dr. Jin Zhao, Dr. Min Feng, Dr. Qiang Zou, Dr. Tian Huang, Dr. Shijing Tan, Dr. Jindong Ren, and Dr. Maciej Krzysztof Dabrowski, for the discussions, encouragement, and models in being a physicist.

Last but not least, I would like to thank my family, particularly my wife, my parents, and my parents in-law. Their support and encouragement are the spiritual energy and momentum for me to finish this work.

1.0 INTRODUCTION

The topic of this dissertation is the dynamical optical response[1–3] of charge carriers in noble metal surfaces, upon the sudden turning-on of external optical field. At the instant of excitation the charge carriers respond to the field instantaneously and coherently, but their time evolution is determined by their natural resonant frequencies and interactions with the environment, which cause decoherence[4–8] and energy relaxation[9–13]. These fundamental responses are very important for many optical and electronic properties of solid state materials, such as the dielectric response[14], transport[15], the interaction of molecules with surfaces[16–19], charge transfer[20–23], etc.

1.1 THE ELECTRONIC STRUCTURE OF Cu AND Ag

Noble metals (copper, silver and gold) have been put to practical and decorative use by mankind for more than five millennia. They have been used as an economic store of value, that is money, for exchange with commodities in Ancient Greece and China for over two thousand years. Today, noble metals are hidden within cables that span the globe and microscopic interconnects within semiconductor wires that transport energy, information, and spam, as well as are exhibited as beautiful and lasting decorations that compensate for their wearers deficiencies and impermanence. Although we have been fascinated by the visual appeal of metals that does not mean that we have fully understood their optical responses. In this dissertation, I will reveal the underpinning microscopic electronic processes of the fundamental optical responses of silver and copper surfaces.

Silver and copper crystallize in face-centered cubic (fcc) structures[24], shown in Fig 1-1 (a). fcc metals crystalize by exposing their most stable, low-index surfaces. The triangles in Fig 1-1 (a) show the most stable (111) surface of the fcc crystal lattice. The electronic structures derived from s-electrons in metals is nearly isotropic, but in the case of (111) surfaces the anisotropy is most pronounced, and it creates the special properties on which this dissertation is mainly focused. This crystalline structure of the surface is symmetric under the 3-fold rotation operation about the <111> axis. Fig 1-1 (b) shows the first Brillouin zone of the fcc lattice structure, which is the momentum space representation of fcc single crystals. The shape of the Brillouin zone is a polyhedron bounded by the low-index planes. In my experiments, I investigate a small momentum range around the Γ point of the surface Brillouin zone.

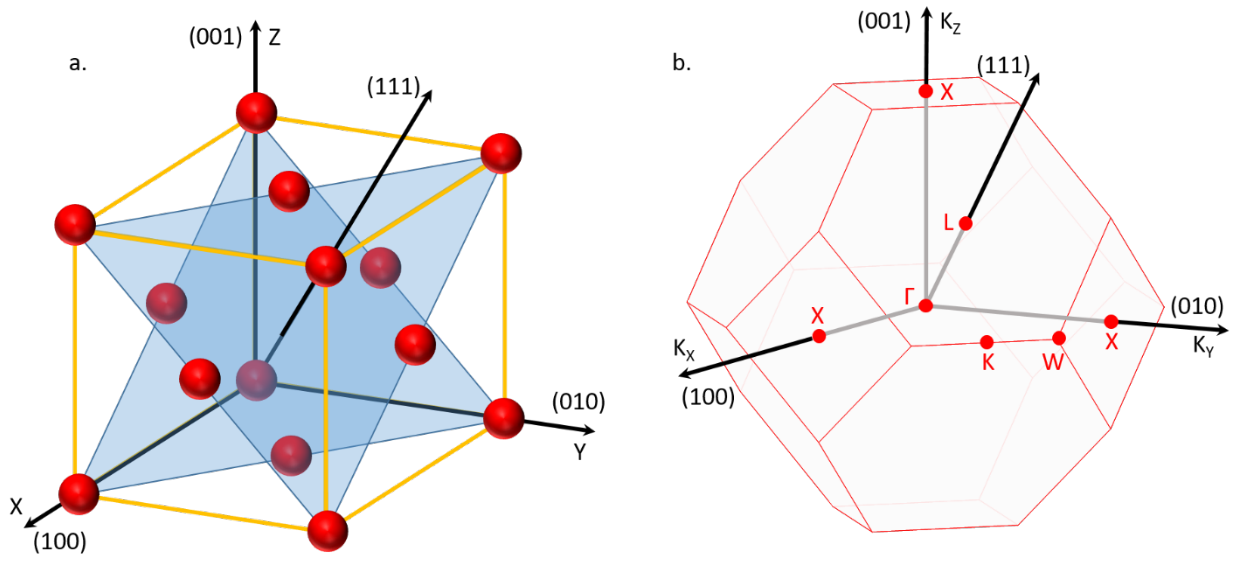

Figure 1-1 The fcc lattice structure (a) of Noble Metals, and the first Briouline Zone (b)

The Cu and Ag elements are both in d-block Group 11 in the periodic table. Cu atom is in the 4th period while Ag atom is in the 5th period. In the atomic state, both have only 1 unpaired electron sitting in the outmost s orbital, $4s^1$ and $5s^1$, for Cu and Ag, respectively, while their inner shells are fully filled.

The band structures of Cu and Ag have been studied extensively[25]. Figure 1-2 shows the calculation of Cu bulk band structure along (001) and (111) direction. The d-bands reaches to about 2 eV below Fermi Level, with top of the d-bands at X symmetry point. The lower sp-band has a minimum at about 9 eV below Fermi Level, and it cuts through the d-bands. In addition, the lower and upper sp-bands, shown as purple and black curves respectively, have a band-gaps in the Γ-X and Γ-L directions. In Ag, the bulk band structure is similar, but d-bands are deeper, reaching about to 3.8 eV below Fermi Level, and the band gap in the Γ-L direction is narrower.

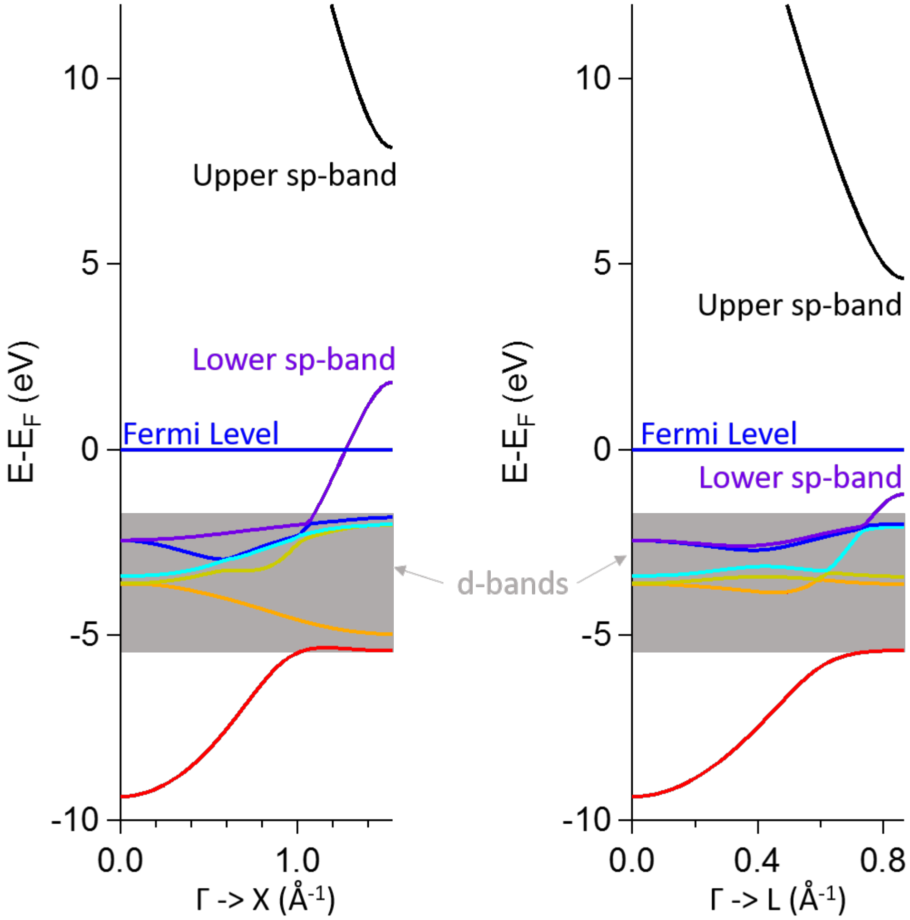

Figure 1-2 Cu bulk band strcuture

1.2 SCHOKLEY SURFACE STATE AND IMAGE POTENTIAL STATE

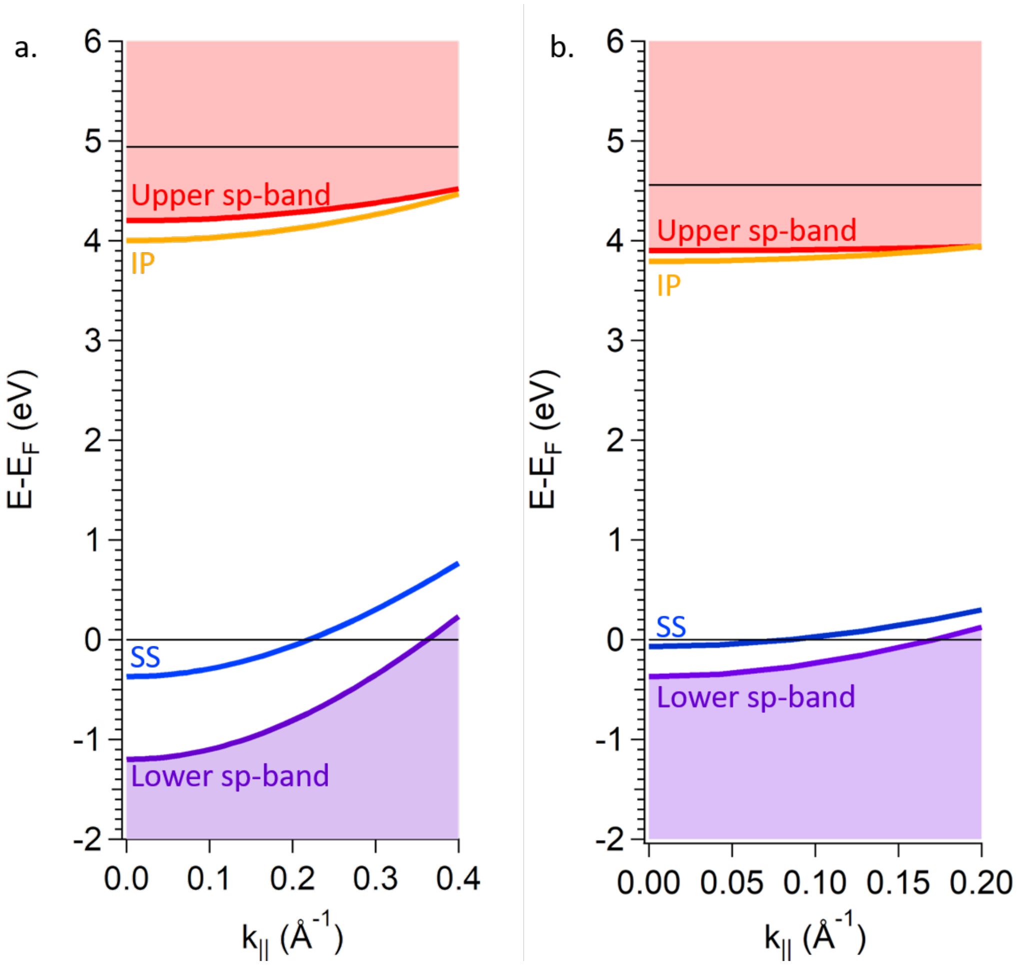

Figure 1-3 (111) surface projected band structure of Cu (a) and Ag (b)

The Figure 1-3 shows surface projected band structure[26,27] of Cu (a) and Ag (b). The lower and upper black horizontal lines are Fermi Level and work functions repectively. The bulk states corresponding to the upper sp-bands (U$_{SP}$) and lower sp-bands (L$_{SP}$) are indicated by curves and shaded areas of red and purple respectively. Between the U$_{SP}$ and L$_{SP}$, there is a projected band-gap on both metals, which is indicated by the white area. Inside the band-gap, reside two states, namely, the Shockley Surface State[28] (SS) and the n=1 Image Potential State[29] (IP). These two states, unlike sp-bands, are not bulk bands, but properties of the surfaces; they are prominent features in electronic spectroscopy of Cu(111) and Ag(111) surfaces[30].

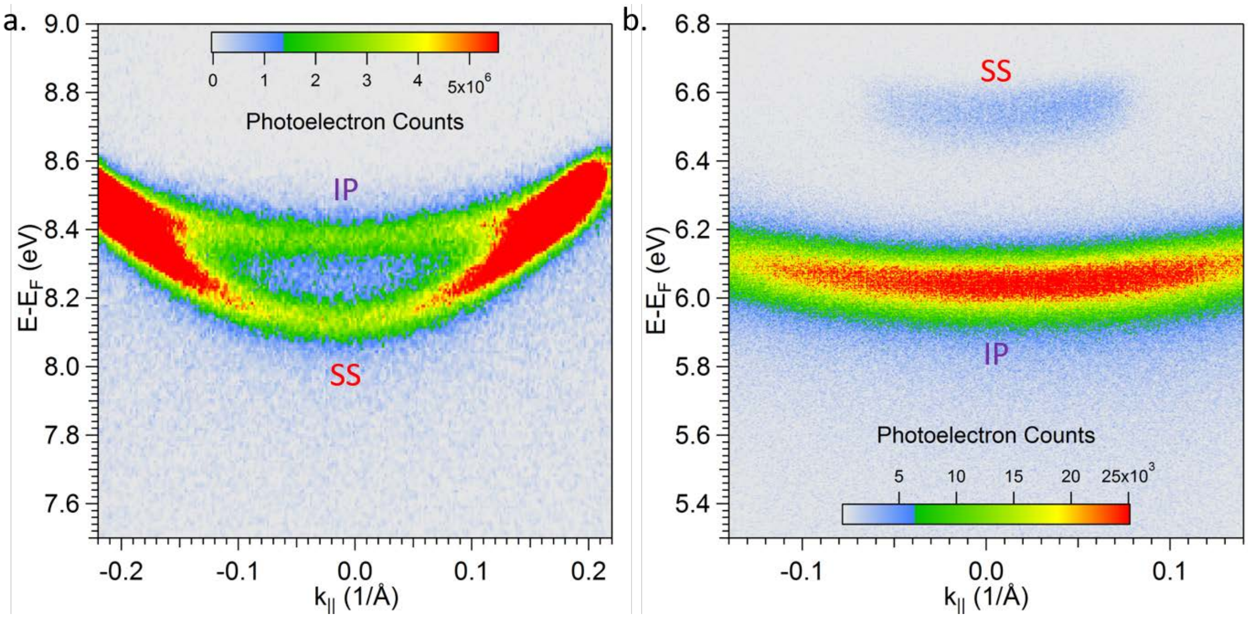

Figure 1-4 The SS and IP states observed in multiphoton photoemission experiments. a. In two-photon photoemission spectra of Cu(111) excited by 4.25 eV pulse laser SS and IP appear as the lower and upper parabolas, respectively; b. In three-photon photoemission spectra of SS and IP on Ag(111) excited by 2.20 eV pulse laser, SS and IP appear as the upper and lower parabolas, respectively

Figure 1-4 shows the experimental multiphoton photoemission measurement of SS and IP on Cu(111) (a) and Ag(111) (b), respectively. In Figure 1-4(a), SS lies below IP at $k_{||} = 0$ Å^{-1}, and resonates with IP at higher $k_{||}$. In Figure 1-4(b), SS (upper parabola) has smaller momentum range, because SS at Ag(111) is only 0.063 eV below Fermi Level, compared with about 0.4 eV below Fermi Level for Cu(111).

the SS and IP band are parabola-like curves with energy vs $k_{||}$, and the parabolic dispersion with parallel momentum gives the effective mass[24] from the Equation 1.1:

$$E(k) = E_0 + \frac{\hbar^2 k_{||}^2}{m_e * m_{eff}} \qquad \textbf{(1.1)}$$

$\boldsymbol{E_0}$ is the band energy relative to Fermi Level at the Γ point, or the vertex of the parabola, and $\boldsymbol{m_e}$ is the effective mass of the band or the curvature of the parabola. SS is more dispersive than IP for both Cu and Ag. For SS, the effective mass is around 0.4 for both metals[31,32], while for IP, the effective mass is 1.35 for Cu(111), and 1.33 for Ag(111)[33,34]. The values of $\boldsymbol{m_e}$ can be slightly different from different publications.

The Shockley Surface State[28] is first described theoretically by William Shockley in the Bell Telephone Laboratories. Due to the periodic arrangement of atoms in a crystal, according to the Bloch Theorem, the wave-functions of electrons have the form[24]:

$$\psi(\boldsymbol{r}) = e^{i\boldsymbol{k}\cdot\boldsymbol{r}} u(\boldsymbol{r}) \qquad \textbf{(1.2)}$$

where $\boldsymbol{k}$ and $\boldsymbol{r}$ are three-dimensional vectors representing the wave vector of electron propagation, and position respectively, u is a function with the same periodicity as the crystal, and ψ is the wave-function of a Bloch wave.

Any crystal, however, is not infinitely large, and therefore necessarily has boundaries at surfaces, which terminate the periodicity of the crystal. Upon creating a surface of a metallic crystal, the ideal unbounded periodic lattice is terminated, and as a consequence a new surface confined state is created, whose wave-function is mainly localized at the surface[35]. Akin to dangling bond states of semiconductor surfaces, the metallic SS are frequently split off from the bulk bands and reside in the band gaps. In the case of the (111) surfaces of noble metals the SSs are partially occupied, and form a 2D free electron gas at the metal-vacuum interface.

In addition to SS, there is another kind of surface electronic band referred to as the image potential states[36] (IP). The IP states exist close to the vacuum level for any solid-state material; their character is that their density mostly localized outside of metal surfaces in the vacuum. The origin of IP states is that an electron outside of a metal surface will polarize conduction electrons inside the metal to create a positive image charge[37]. Thus, IP states form on the screening time scale through the screening of the Coulomb field of the external charge.[38,39] The net effect of polarization of conduction electrons in a metal is equivalent to forming a positive image charge inside the metal. The screened Coulomb interaction is characterized by an attractive potential that is approximately given by[37]:

$$V(z) = E_V - \frac{1}{4z} \qquad \textbf{(1.3)}$$

where E_V is the vacuum level. This Coulomb-like potential supports a series of IP states, of which eigen-energies converge to the vacuum level in a Rydberg series[37]:

$$E_n = E_V - \frac{0.85\ eV}{(n+a)^2}, n = 1,2,3, \dots \qquad \textbf{(1.4)}$$

where a is a quantum defect.[38–42]

1.3 MULTIPHOTON PHOTOEMISSION

Einstein’s photoelectric effect is the basis for the modern photoemission spectroscopy[43], which has evolved into the most effective method for mapping the occupied electronic bands of solids. In this thesis, I will refer to conventional one-photon photoemission as 1PP. By increasing the power of exciting light, electrons are able to absorb more than one photon before relaxing back to the Fermi level. I will refer to such processes as multi-photon photoemission (mPP)[44–48], where m designates to nonlinear order of the process.

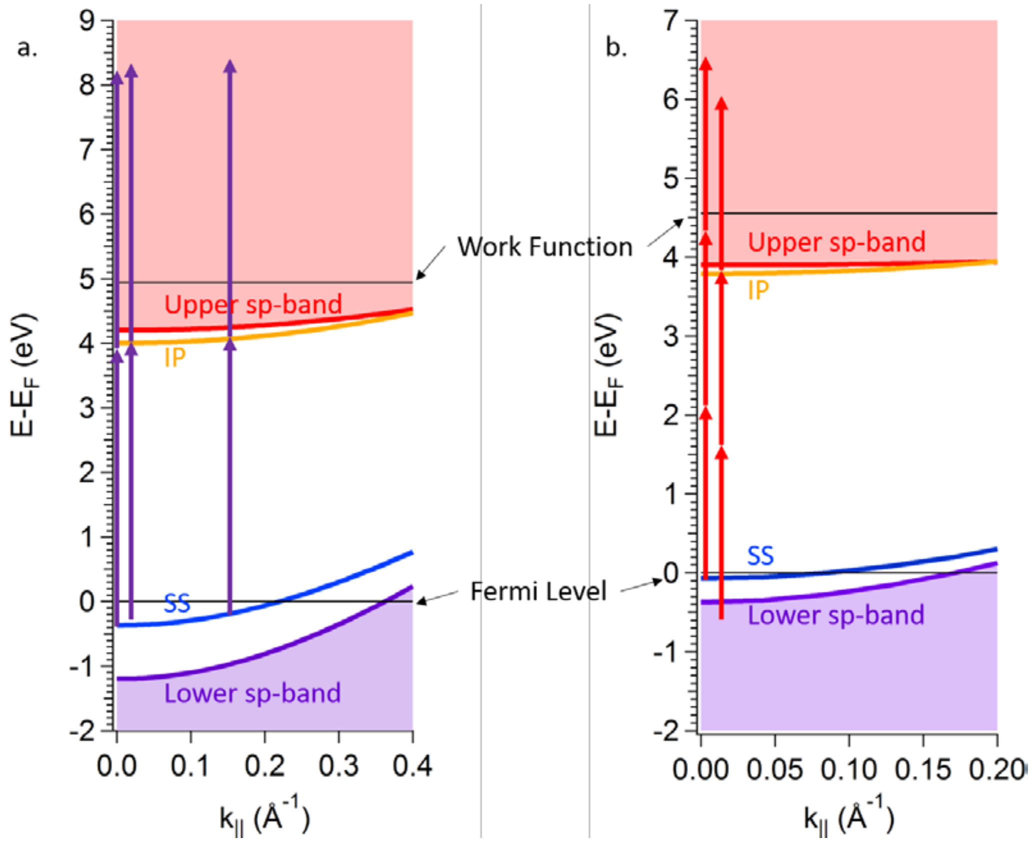

Figure 1-5 mPP scheme for 4.25 eV on Cu(111) (a.) and 2.20 eV on Ag(111) (b.)

The mPP spectra of Cu(111) and Ag(111) (Figure 1-4) can be explained by the schematic energy diagrams in Figure 1-5. The blue and yellow curves indicate SS and IP, respectively, which are within the band gap for a range of momenta about the Γ point. After absorption of 2 or 3 photons for Ag(111) or Cu(111) respectively, SS electrons are able to overcome their respective work function barrier, and thereby be emitted into the vacuum. The benefits of mPP are demonstrated by photoemission spectra from the IP. Electrons are first excited into the IP by 1- or 2-photon absorption for Ag(111) or Cu(111), respectively, and then, promoted further by absorbing another photon that excites them above the vacuum barrier. With these excitation schemes, we are also able to detect the unoccupied states.

Further, we could learn more information about the excitation process and electron dynamics by performing the interferometric time-resolved multiphoton photoemission (ITR-mPP) measurements, which will be introduced in Chapter 2

1.4 ORGANIZATION OF THE DISSERTATION

This thesis is organized as follows. I will introduce my experimental apparatus in Chapter 2. I will introduce the excitation laser system, its broad tunability, and also the Mach-Zander interferometer for delay scanning between two identical pulses with attosecond control of the delay. I will introduce the vacuum chamber for preparing the samples, and performing angle-resolved photoemission measurements. Finally, I will introduce the integration of the laser and detector operation to perform ITR-mPP measurements.

Computational modeling and simulation is an inseparable part for understanding the spectra of photoelectron, which will be discussed in Chapter 3.

Chapter 4 and Chapter 5 describe interesting results from mPP spectroscopy of surface state on Ag(111) and Cu(111) surfaces.

In Chapter 6, I will describe my simulations of interferometric measurements of multi-electron coherence in charge transfer excitation of Cs deposited on Cu(111).

2.0 EXPERIMENTAL APPARATUS

Photoemission experiments combine several experimental systems. The excitation source for mPP experiments is a broadly tunable femto-second laser based on noncollinear optical parametric amplifier (NOPA)[49]; the system is discussed in Section 2.1. The ultra-high vacuum (UHV) chamber enables us to prepare and keep clean our crystal samples by conventional surface techniques[50]. The UHV chamber also incorporates the Angle-Resolved Photoemission Spectroscopy (ARPES)[51] system, with which we perform mPP spectroscopy. These topics are discussed in Section 2.2. The three dimensional coherent photoemission spectroscopy (3DCPES) system gives us the ability to monitor the lifetime of quasi-particles in condensed matter. This part is discussed in Section 2.3. Techniques for characterizing a laser pulse will be discussed in Section 2.4.

2.1 THE LASER SYSTEM

A light source is crucial in researching an optical response of metal surfaces. The typical time scale for various dynamical process at metal surfaces ranges from the sub-femtoseconds up to picosecond range[46]. In order to understand these ultrafast phenomena, we use a sophisticated laser system to generate a train of laser pulses with duration of 10~30 fs in a widely tunable wavelength range.

the NOPA system pumped by a fiber laser can generate broadly tunable femtosecond (fs) laser pulses at a 1 MHZ repetition rate. The tunability makes the NOPA essential for exploring the optical responses of metal surfaces. To study the time evolution of the optical excitations at metal surfaces, we need to perform the pump-probe measurements. For this we use a Mach-Zehnder interferometer with an Interferometric time-delay scanning system. In addition, laser pulse characterization is essential to characterize the laser source before any measurements.

2.1.1 Second Harmonic Generation System

To broaden the wavelength range of laser, one can often resort to nonlinear optical conversion techniques, such as second harmonic generation (SHG)[52] and sum frequency generation (SFG)[52]. For example, the output of our NOPA laser is broadly tunable in a range of 530 ~ 1000 nm. This range can be extended to 292 ~ 430 nm by SHG of the NOPA output. In addition, the SHG and SFG are inside the NOPA system to generate the pump wavelengths. Further, the SHG technique can be used in characterizing laser pulse.

The key factor in the nonlinear optical conversion is the phase matching. Essentially, phase matching corresponds to momentum conservation while the generation and output pulses propagate in the nonlinear crystal. It is a requirement that all the fields oscillate in phase during the conversion process. Phase matching is described by the following equations[53]:

$$\boldsymbol{k}_3(\omega_1 \pm \omega_2) = \boldsymbol{k}_1(\omega_1) \pm \boldsymbol{k}_2(\omega_2) \qquad \textbf{(2.1)}$$

In the simplest situation, the three bold vectors $\boldsymbol{k}$ of the field propagation are all parallel with one another; in this case the equation is simplified to:

$$n_3 * (\omega_1 \pm \omega_2) = n_1 * \omega_1 \pm n_2 * \omega_2 \tag{2.2}$$

Unfortunately, materials have dispersion, which causes light of different colors to have different indices of refraction. Thus, the above equation is not generally satisfied. The condition can be satisfied if the nonlinear medium is birefringent so that differently polarized beams can experience different index of refraction while propagating in the same direction. In the case of a negative birefringent uniaxial crystal, such as beta barium borate (BaB_2O_4 beta phase; abbreviated as BBO)[53], in which the extraordinary light travels faster than the ordinary light, we can achieve phase matching at a specific incident angle that depends on the incident frequencies and the nonlinear process. In our lab, we use BBO crystals to perform the SHG, and SFG.

The method of the phase matching in type I in a BBO crystal is illustrated in Figure 2-1. The diagram shows the refringence index ellipsoid of BBO crystal for two wavelengths. The z axis is the optical axis, and any light with its polarization direction perpendicular with this axis is named ordinary light (o-light), for which refringence index is generally not changed as the incident direction of ordinary light changes. O-light is displayed as a circle in the figure. The orthogonal polarization direction, which is not perpendicular to the optical axis, is called extraordinary light (e-light), because its refringence index has dependence on the angle between the incident direction of the e-light and the optical axis of the birefringent crystal. The e-light has an elliptical index dependence on the incidence angle. The red ellipse and circle show the refringence index of the fundamental wavelength for different incident angles of e-light and o-light, respectively, and the purple oval and circle show the refringence index of the second harmonic of other fundamental wavelength light. At θ_p, the o-light circle of fundamental beam crosses the e-light ellipse of second harmonic beam; this corresponds to the phase matching condition. Thus, in a process, the fundamental beam entering a BBO crystal with ordinary polarization at the angle θ_p with respect to the optical axis, will generate the second harmonic with extraordinary polarization.

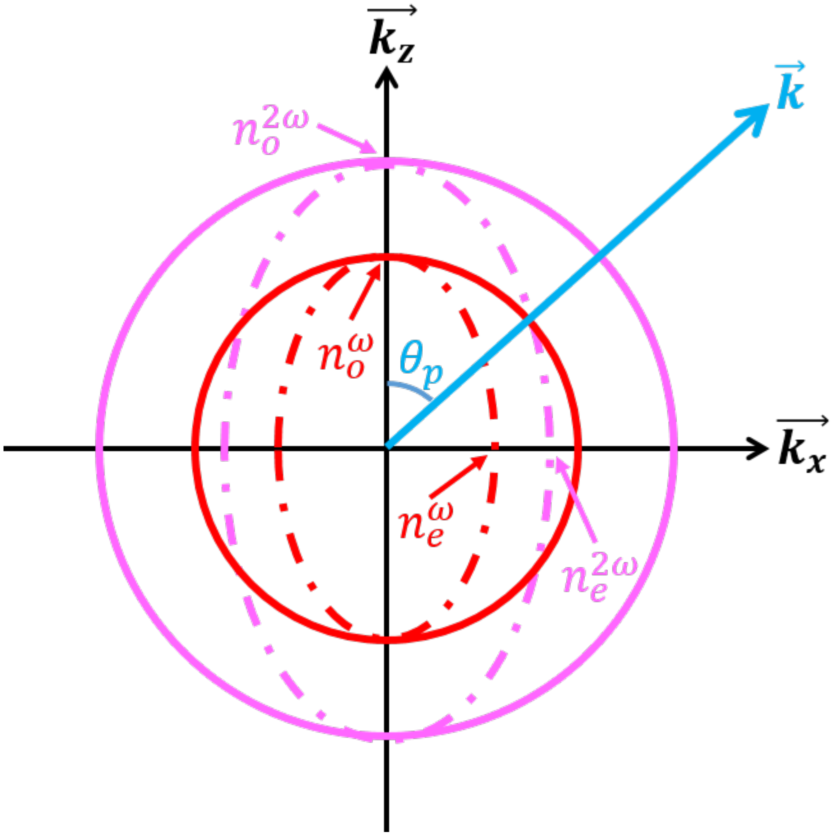

Figure 2-1 Type I Phase Matching In BBO crystal for SHG

The experimental setup of the SHG system is shown in Figure 2-2. To reduce dispersion which broadens the laser pulse as it propagates through dispersive media like glass, the concave reflection mirror is used near normal incidence to focus the fundamental laser pulse into the BBO crystal for SHG. The focusing mirror is mounted on a translation stage to manually optimize the focus in the BBO crystal. The double-headed arrows of different colors indicate the different polarizations for the fundamental and second harmonic beams, respectively. After the generation, the second harmonic light is re-collimated with another concave mirror. This mirror may have dielectric or aluminum reflective surface, depending on the wavelength of the generated second harmonic. Silver starts absorbing at around photon energy of ~3 eV, and therefore is not useful for UV applications.

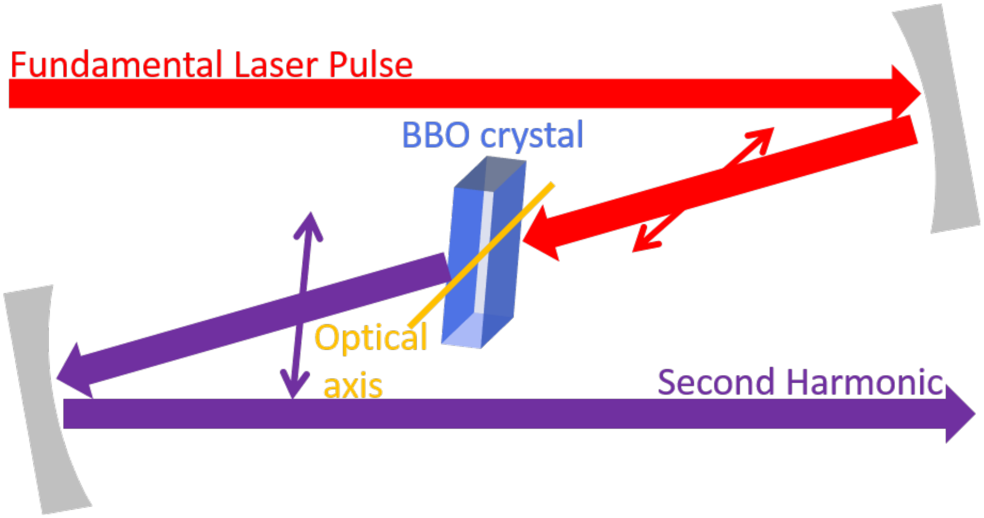

Figure 2-2 The experimental setup of the SHG system

2.1.2 NOPA System

The ability of generating wide-range-tunable laser pulse, makes the NOPA system extremely important when we explore the wavelength-dependent properties of a sample. Figure 2-3 shows its schematic setup.

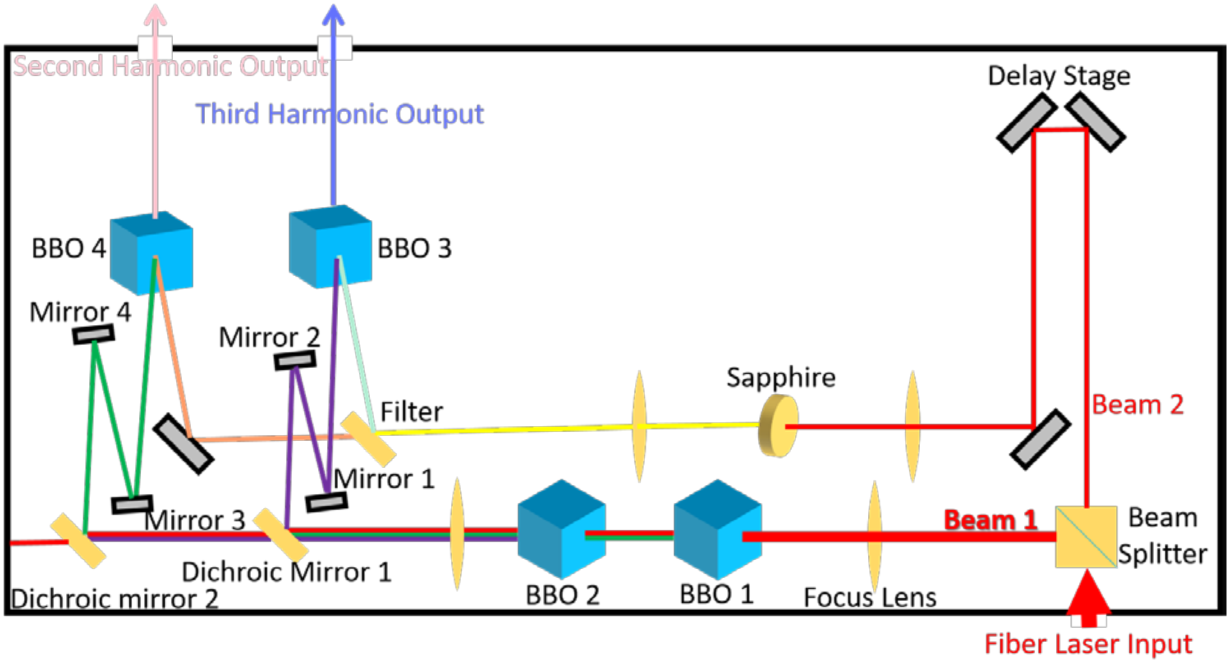

Figure 2-3 The NOPA setup

The NOPA system is pumped by a diode-pumped Ytterbium-doped fiber oscillator/amplifier system (Clark-MXR, Inc.), which produces pulse energy of 10 μJ at repetition rates of 1.25 MHz at 1030 nm with pulse duration < 250 fs. The 1030 nm pump laser, indicated by a large red arrow, enters the NOPA from the right bottom of the figure; it is immediately split into two beams by a polarizing beam splitter. One beam (Beam 1) has most of the energy, and is used for harmonic generation; the other (Beam 2) for white light generation has only a small fraction of the total energy, and sent to the delay stage for adjusting of the pulse timing.

Beam 1 is focused between two BBO crystals; in the first crystal BBO 1, it generates the second harmonic (SH) at 515 nm. The fundamental and second harmonic enter BBO 2, which generates the third harmonic (TH) at 343 nm by sum frequency mixing. The power of each harmonic can be adjusted by adjusting the orientation of the two BBO crystals.

The optical paths are adjusted by the delay stage so that the Beam 1 and Beam 2 meet at BBO 3 or 4, where NOPA generation occurs. After the delay of Beam 2 is set, it is focused into the sapphire crystal to generate the white light (WL). WL has a broad spectrum from ~520 to ~950 nm. The sapphire crystal is damaged after prolonged use, and therefore it can be rotated to a new spot as necessary.

The SH and TH light amplifies different parts of the WL spectrum. The dichroic mirror 1 reflects the WL below 650 nm to BBO 4 and passes the WL above 650 nm to the BBO 3. Then in the TH arm, the reflected light from Beam 1 and Beam 2 meet in BBO 3. The TH has high power but a small band-width, whereas the WL has low power but a broad band-width. The TH therefore amplifies a part of the WL spectrum in the BBO 3 crystal. The center wavelength of the amplified light can be tuned by the incident angle of the TH, and the relative delay between the TH and the WL. Mirror 2 is also mounted on a translation stage to tune the delay. Also, the bandwidth of the amplified light can be tuned by rotating the BBO 3 crystal.

The same approach works for the SH amplifying the white light of >680 nm in BBO 4. The laser coming from BBO 3 can be tuned from 530 nm ~650 nm, or 2.3~1.9 eV photon energy, with energy ~80 nJ/pulse, ~20 fs pulse duration. The laser coming from BBO 4 can be tuned from 650 nm ~1000 nm, or 1.9~1.24 eV photon energy, with energy ~200 nJ/pulse, ~20 fs pulse duration.

2.1.3 Interferometric Time Delay Scanning System

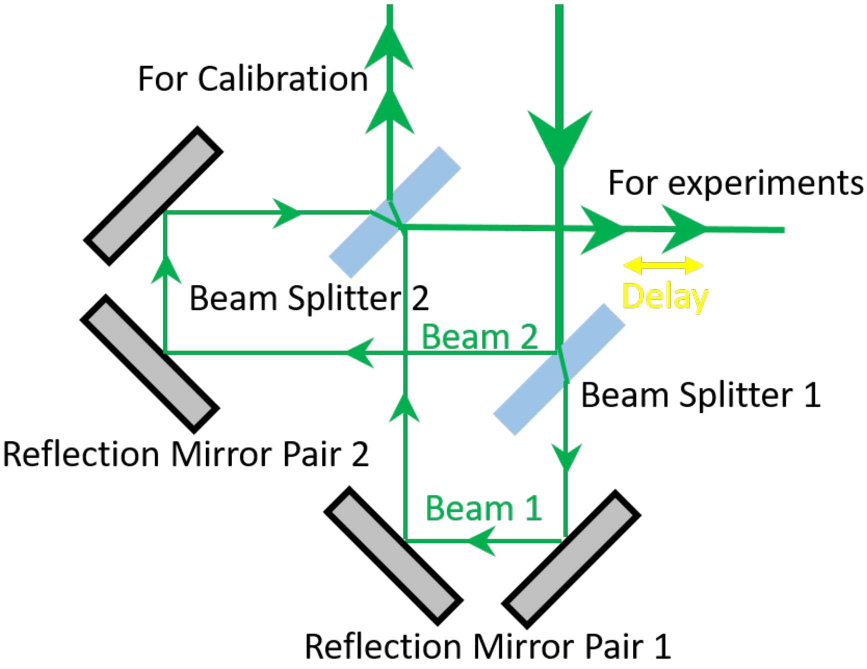

Figure 2-4 Mach-Zehnder Interferometer

The Mach-Zehnder Interferometer (MZI) is an important instrument for pulse characterization and interferometric pump-probe measurements. Especially for performing pump-probe measurements, the collinear design of MZI makes overlapping of the ultrafast pulses in time and space much easier than a non-collinear design. Also, the time-resolved measurements by interferometric single-color design of the Mach-Zehnder interferometer offer polarization information, which is otherwise unavailable in a two-color design.[46] The design of the MZI is shown at Figure 2-4.

As the laser beam enters the MZI it is split into two equal beams by the 50% Beam Splitter 1. Beam 1 goes straight down and is reflected onto the Beam Splitter 2 by the Reflection Mirror Pair 1; Beam 2 deflected by 90° and is also reflected onto Beam Splitter 2 by the Reflection Mirror Pair 2. Beam Splitter 2 also has 50% reflectivity; it recombines Beam1 and Beam 2, and creates two different outputs sending 50% of each into the two paths. The path where Beam 2 is transmitted is balanced with respect to the number of reflections and dispersion; this beam is sent to the experiment. The path where Beam 1 is transmitted is π phase-shifted with respect to the that other path; it is used for the time axis calibration and MZI stabilization, which will be discussed in section 2.3.

Beam 1 and Beam 2 have a variable light path difference, which is controlled by Reflection Mirror Pair 1 or 2. One of the Reflection Mirror Pair is translated by a piezo, which is controlled by computer, so the light path difference between the two beams can be accurately scanned and programmed. Thus, by MZI we create two identical pulse of controllable delay to better than 50 attosecond (as) from a single pulse. The underlying idea is that the first pulse (pump pulse) excites coherent polarization in a sample, and the second pulse (probe pulse) tests the evolution of the polarization by modulating the photoelectron spectra with respect to the relative phase delay.

2.2 THE UHV CHAMBER AND ARPES SYSTEM

All the experiments are performed in an UHV chamber for photoemission measurements. The chamber is also used to prepare the samples and to keep them free of adsorbates during the measurements. The base pressure of the UHV chamber is of $< 1.0 \times 10^{-10}$ mbar.

2.2.1 UHV System

Figure 2-5 and Figure 2-6 show the schematic diagrams of horizontal and vertical cross sections of our UHV system respectively. The vacuum is produced and kept by a turbo pump, ion pump and titanium sublimation pump (not shown in the figures). The UHV system consists of connected chambers. The samples are kept in the load-lock chamber, where they can be introduced from the atmosphere, stored on sample stage, and transferred to the measurement chamber. The transfer to the manipulator in the measurement chamber is performed with a magnetic transfer rod. The manipulator has 4-dimensional freedom of movement, including 3-dimensional translation and 1-dimensional rotation about axis of the manipulator. The 4-dimensional freedom of movement helps to position the sample in front of the hemi-spherical electron energy analyzer. The positioning must be precise to prevent distortion in the momentum distribution of photoelectrons. The photoelectrons are excited from the sample surface by the pulsed laser. The laser beam is introduced from the outside by passing through a lens, which makes the air/vacuum barrier and focuses the laser onto the sample. Photoelectrons with different energy and momentum are focused by an electrostatic lens onto the entrance slit of the hemispherical analyzer. Upon entering the analyzer, they are deflected by an electrostatic field according to their kinetic energy and mapped onto different positions on a 2D-delayline detector.

The detector collects electron count data (x and y position, and arrival time) to a computer to produce distributions that correspond to the angle-resolved photoemission spectra, that is, the electron count distribution of energy vs. angle/momentum.

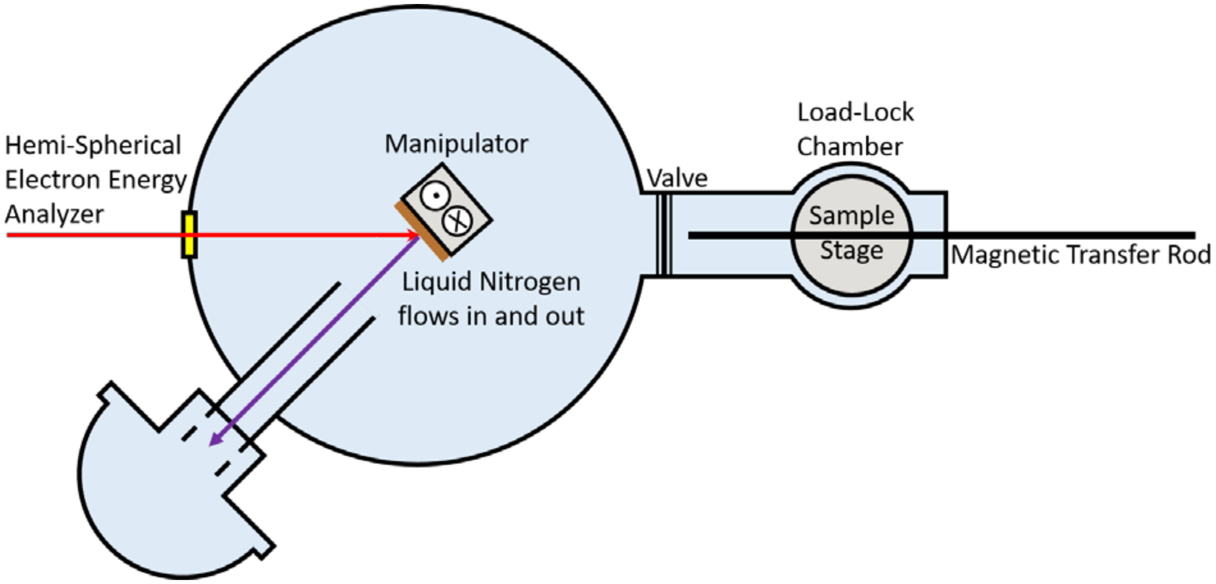

Figure 2-5 Horizontal cross section of the UHV System

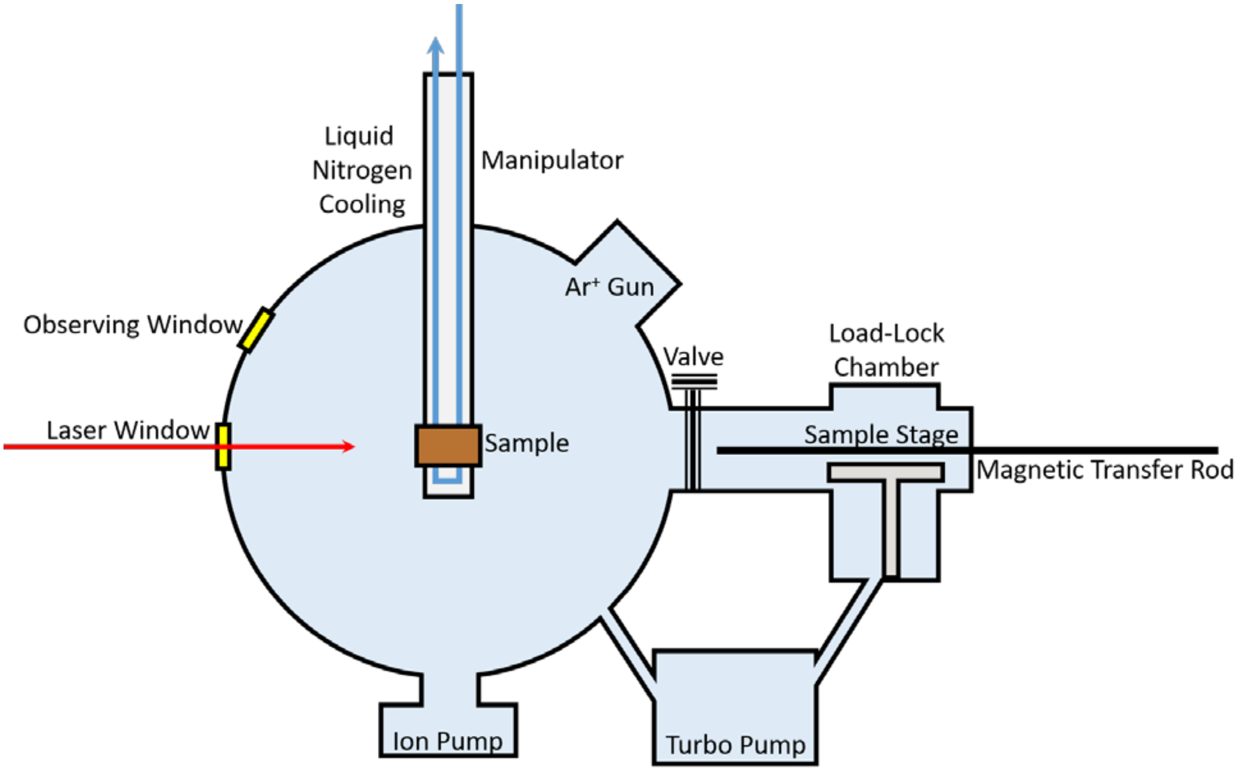

Figure 2-6 Vertical cross section of the UHV system

Before experiments, single crystalline metal samples are cleaned by cycles of sputtering with an Ar^+ gun and annealing by electron bombardment heating. (The electron heating device is behind the sample, and not shown in the figure) The manipulator has hollow center, into which we introduce liquid nitrogen to cool the sample and keep it at ~100 K by pumping liquid nitrogen through the manipulator.

2.2.2 ARPES System

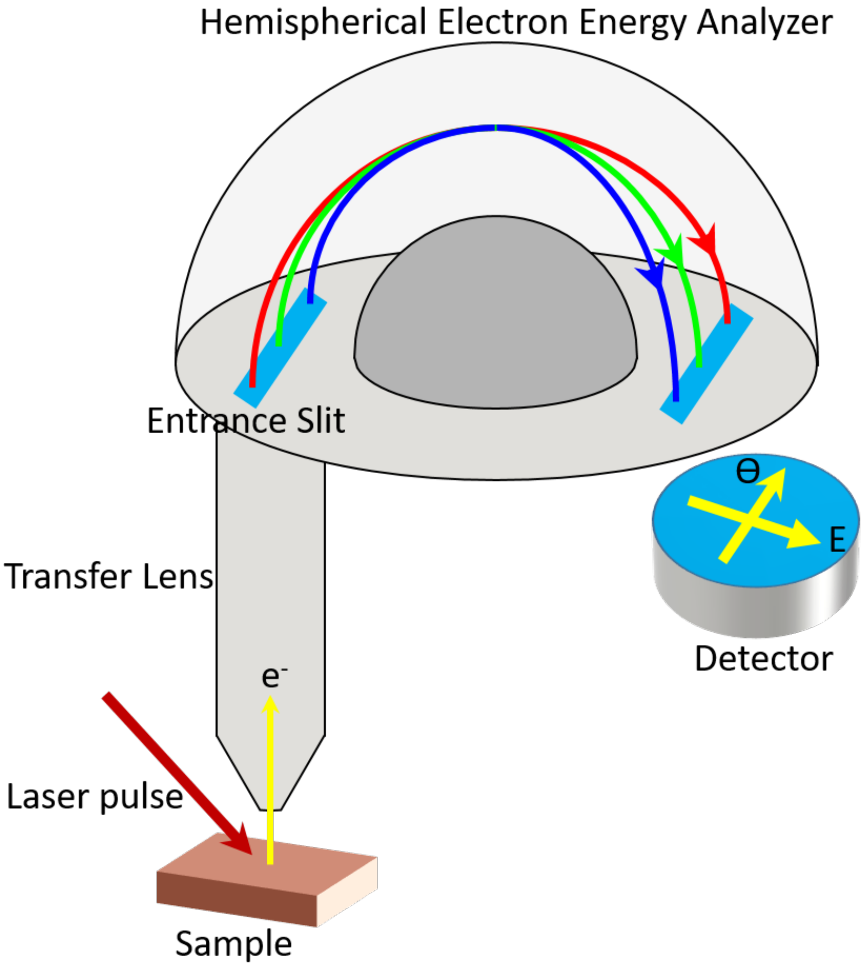

Figure 2-7 The diagram of hemispherical electron energy analyzer

Figure 2-8 The diagram of our PHOIBOS 100 Hemispherical Electron Energy Analyzer from SPECS Surface Nano Analysis GmbH. E and θ indicate the energy and momentum dispersion axes.

Electrons are excited by the laser pulse from the sample surface, and have a wide angular distribution, are focused by the transfer lens system into the energy filter (the hemispherical part of the analyzer). The entrance slit, which sits between lens system and the energy filter, not shown in the above figure, allows a fraction of electrons into the energy filter. A wide slit allows higher intensity of the photoemission spectra with sacrificing energy resolution, while a narrow slit gives photoemission spectra of better energy resolution but lower intensity.

The Phobios 100 has two hemispherical metal surfaces with a mean radius of 100 mm. The inner hemisphere and outer hemisphere are held at a different electric potential. Thus, the electrons entering the energy filter will be deflected and mapped into detector by the static electric field. We use a delay-line detector (DLD) to simultaneously measure the electron count distribution among angle and energy.

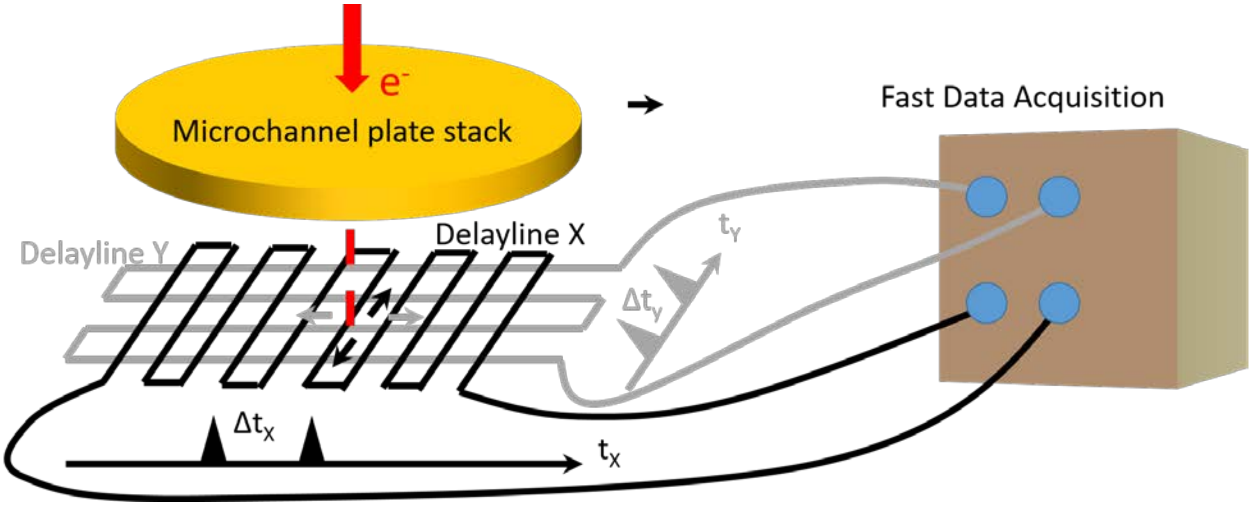

Figure 2-8 Schematic drawing of the basic parts of the Delay-line Detector

Schematic drawing of the basic construction of the DLD is shown in Figure 2-8. The DLD consists of a microchannel plate (MCP) stack for amplifying single electron signals by >10^7, and an in-vacuum readout unit. Photoelectrons, deflected by analyzer onto the DLD, are amplified by the MCP stack, and then are accelerated by a potential of several hundred volts into the meander delayline X & Y wires. The electrons that are captured by the wires travel to both ends of the delayline X & Y wires. The DLD determines the hit x and y positions of photoelectron generated pulse by the relative time delays (Δt_X, Δt_Y). Accumulating such signal for single electron hits produces the electron count distribution of energy vs. angle/momentum.

2.3 3DCPES

With interferometric time delay scanning system introduced into the laser path, the time-delay dimension between pump and probe pulses is added to the ARPES system; this enables 3DCPES

We have discussed how to generate two identical pulses with controllable time delay by Mach-Zehnder Interferometer in section 2.1.4, and we discussed the ARPES system in section 2.2.2. Now we need a system to ensure the Mach-Zehnder Interferometer working in synchronization with the ARPES system.

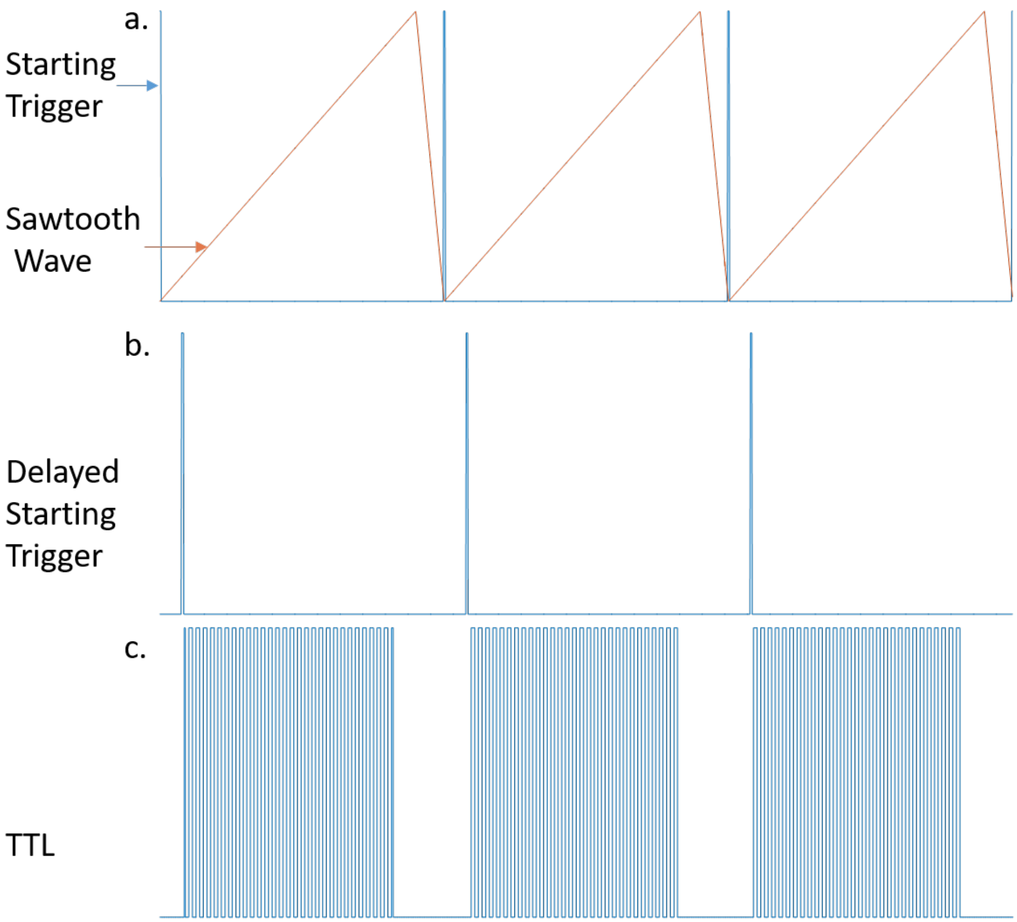

Figure 2-9 Diagram of Trigger Transformation

Figure 2-9 shows how we use trigger signals to synchronize our measurements. We program a Stanford Research Systems Model DS345 synthesized function generator to generate a sawtooth wave and a start trigger at the beginning of each period of the sawtooth wave. The sawtooth wave is a slowly ascending and rapidly descending voltage ramp as a function of time; the signal is used to control the scanning of the piezoelectric actuator in the MZI, which scans the time delay between the two output pulses. Both ramps are linear with time, so that the delay time is scanned uniformly.

However, when the piezoelectric actuator changes the scanning direction, a sudden change in velocity could introduce noise., so we avoid using the data near the turning points. We program Stanford Research Systems Model DG535, with the input of synchronizing starting trigger, to create the delayed starting trigger signal.

The delayed signal is then fed to the NI PCI-6711 card, which is mounted on a common PC. A LabVIEW program for the NI PCI-6711 card creates multiple (for example, 4,096) TTL signals. These TTL signals are used to for two things: 1) to tell ARPES system to take an energy vs. momentum at each signal; and 2) to tell NI PCI-MIO-16E-4 card to record the calibration wave (see Figure 2-4).

For a typical 3DCPES measurement, we take about 500 time-delay scans, and for each scan we take 4096 images at different time delay points. At each time delay point, we acquire spectral images corresponding to hundreds of pixels for energy and momentum, respectively. For our DLD, the pixel resolution is 1,000*600. To shrink the image size, we can bin several pixels into one, and select a rectangular range of interest (ROI) though the Application Program Interfaces (APIs) of our DLD.

For multiple scans, each scan starts at the same delay time, and they are synchronized by the delayed starting trigger. Inside each scan, the images taken at each time-delay point are synchronized with the calibration wave.

In addition to the above procedure, we insert a Stanford Research Systems Model SR560 Low-Noise Voltage Preamplifier between the sawtooth wave and the piezo controller. The SR560 acts as a filter for the high frequency digital staircase part of the sawtooth wave to reduce the noise of scanning.

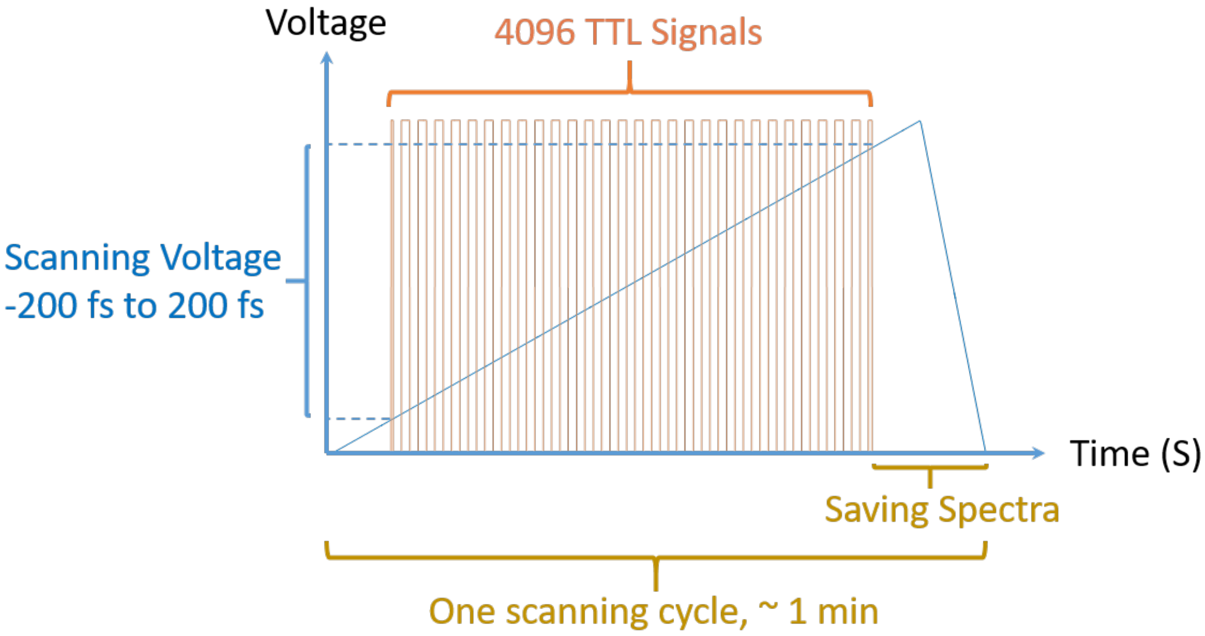

Figure 2-10 One Cycle of delay Scanning

Figure 2-10 describes one typical cycle of scanning in the 3DCPES measurement. We apply sawtooth wave voltage to the piezo in the Mach-Zehnder Interferometer to create time-delay between two pulses. The time-delay is proportional to the applied voltage. A typical scanning range is about -200 to 200 fs, which can be adjusted by changing the voltage range of the sawtooth wave.

The scanning triggers are in the ramping-upward part of the sawtooth wave, and for our experiments, each period of the scanning trigger is 12 ms; this gives the ARPES system about 10 ms of integration time for one image at a specific time-delay. After prescribed number of ARPES images at different time delays are taken, the 4,096 ARPES images are fetched and written to hard drive, within the left time before the next scanning trigger starts the next cycle. When the scanning range is fixed, for example, -200 to 200 fs, changing the number of scanning triggers changes the time-delay resolution. 4,096 TTL signals mean about 0.1 fs scanning step between 2 successive ARPES images. For a typical 3DCPES measurement with 600 nm wavelength, one optical cycle is about 2 fs, which means that there are about 20 sampling points per optical cycle.

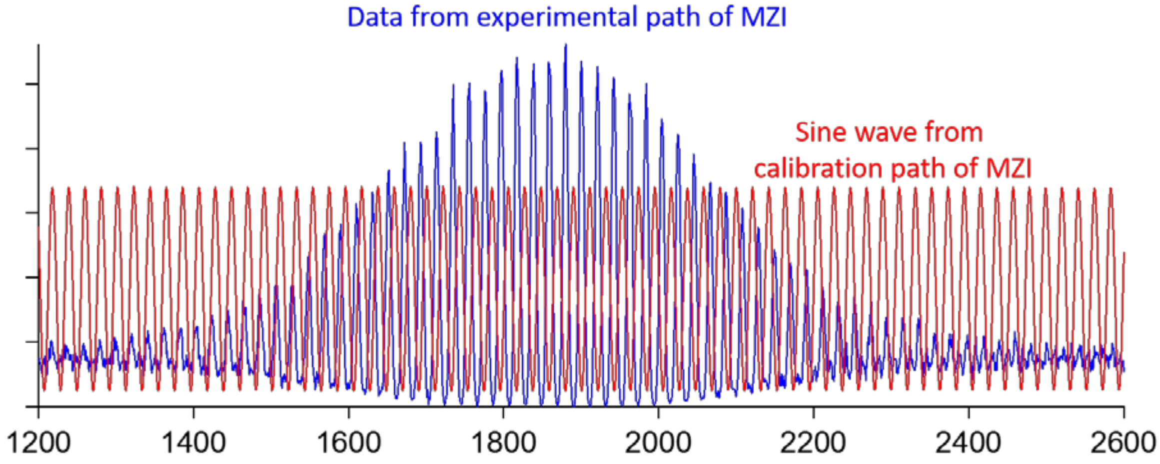

Figure 2-11 Time Axis Calibration

Figure 2-11 demonstrates how we calibrate the time axis for each scan. In section 2.1.3 and figure 2-4, we showed the structure of Mach-Zehnder interferometer. On one hand, a laser pulse from the experimental path is directed into sample surface, and the blue wave in figure 2-11 is the time-sequence data of SS at Cu(111) at Γ point measured by 400 nm laser. On the other hand, laser pulses from the calibration path pass through the monochromator, their frequency spectrum is narrowed, and therefore, the pulses are stretched. The interference between the pulses then becomes continuous on the time scale of the delay scanning providing a sine wave signal, contrasting with the blue wave, which does not pass through a monochromator. Then the voltage on the detecting photodiode is recorded and synchronized with the scanning triggers. So, the blue and the brown waves are synchronized by the scanning triggers.

In Figure 2-11, the blue and red waves share the common X-axis consisting of an array of sampling points. The period of the red sine wave corresponds to the wavelength of light, which can be directly read from the monochromator readout. The period of the sine wave and the time delay are related by the speed of light. Thus, by recording the calibration sine wave the relative delay-time for the correlation measurement represented by the blue wave is thus determined. Also, zero delay point can be determined by the symmetry of the blue wave. In this way, we can calibrate the exactly the time-delay axis for the blue wave, and correct the slow shifts between 2 successive scans up to 1 period. In experimental measurements, the time-sequence data from the experimental path does not necessarily have the same period as the time-sequence data from the calibration path. Also, time-sequence data from the experimental path may have a time-dependent oscillation period.

After determination of the time axis for each scan, we have a set of data of electron counts in the space spanned by [energy, angle/momentum, time delay, scan]. We add up the electron counts from all scans for the same energy, angle/momentum, and time delay; thus, we obtain the data of 3DCPES.

2.4 LASER PULSE CHARACTERIZATION

Before performing a measurement, we need to characterize and optimize the laser pulse. Phase dispersion is introduced in the optical path when laser passes through dispersive media like air, glass, etc. The pulse is characterized by an interferometric autocorrelation (IAC) technique. We create two replicas of the laser pulse and scan their time delays by MHI described in section 2.1.3, and check the light intensity of the SHG described in section 2.1.1. Alternatively, we can also use the photoelectron signals for in situ measurement by using 3DCPES techniques described in section 2.3. When we use the 3DCPES techniques to measure autocorrelation, light is introduced onto sample holder surface, which is made of polycrystalline molybdenum, and its optical response is considered to be instantaneous.

$$I(\tau) = \int_{-\infty}^{+\infty} |[E(t) + E(t-\tau)]^2|^2 \, dt \tag{2.3}$$

Equation 2.3 gives the second-order IAC function. The electric field $E(t)$ of the pulse, instead of laser intensity, is correlated with itself after a variable delay τ; such correlation of fields, rather than intensities preserves the phase information of the correlated waves to produce the autocorrelation trace.

$$E(\omega) = E_0 e^{-\frac{(\omega-\omega_0)^2}{2\omega_\tau^2} - i*\boldsymbol{k}(\omega)*\boldsymbol{z}} \tag{2.4}$$

$$\boldsymbol{k}(\omega) = \boldsymbol{k}(\omega = \omega_0) + \frac{\partial \boldsymbol{k}}{\partial \omega}(\omega - \omega_0) + \frac{1}{2}\frac{\partial^2 \boldsymbol{k}}{\partial \omega^2}(\omega - \omega_0)^2 \tag{2.5}$$

Equation 2.4 describes the propagation of a Gaussian light pulse, while Equation 2.5 is a Taylor expansion of the frequency dependent propagation vector, $\boldsymbol{k}(\omega)$. $E(\omega)$ is the electric field amplitude of each frequency component in the spectrum of the pulse laser; ω_τ describes its spectral width; and ω_0 is the center frequency of the pulse laser. To see how the phase term $\boldsymbol{k}(\omega) * \boldsymbol{z}$ in Equation 2.4, where and $\boldsymbol{z}$ it the space vector, changes the pulse shape $E(t)$, we will perform an Inverse Fourier Analysis on Equation 2.3 with Equation 2.4 inserted. Since $E(t)$ is not an experimentally observable quantity, we further look at the autocorrelation traces $I(\tau)$.

Only keeping the zeroth-order term $\boldsymbol{k}(\omega = \omega_0)$, every frequency component in Equation 2.4 will be in phase, and Inverse Fourier Transformation will yield the pulse shown in Equation 2.6:

$$E(t) = E_0 e^{-\frac{1}{2}\omega_\tau^2 t^2 - i*\boldsymbol{k}(\omega=\omega_0)*\boldsymbol{z} + i\omega_0 t} \qquad \textbf{(2.6)}$$

Only keeping the first-order term $\frac{\partial \boldsymbol{k}}{\partial \omega}(\omega - \omega_0)$, the Inverse Fourier Transformation will yield the pulse shown in Equation 2.7:

$$E(t) = E_0 e^{-\frac{1}{2}\omega_\tau^2 \left(t - \frac{\partial \boldsymbol{k}}{\partial \omega} * \boldsymbol{z}\right)^2 + i\omega_0 t} \qquad \textbf{(2.7)}$$

Only keeping the second-order term $\frac{1}{2}\frac{\partial^2 \boldsymbol{k}}{\partial \omega^2}(\omega - \omega_0)^2$, the Inverse Fourier Transformation will yield the pulse shown in Equation 2.8:

$$E(t) = E_0 e^{-\frac{1}{2}\omega_\tau^2 t^2 \frac{1}{1-a*i} + i\omega_0 t} \approx E_0 e^{-\frac{1}{2}\omega_\tau^2 t^2 (1+a*i) + i\omega_0 t} \tag{2.8}$$

$$a = -\frac{\partial^2 \boldsymbol{k}}{\partial \omega^2} * \boldsymbol{z} * \omega_\tau^2 \tag{2.9}$$

In Equation 2.6, only the zeroth-order dispersion is considered, and it gives only an overall phase to the pulse. When only the first-order dispersion is considered in Equation 2.7, there is a time shift term $\frac{\partial \boldsymbol{k}}{\partial \omega} * \boldsymbol{z}$ to the pulse. When the second-order dispersion only is taken into consideration in Equation 2.8, there is an extra phase term $-\frac{1}{2} a\omega_\tau^2 t^2$, besides the term $\omega_0 t$, to the pulse.

$$\varphi(t) = -\frac{1}{2} a\omega_\tau^2 t^2 + \omega_0 t \tag{2.10}$$

$$\omega = \dot{\varphi(t)} = -a\omega_\tau^2 * t + \omega_0 \tag{2.11}$$

The complete phase terms are written in Equation 2.8. It is interesting to look at the angular frequency, shown in Equation 2.9, which is the first derivative of phase with respect to time. Now, the angular frequency is no longer a constant, but sweeps with velocity proportional to the second-order dispersion as defined in Equation 2.9. The frequency change with time is called a chirp. Thus, Equation 2.11 shows a linear chirp. Thus, unlike zeroth- and first- order dispersion, the second-order dispersion will cause a modification of the pulse shape, and its effects can be seen in interferometric autocorrelation measurements.

$$E(t) = \exp\left\{ -\left(\frac{t}{T_0}\right)^2 (1 + a * i) + i * \omega_0 t \right\} \tag{2.12}$$

$$\begin{aligned} I(\tau) = \quad & 1 + 2\exp\left[-\left(\frac{\tau}{T_0}\right)^2\right] \\ & + 4\exp\left[-\frac{a^2+3}{4}\left(\frac{\tau}{T_0}\right)^2\right]\cos\left[\frac{a}{2}\left(\frac{\tau}{T_0}\right)^2\right]\cos(\omega_0\tau) \\ & + \exp\left[-(1+a^2)\left(\frac{\tau}{T_0}\right)^2\right]\cos(2\omega_0\tau) \end{aligned} \tag{2.13}$$

Using a simple linear chirped Gaussian pulse, as shown in Equation 2.12, plugging into IAC function, defined in Equation 2.3, we get Equation 2.13. Equation 2.13 naturally is composed of 3 parts, corresponding to $0 * \omega_0$, $1 * \omega_0$, $2 * \omega_0$ oscillations given by three separate terms. There is an interesting relationship of the autocorrelation amplitude between time 0 and infinity, shown in the following equation.

$$I(0)/I(\pm\infty) = 8/1 \tag{2.14}$$

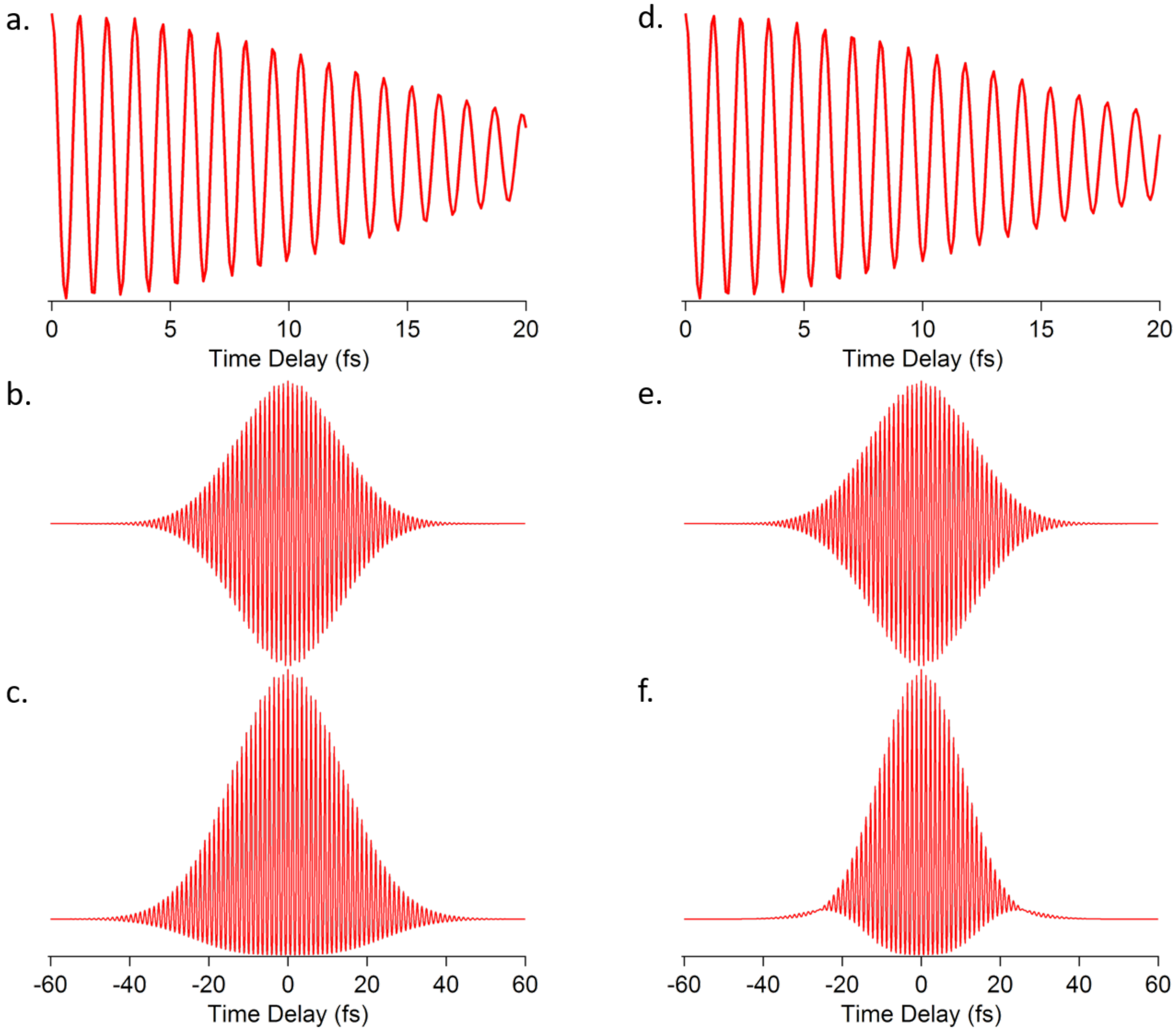

Figure 2-12 Simulation of IAC traces without chirp (a, b, c) and with chirp (d, e, f)

Figure 2-12 shows how a linear chirp affects the pulse and IAC traces. A laser pulse of 350 nm and 30 fs duration and its IAC are plotted in Figure 2-12b and Figure 2-12c. By setting $a = 1.5$ in Equation 2.12, the pulse details without and with chirp are compared in Figure 2-12a and Figure 2-12d. Figure 2-12a has more than 17 periods in 20 fs, while Figure 2-12d has less than 17 periods. The resulting IACs are compared in Figure 2-12c and Figure 2-12f. The major differences in Figure 2-12f are that the oscillation finishes earlier, there is a phase shift in the oscillations and the baseline is not flat at short delays giving an impression of an incoherent decay process.

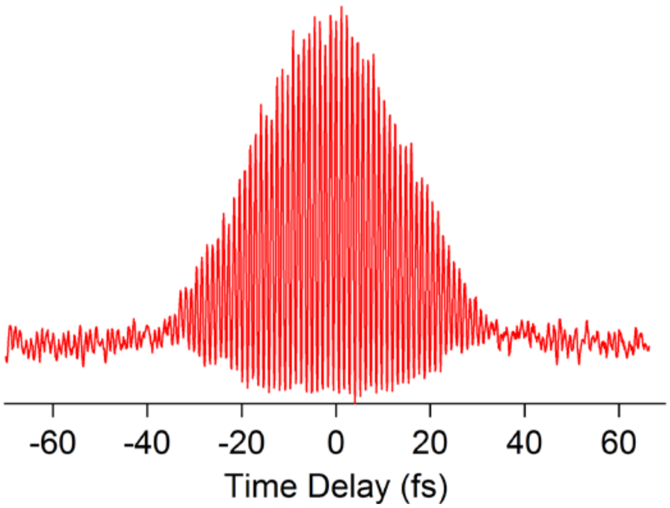

Figure 2-13 Experimental IAC of 340 nm laser pulse with 30 fs duration

Figure 2-13 shows a typical experimental IAC trace. In the optical path, we use a pair of negative-dispersive mirrors to compensate the high-order dispersions in order to approach the Fourier-transform limited pulse at the position of laser interacting with the target material. We perform in situ IAC measurement to characterize our laser pulse. By adjusting the laser reflections between the negative-dispersive mirror pair, we minimize the laser pulse duration at the sample position.

3.0 COMPUTATION AND SIMULATION

My research concerned the mPP process on clean Ag and Cu surfaces. These surfaces have characteristic surface states, which are the dominant features in mPP spectra. The simulation of the spectra requires the knowledge of the surface state wave functions. This chapter discusses the calculation of SS and IP state wave-function, the simulation of the mPP process, and some techniques for analyzing the experimental spectra.

3.1 WAVEFUNCTION CALCULATION

In previous chapters, we have introduced SS and IP states at metal surfaces, which are the major topics in our study. In this section, we will describe how to calculate their wave functions.

The theoretical modeling of the electronic structure of noble metals requires a simple model to describe their electronic structure. Chulkov[54] et al. proposed a useful one-dimensional pseudo-potential model to approximately describe the potential across metal surfaces along the direction normal to metal surfaces. With his parametrization we can easily calculate the wave functions on a personal computer using the following equations:

$$V_1(z) = A_{10} + A_1 \cos\left(\frac{2\pi}{a_s} z\right), z < D \tag{3.1}$$

$$V_2(z) = -A_{20} + A_2 \cos(\beta(z - D)), D < z < z_1 \tag{3.2}$$

$$V_3(z) = A_3 \exp\big(-\alpha(z - z_1)\big), z_1 < z < z_{im} \tag{3.3}$$

$$V_4(z) = \frac{\exp\big(-\lambda(z - z_{im})\big)}{4(z - z_{im})}, z_{im} < z \tag{3.4}$$

In the above equations, D is the half-depth of the sample, and the origin is taken as position of the first ion, which is closest to the vacuum. There are ten parameters in the above equations: A_{10}, A_1, A_{20}, A_2, β, A_3, α, z_1, λ, z_{im}; by requiring the continuity in zeroth and first-order derivative of the piece-wise potential curve at the break points, only four parameters are independent, and they are chosen to be A_{10}, A_1, A_2, and β. The rest parameters are calculated by continuity boundary conditions. Equation 3.1 describes the potential inside the bulk material, while a_s is the interlayer distance. Equation 3.2 and Equation 3.3 reproduces the potential of solid-vacuum interface region. The intermediate point z_1 is given by $z_1 = 5\pi/(4\beta)$, and $V_2(z_1) = -A_2/\sqrt{2}$. Equation 3.4 gives the asymptotic potential in vacuum. The pseudo-potential model is given in Figure 3-1.

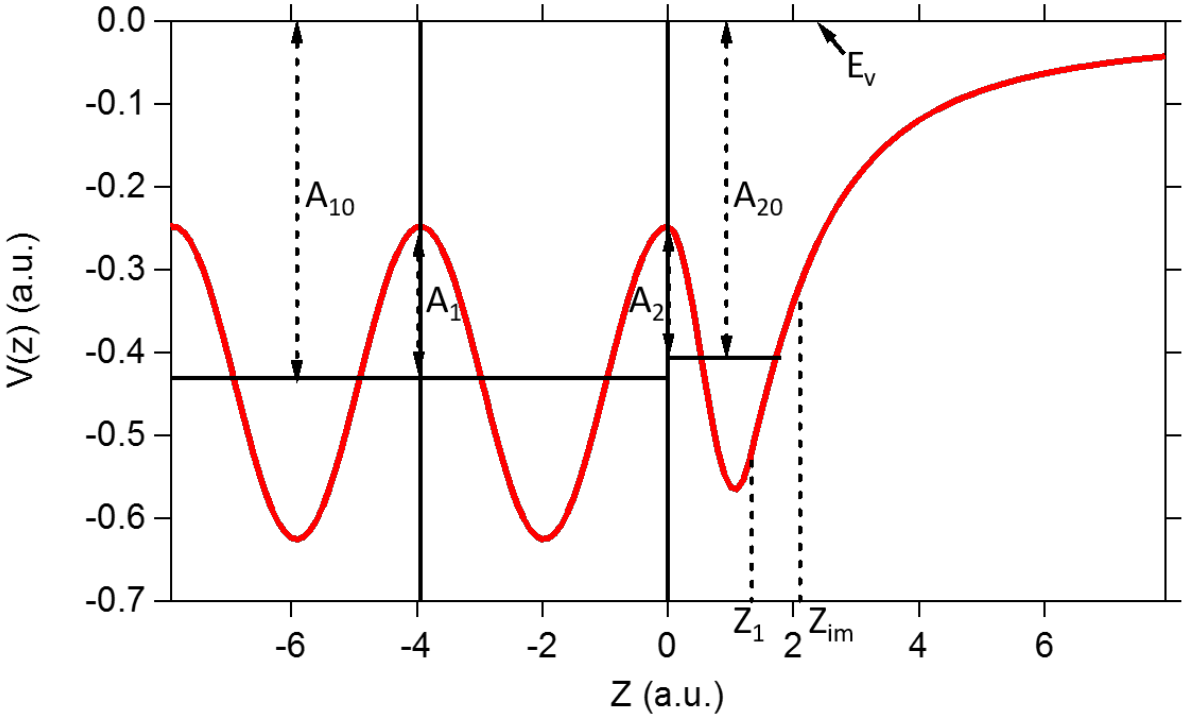

Figure 3-1 One-Dimensional Psuedo-Potential

With the potential described by Equation 3.1 – 3.4, a single electron moving inside such potential is described by the time-independent Schrödinger Equation, shown in Equation 3.5. The eigen-problem of electron in this pseudo-potential is then solved programmatically by the Mapped Fourier Grid Method[55,56].

$$\widehat{H_0}\psi_n(z) = \left[-\frac{\hbar^2}{2m_e}\frac{d^2}{dz^2} + V(z)\right]\psi_n(z) = E_n\psi_n(z) \qquad \textbf{(3.5)}$$

Before going into details of Mapped Fourier Grid Method, we will introduce the "ordinary" Fourier Grid Method[57] first.

The Schrödinger Equation (Equation 3.5) is composed of a kinetic energy and a potential energy operator. The simplest way to represent the kinetic energy operator as a matrix is in the momentum space, while the easiest way to represent the potential energy operator as another matrix is in the real space. Fourier Transformation comes naturally to merge these two representation. So the Equation 3.5 is reduced to diagonalize the sum of the kinetic energy matrix and the potential energy matrix.

A grid here means equally-spaced points z_i $(i = 1, \ldots, N)$ on the z axis. One uses the Dirac δ functions as basis functions in real space coordinates, so that any wave function $\psi_n(z)$ can be expanded by the Equation 3.6

$$\varphi_i(z) = \delta(z - z_i) \; (i = 1, \ldots, N) \tag{3.6}$$

For this basis set, the kinetic energy operator is a Hermitian Matrix, and the potential energy operator is a diagonal matrix. By diagonalizing the Hamiltonian matrix, we obtain eigen-values and eigen-functions, which correspond to eign-energies and wave-functions.

When we discretize the z axis as equally-spaced points, the grid spacing $\Delta z = z_{i+1} - z_i$ limits the minimum wavelength which can be contained as our solution. The smaller the spacing is, the higher momentum component that can be obtained as the solution. Choosing the grid space to be smaller will have benefits resolving eigen functions, which contain larger momentum components. On the down side, the smaller grid space will require larger memory usage and longer CPU time.

Looking at Figure 3-1, the potential is oscillatory for $z < z_{im}$, but when $z > z_{im}$, the potential has approximately $1/4z$ dependence. So the grid spacing should be chosen to be at least smaller than the oscillatory period. But on the vacuum side, the potential has less information, so it does not require a very dense sampling points. In order to have uneven sampling points over the potential, the Mapped Fourier Grid Method is adopted, because it not only provides more accurate results but also it consumes less computation resources by sampling the potential more efficiently.

The strategy is to introduce an auxiliary grid in a new axis of q, on which the sampling points are equidistant. The sampling points on the z axis are not equidistant, but are mapped onto the new axis q. The mapping procedure is shown in Figure 3-2, where the mapping function is

$$z(q) = q - A * \arctan(\beta * q) \qquad \textbf{(3.7)}$$

In the example Figure 3-2, the plots are drawn for A and beta set to 1. It is clear that, when z is close to 0, the sampling points in z are dense; when z is far away from 0, the sampling points in z are sparse.

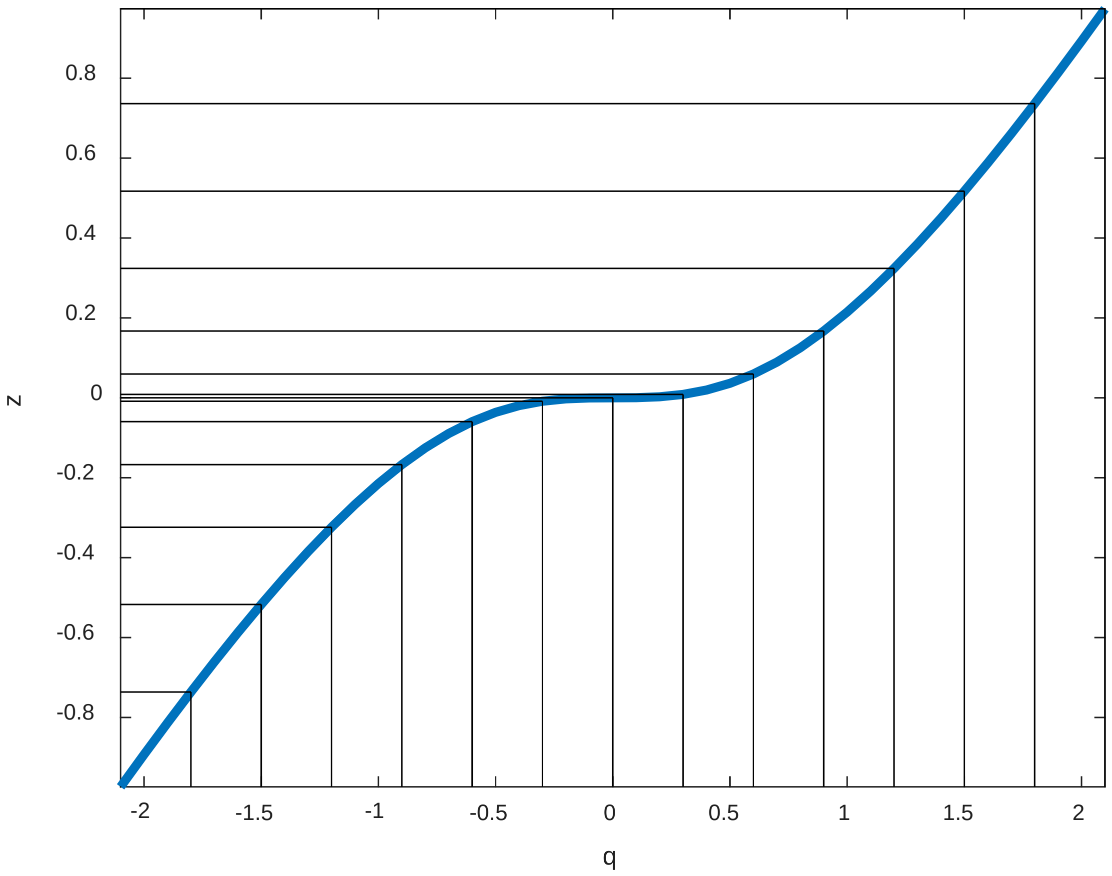

Figure 3-2 Mapping Procedure

In Mapped Fourier Grid method, the Hamiltonian is rewritten by Equation 3.8:

$$\widehat{H_0} = V\big(z(q)\big) - \frac{\hbar^2}{2m}\left(\frac{\partial q}{\partial z}\frac{\partial}{\partial q}\right)^2 \qquad \textbf{(3.8)}$$

Using Chulkov's Pseudo-potential for Cu(111), and solving the potential with Mapped Fourier Grid method, I obtained a series of eigen-energies, which are plotted in Figure 3-3. We can see there is a band gap around the 100th eigen-energy, which corresponds to SP-band gap on Cu(111), and the SS and IP states reside in this gap.

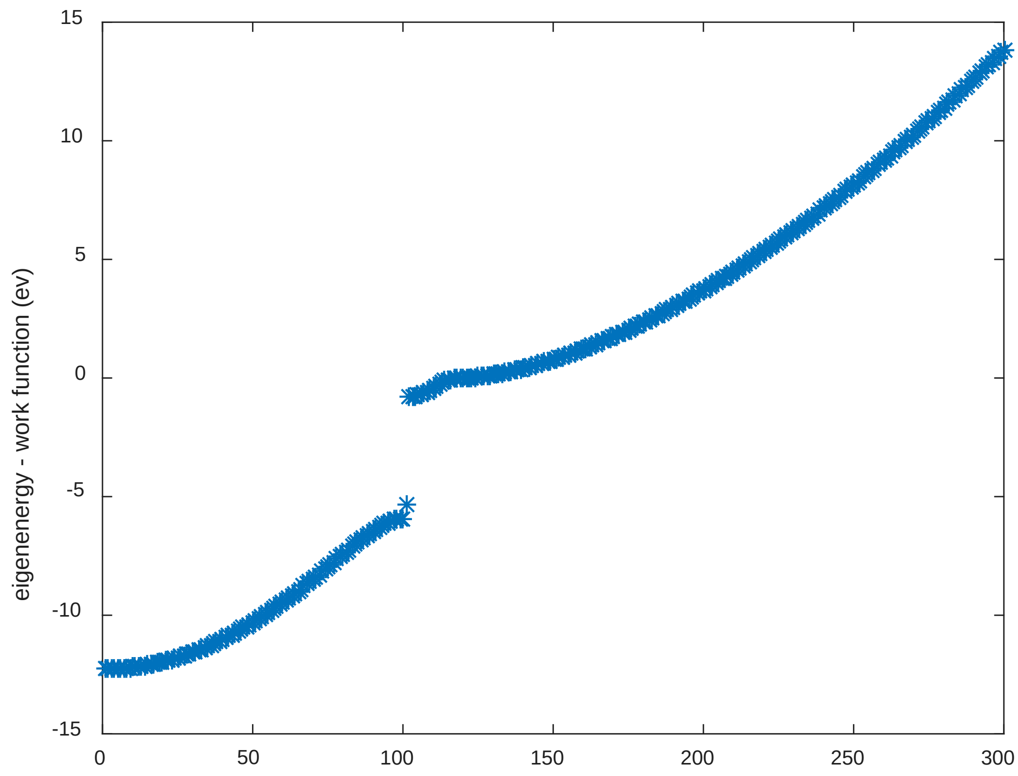

Figure 3-3 First 300 eigen-energies obtained by solving Chulkov's for the Cu(111) pseudo-potential.

The probability densities of SS and IP are plotted in Figure 3-4. The purple line shows the potential of Cu(111), the green line the probability density of SS state, and the red line the probability density of the IP state.

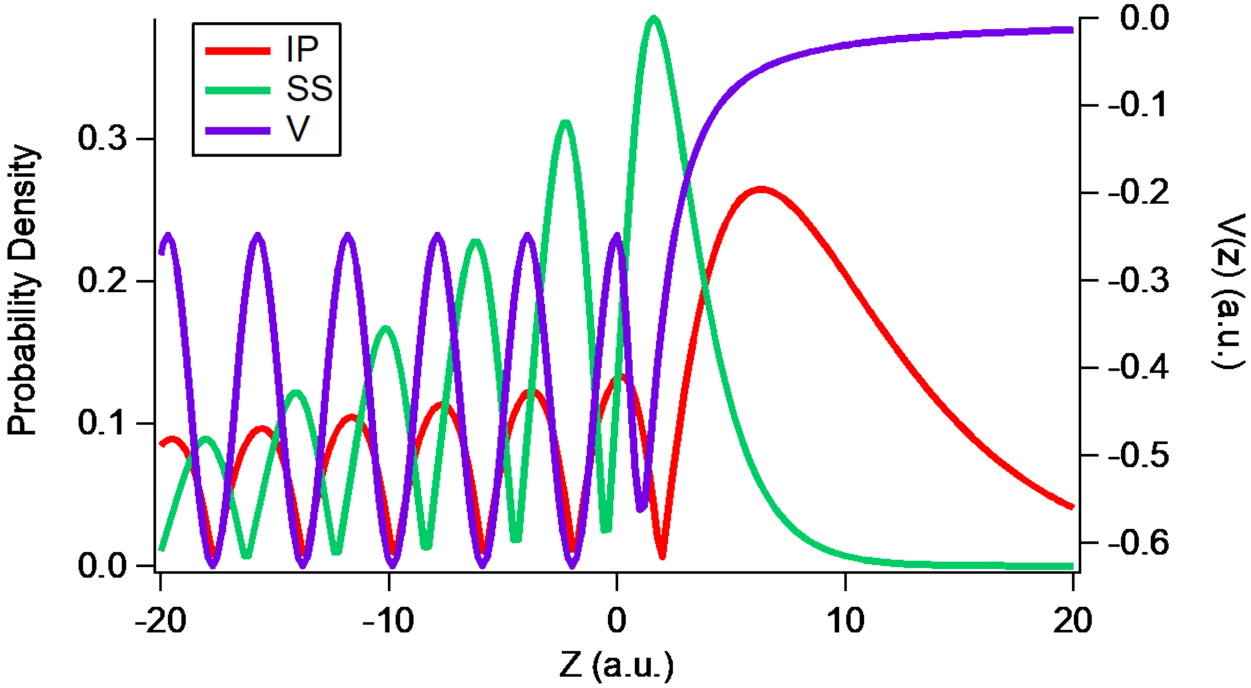

Figure 3-4 The Cu pseudopotential (purple), SS state probability density (green), and IP state probability density (red).

3.2 MULTIPHOTON PHOTOEMISSION SIMULATION

This section presents simulation of multiphoton photoemission process using Optical Bloch Equations[6,58,59] and the surface band structure that was introduced in the last section.

The quantum mechanical response of noble metal surfaces to a time dependent perturbation field can be described using density matrix formalism (Equation 3.9). Equation 3.9 is a density matrix involving 4 states, state 0 to 3, which are coupled by the perturbation field. The diagonal elements of the density matrix describe the population of each state: ρ_{00} is the probability of finding electron in State 0, which is the ground state. The off-diagonal elements describe the coherence bridging two states: ρ_{10} is the coherence between State 1 and State 0. Coherence describes a quantum mechanical superposition of two states. The density matrix is always Hermitian, and thus, elements in symmetric positions with respect to the diagonal, are complex conjugates: $\rho_{10} = \rho_{01}^*$. So, in describing a 3PP process with a density matrix of 4 states, only 10 elements are independent.

$$\begin{matrix} \rho_{00} & \rho_{01} & \rho_{02} & \rho_{03} \\ \rho_{10} & \rho_{11} & \rho_{12} & \rho_{13} \\ \rho_{20} & \rho_{21} & \rho_{22} & \rho_{23} \\ \rho_{30} & \rho_{31} & \rho_{32} & \rho_{33} \end{matrix} \qquad \textbf{(3.9)}$$

The Optical Bloch Equations describe the changing rates of each of the independent elements under the perturbation of the excitation laser field. In the Optical Bloch Equations, the coherence between any two states is created by the laser field, and, state populations are changed by the coherences. In addition to the creation of coherence and transferring the electron populations by the laser field, naturally coherences decay and electrons in high energy states decay into lower states through the quantum system’s interactions with its environment, for example e-e scattering, and e-phonon scattering, etc. These decays, must asymptotically obey the second law of thermodynamics, and are phenomenologically represented by decay time constants. For example: T_{11} is the population decay time constant for State 1; T_{10} is the pure coherence decay time or pure decoherence time constant between States 1 and 0. Obviously, states below the Fermi Level have infinite population decay time or infinite lifetime.

To derive the Optical Bloch Equations, we start from the unperturbed states (see Equation 3.10), with unperturbed Hamiltonian H_0, and original quantum eigen state ϕ_k, and associated eigen-energy $E_k = \hbar\omega_n$. When the perturbation $H'(t)$ turned on, the wave functions become time dependent (see Equation 3.12) and can be rewritten as linear combination of the unperturbed states (see Equation 3.11). Then Equation 3.11 is substituted in to the Schrödinger Equation (See Equation 3.12), and we can solve for the time-dependent coefficients a_k in Equation 3.13. The matrix terms H'_{nk} are explained in Equation 3.14. $H'(t)$ is the time dependent perturbation term, and here is composed of dipole moment and laser electric field. (see Equation 3.15)

$$H_0\phi_k = E_k\phi_k \tag{3.10}$$

$$\psi(t) = \sum\nolimits_k a_k(t)\phi_k \tag{3.11}$$

$$i\hbar\frac{\partial\psi(t)}{\partial t} = H(t)\psi(t) \tag{3.12}$$

$$\dot{a}_n = -i\omega_n a_n - \frac{i}{\hbar}\sum\nolimits_k H'_{nk}\, a_k \tag{3.13}$$

$$H'_{nk} = \int \phi_n^* H'(t)\phi_k\, d^3r \tag{3.14}$$

$$H'(t) = -e \cdot r \cdot E(t)\cos(\omega_l t) \tag{3.15}$$

$$\rho_{mn} = a_m a_n^* \tag{3.16}$$

$$\dot{\rho}_{mn} = \dot{a}_m a_n^* + a_m \dot{a}_n^* \tag{3.17}$$

From the definition of the new wave function in Equation 3.11, and also ϕ_k being a set of normalized orthogonal basis, the density matrix of the system can be written in Equation 3.16. We are now trying to construct the general density matrix equations, independent on the coefficients of the basis of the unperturbed system $a_k(t)$. The way we achieve this, is deriving the rate of changing of the density matrix, which is easily derived in Equation 3.17. With Equation 3.13 substituted into, Equation 3.17, it can be rewritten in terms of ρ_{mn}, and its first derivatives with time $\dot{\rho}_{mn}$. In this way, we construct a set of self-consistent equations for the density matrix. In addition, because of the decay of density matrix elements due to the system's interaction with environment, additional terms ρ_{mn}/T_{mn} describing the decaying should be added on the right side of Equation 3.17 (see Equation 3.18). Then we get the Optical Bloch Equations for the individual elements of the matrix.

$$\dot{\rho}_{mn} = \dot{a}_m a_n^* + a_m \dot{a}_n^* + \rho_{mn}/T_{mn} \tag{3.18}$$

Solving the Optical Bloch Equations, one can simulate the outcome of multiphoton photoemission process. But to simulate a three-dimensional coherent photoemission experiment, we need simulate 3PP spectra for every time delay and momentum. In measuring 3DCPES, we are experimentally performing the multiphoton photoemission measurement with different time-delays between the identical pump and probe pulses (typical measurement time delay range is from about -100 fs to 100 fs with step size of 0.1~0.2 fs). To describe the pump-probe measurement, above Equation 3.15 should be changed to

$$H'(t,\tau) = -e \cdot r \cdot \left[E(t)\cos(\omega_l t) + E(t+\tau)\cos\big(\omega_l (t+\tau)\big)\right] \tag{3.19}$$

A simple simulation of the 3DCPES is given in Figure 3-5 and Figure 3-6. The simulation uses $h\nu = 2.25$ eV photon energy and 20 fs duration laser pulses to excite electrons from 0.4 eV below Fermi Level, passing through a virtual state, to a 2-photon resonant state at 4.1 eV, and finally to the photoemission continuum by absorption of an additional photon. Figure 3-5b shows electronic structure of the simulated model and the excitation diagram; Figure 3-5a shows the electron count (normalize the max count to 32) at 6.35 eV above Fermi Level versus the time delay; the inset Figure 3-5c shows details of Figure 3-5a for the time delay range from 30 fs to 60 fs; Figure 3-5d is the Fourier Transformation of Figure 3-5a.

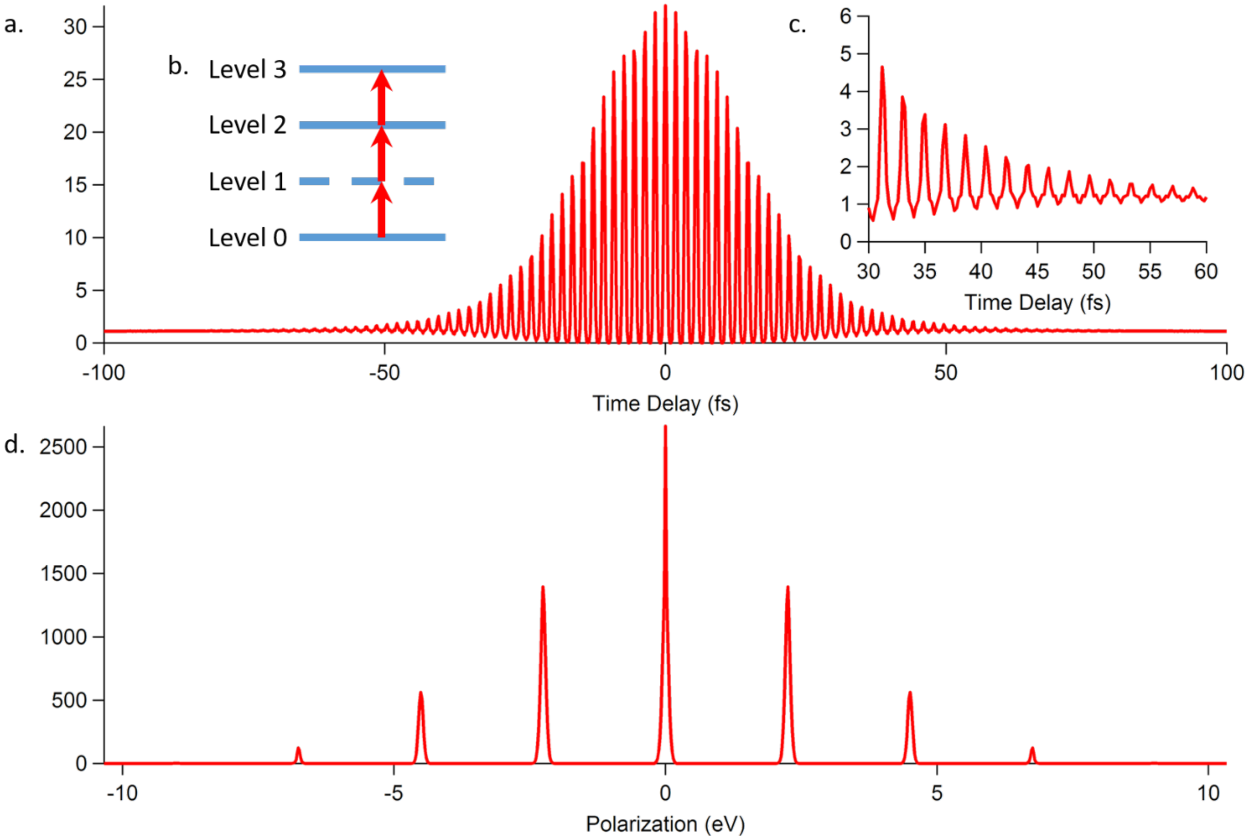

Figure 3-5 Simulation of an interferometric two-pulse correlation for a 3PP process

Figure 3-5 shows several typical features of interferometric two-pulse correlation measurements.

First, the time-resolved trace (Figure 3-5a) is oscillatory with a bell-like envelope. The oscillation comes from the fact that we are performing a pump-probe measurement with identical and collinear pulses. The first to interact pump pulse creates an optical excitation in the initially thermalized system; the excited system instantaneously starts to evolve and decay. The nonlinear orders of polarization are necessarily excited because the photoemission experiments involve two or more photon absorption. The pump pulse will polarize the electrons in the system, and there will be several different orders of the polarization field, which is both dependent on the laser pulse and the electronic structure of the probed system. The second pulse will probe the evolved and decayed system, and also will interfere with the polarization field. So, total electron counts signal vs. the time delay will contain interesting information: the decaying of the population of the involved states, the decaying of the coherence between the involved states, and also the polarization field induced by laser pulses. At time delay = 0, the population and coherence has not started to decay, so the electron count max should be expected at time delay = 0.

Second, because of the nonlinearity there are several orders of laser frequency in the oscillating signal. If we zoom in Figure 3-5a, (see Figure 3-5c) we can clearly see that the oscillation is not sinusoidal, and that requires several frequencies to be present in the signal. As we have discussed, these different frequencies may come from higher orders polarization, laser-driving frequency, and frequencies unique to the specific electronic structure of our sample

Third, the ratio of the electron count at zero to that at infinity for a three-photon process is approximately to $32/1$. Assuming that the laser pulse has electric field with amplitude 1, then at time delay 0, the total field has the amplitude of 2. In an n-photon photoemission process, the electron counts are proportional to the laser intensity to the n^{th} order, which equals the electric field amplitude to the $2n^{th}$ order. So, when two identical pulses perfectly overlap (when time delay is 0), the electron count is 2^{2n}, with a constant coefficient. When two identical pulses no longer overlap and no interference is observed (when time delay is very large compared with laser pulse duration), the electron count will be $2 * 1^{2n}$, with the same constant coefficient. In summary, the ratio of the signal at zero delay as compared with infinite delay is $2^{2n-1}/1$. For 3PPE process, it is 32/1. It is a very useful and practical way to check both your experimental data and simulation results.

Fourth, when time delay is close to zero, the local minima are very close to 0, because the two identical pulses are nearly cancelling each other and little power to excite electrons out.

Fifth, the electron count vs time delay should be symmetric with respect to time delay 0.

Figure 3-5d is the Fourier Transformation result of Figure 3-5b. There are clearly several integer orders of the laser photon energy, and everywhere else is 0.

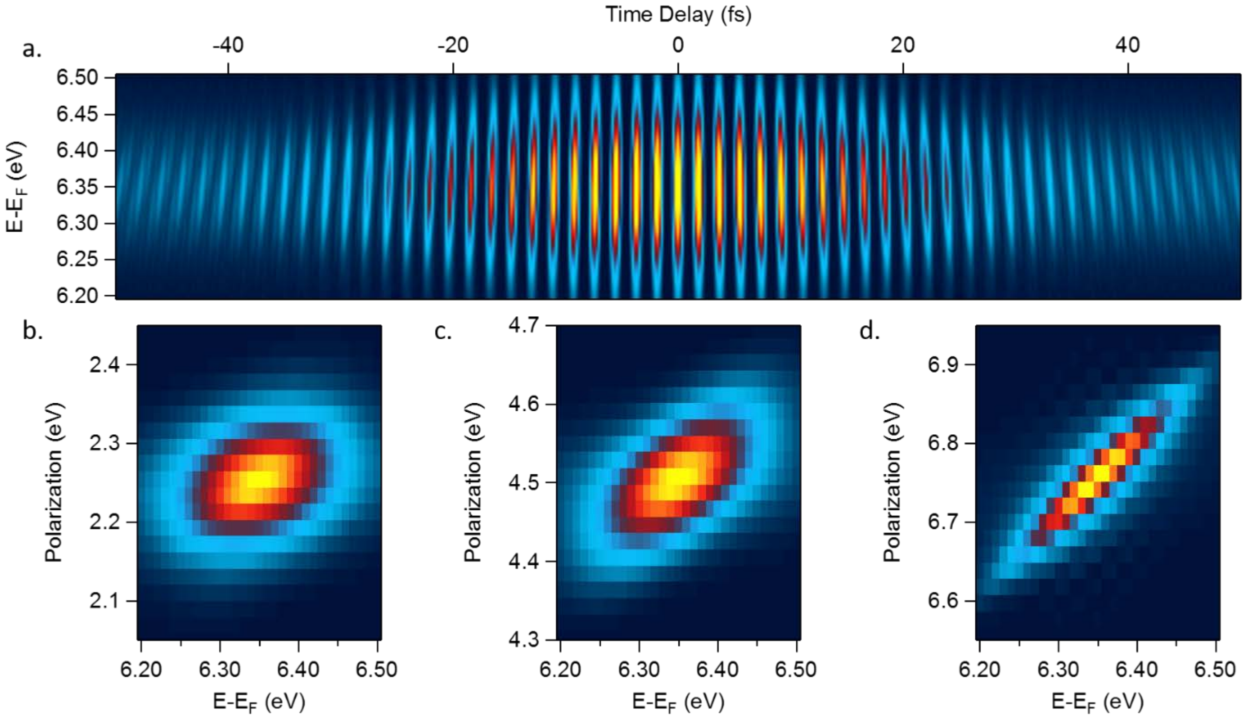

Figure 3-6 3PPE Simulation – Image

In interferometric multi-photon photoemission spectroscopy, the I2PC scans are simultaneously measured for a 2D array of final state energies and parallel momenta. Thus, the data are three-dimensional. Figure 3-6a shows a simulated interferogram for a range of final state energies from 6.20 to 6.50 eV. In a 3D data set, it would represent the interferogram for a particular momentum. The salient feature of Figure 3-6a is that in a coherent process the interference fringes away from zero delay are tilted. The tilting is caused by coherence where a particular final state energy E_f is excited dominantly by a coherent polarization corresponding to the frequency of $E_f/3$. If all the frequencies in a laser pulse could contribute incoherently to a particular E_f independently of one another, the fringes would be vertical for all delays. The same aspect of coherence is again demonstrated in Figure 3-6b to Figure 3-6d, which shows the Fourier Transform of the interferogram in Figure 3-6a. In the Fourier Transformation plots the tilting fringes in Figure 3-6a translate into tilted ellipses for the different Fourier components contributing to the interferogram.

4.0 3DCPES ON SILVER SURFACE

In this chapter, I will describe our discovery of transient excitons (TE) at the Ag(111) surface[45]. We perform mPP spectroscopy of a clean Ag(111) surface[60,61] with tunable laser excitation with from 300 to 1000 nm. The main spectroscopic features observed in this range are the SS and IP states, which are well known from the published literature[61–64]. When the laser is tuned to resonate one, two, or three photon resonances between SS and IP states, however, we observe a new feature, which we attribute to a TE.

4.1 TE ON Ag(111) BY VISIBLE LIGHT

An exciton[65,66], to put it simply, is composite quasiparticle of a positive hole and an electron, bound by the Coulomb potential. It is a solid-state analog of a H atom (see Figure 4-1), where the proton of a H atom is replaced by a hole in the crystal, the effective electron and hole masses are different from a free electron and proton, and the Coulomb interaction is attenuated by the dielectric screening of the crystal[24]. These differences are expressed in the equations for the eigenvalues of an H atom (Equation 4-1) and an exciton (Equation 4-2). The mass of H atom m, a multiplier factor contained in 13.6 eV in Equation 4-1, is replaced by the reduced mass m^* in Equation 4-2. The reduced mass m^*, explained in Equation 4-3, is the harmonic mean of electron and hole mass. And, the dielectric function, due to polarizing nearby atoms, should also be taken into consideration. In addition to the eigenstate spectra, the exciton radius, a_{ex}, is enhanced according to Equation 4.4 with respect to the Bohr radius, a_0.

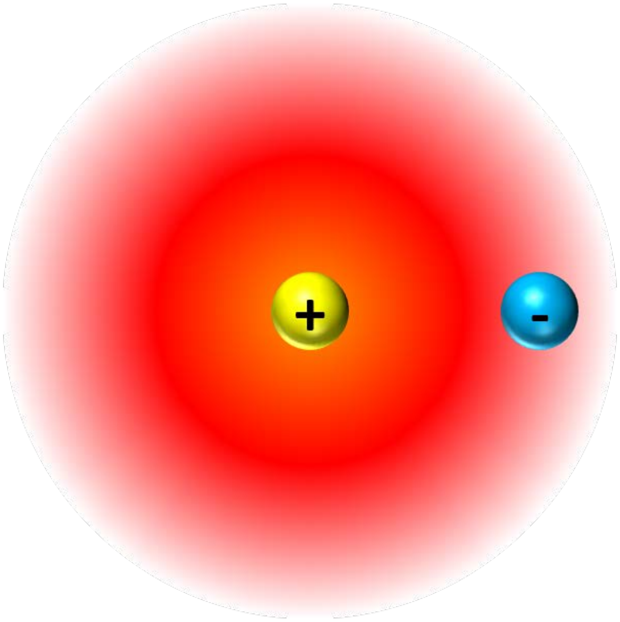

Figure 4-1 H-atom, or Exciton

$$E_n = \frac{13.6\ eV}{n^2}, n = 1,2,3, \dots \tag{4.1}$$

$$E_n = \frac{m^*}{m}\frac{1}{\varepsilon^2}\frac{13.6\ eV}{n^2}, n = 1,2,3, \dots \tag{4.2}$$

$$\frac{1}{m^*} = \frac{1}{m_e} + \frac{1}{m_h} \tag{4.3}$$

$$a_{ex} = \frac{m}{m^*}\varepsilon a_0 \tag{4.4}$$

Figure 4-1 suggests that an exciton is composed of a negative charge (the blue ball) that is bound to a positive charge (the yellow ball) by the Coulomb Potential (circle colorful bands changing from yellow passing red to white at the end). This should not be interpreted that the exciton is composed by two elementary quasi-particles, an electron and a hole. Actually, an exciton is a collective excitation[24], instead of a dressed particle. Consider a typical insulator. A quasiparticle excitation is to remove an electron from an occupied state (valence bands) and to put it on the unoccupied state (conduction bands). An exciton excitation is much more complex: it is a localized excitation, and therefore to create it from dispersive valence and conduction bands requires their superposition or a wave-packet. The Coulomb interaction between the electron and hole wave packets will reduce the excitation energy with respect to the valence and conduction bands. So, the wave function of an exciton is written as Equation 4.5, where on the right the state has an electron with K_e in conduction band and a hole with K_h in valence band and Bloch function Ψ_{K_e,K_h}, and the sums are performed over all K values of the coupled bands[65] with the restriction of Equation 4.2. In Equation 4.2, r is the relative distance between the electron and hole. When the exciton is created by light, owing to momentum conservation and the very small amount of momentum of a photon, K of the exciton is approximately 0.

$$|K,r\rangle = \sum_{K_e,K_h} \Psi_{K_e,K_h} |K_e;K_h\rangle \tag{4.5}$$

$$\mathrm{K} = K_e + K_h \tag{4.6}$$

$$\mathrm{K} \approx 0 \tag{4.7}$$

Excitons are known in molecules, insulators, and semiconductors[65–67]. For metals, there are several publications discussing the existence from theory, but the experimental evidence was lacking until we presented the first direct evidence for the Ag(111) surface. The general belief that metals do not support excitons comes from the fact that the screened Coulomb potential in metals does not support bound states[68]. Owing to the electrons' freedom to move in metals, a positive charge will be screened by the sea of electrons, such that the effective potential is described by the Equation 4.8. For different combinations of parameters λ and q, the potential shape changes accordingly. Computation and simulation show that there exists a critical value of the screening parameter $q_c(\lambda)$, for larger than which there are no bound states[69]. Metals are materials for which the screening length is sufficiently small that free electrons are not localized in bound states by Coulomb interactions even at 0 K[24].

$$V(r) = \frac{-\lambda}{r} e^{-qr} \tag{4.8}$$

Though the above Yukawa potential does not support stationary excitons in metals, it does not exclude the possibility that excitons exist before the screening is fully saturated. There are several theoretical publications discussing this transient regime of TE. In 1967, Mueller and Phillips[70] discussed that one should include the Coulomb interaction terms between electron and hole pairs and polarization terms to reproduce the intensity of the interband absorption threshold in copper at ~2.0 eV. More recently, in 2000, Schöne and Ekardt[71] discussed the transient excitons (TE) for a jellium model and the realistic band structure of Cu in order to explain its anomalous hot electron lifetimes; in 2002[72], they discussed TE again in Ag and Au. In their theory, the localization of holes in d-bands of noble metals is important in forming TE. In 2003, Marini and Sole[73] demonstrated that dynamical excitonic effects are important in the calculation of the dielectric functions of noble metals to obtain good agreement with the experimental absorption spectra. Finally, in 2010, Gumhalter[74] et al. discussed the formation of TE composed of SS-hole and excited electron, and the evolution of TE into IP state. Gumhalter's work anticipated our discovery, shown in Figure 4-2, and discussed in the following.

Figure 4-2 displays the dynamical process of TE evolution into IP in our experiments. The Ag(111) surface has a band gap[75] for a wide range of $k_{||}$ momenta between the LSP and USP. Between LSP (violet horizontal line and violet bulk) and USP bands (red horizontal line and red bulk), there exists a SS band (blue horizontal line). We excite Ag(111) with laser pulses (vertical yellow arrows) in the visible range to perform 3PP to investigate the excitation pathways for SS and IP surface bands (horizontal bar on the right colored yellow-green). The SS corresponds to a 2D electron gas that is confined to the metal surface. The IP states are not preexisting features of the surface band structure; they are created through the retarded many-body screening of an electron introduced in front of the surface. Because the IP state does not exist before the interaction, there is no dipole moment between SS and IP, and therefore no optical coupling between them.

The USP band provides the optical coupling by which we excite electrons from the SS band. The absorption of a photon creates a hole in the SS band and an electron that is split off from the USP band; at the instant of excitation the electron and hole interact through the bare Coulomb interaction to form a series of Rydberg-like excitonic states. Solving the Schrödinger equation for this scenario, yields the eigen-energies of the exciton states (green horizontal bars), which converge in a quasi-continuum (green bulk) to the bottom of U_{SP} band. Above the U_{SP} band minimum, the electron is no longer bound by the Coulomb interaction. It should be noted that energy is conserved asymptotically, and the energy spectrum of the excitonic states evolves dynamically on the screening time scale; therefore, the excitonic spectrum does not survive to be imprinted on the measured mPP spectra.

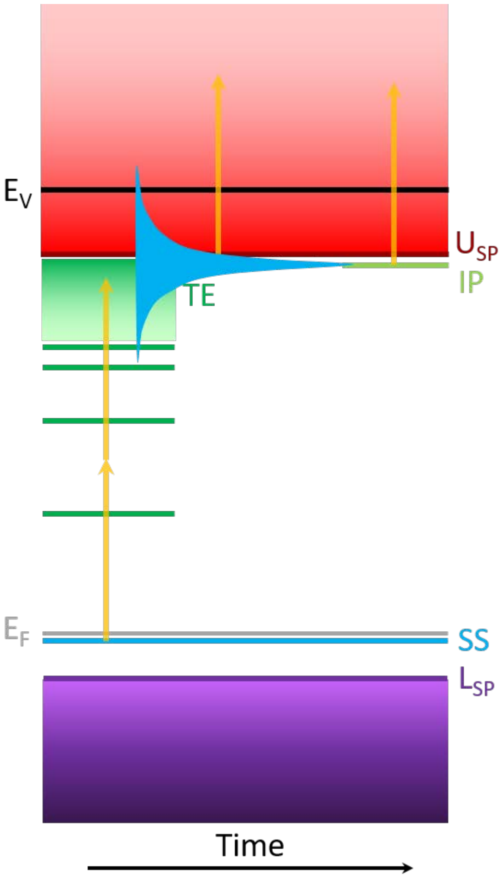

Figure 4-2 Excitation scheme of IP states via TE

The creation of excitons turns on the charge density fluctuations of the free electron sea that screens the Coulomb potential. As the screening saturates, the hole and electron evolve to their fully screened states, namely a hole in the SS and electron in the IP band. Any component of the initial polarization must either: 1) terminate in the energy conserving IP band; 2) be excited further to the free electron continuum above the E_v; or 3) be reemitted as a photon. According to the theory[74] by Gumhalter et al. the saturation of screening at a silver surface is completed in about 15 fs, whereas at a copper surface it is about 2 fs. So armed with ~15 fs duration of laser pulses, we are able to access the transient screening regime for the Ag(111) surface.

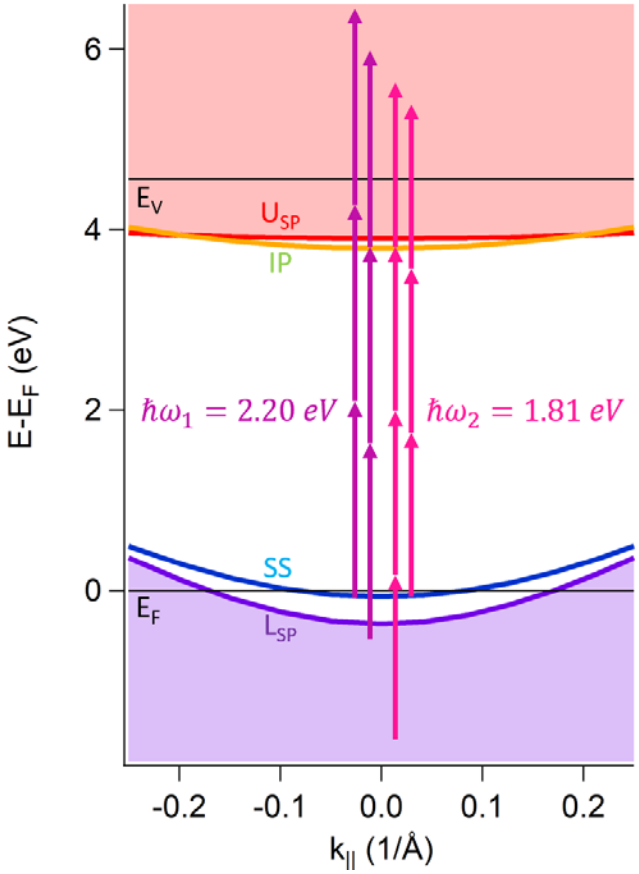

Figure 4-3 Ag(111) band structure with respect to $k_{||}$

Figure 4-3 shows the band structure of a Ag(111) surface with respect to the parallel momentum. A band gap, already implied in Figure 4-2, between L_{SP} (violet curve) and U_{SP} (red curve) extends from -0.4 eV to 3.9 eV for $k_{||}$= 0 Å^{-1}. Within the gap, SS and IP, with minima at -0.063 eV and 3.79 eV and effective mass of $0.4m_e$ and $1m_e$, respectively, form quantum wells in the metal/vacuum interface. The SS band crosses Fermi level at $k_{||}$= $\pm$0.07 Å^{-1}. The vertical arrows show the excitation paths for observation of SS and IP bands in 3PP and 4PP processes with different excitation wavelengths. We tune the excitation wavelength from 2.20 eV (violet vertical arrows) to 1.81 eV (pink vertical arrows) to excite Ag(111); this corresponds to exciting from above to below the two photon resonance from SS to IP state at 1.93 eV..

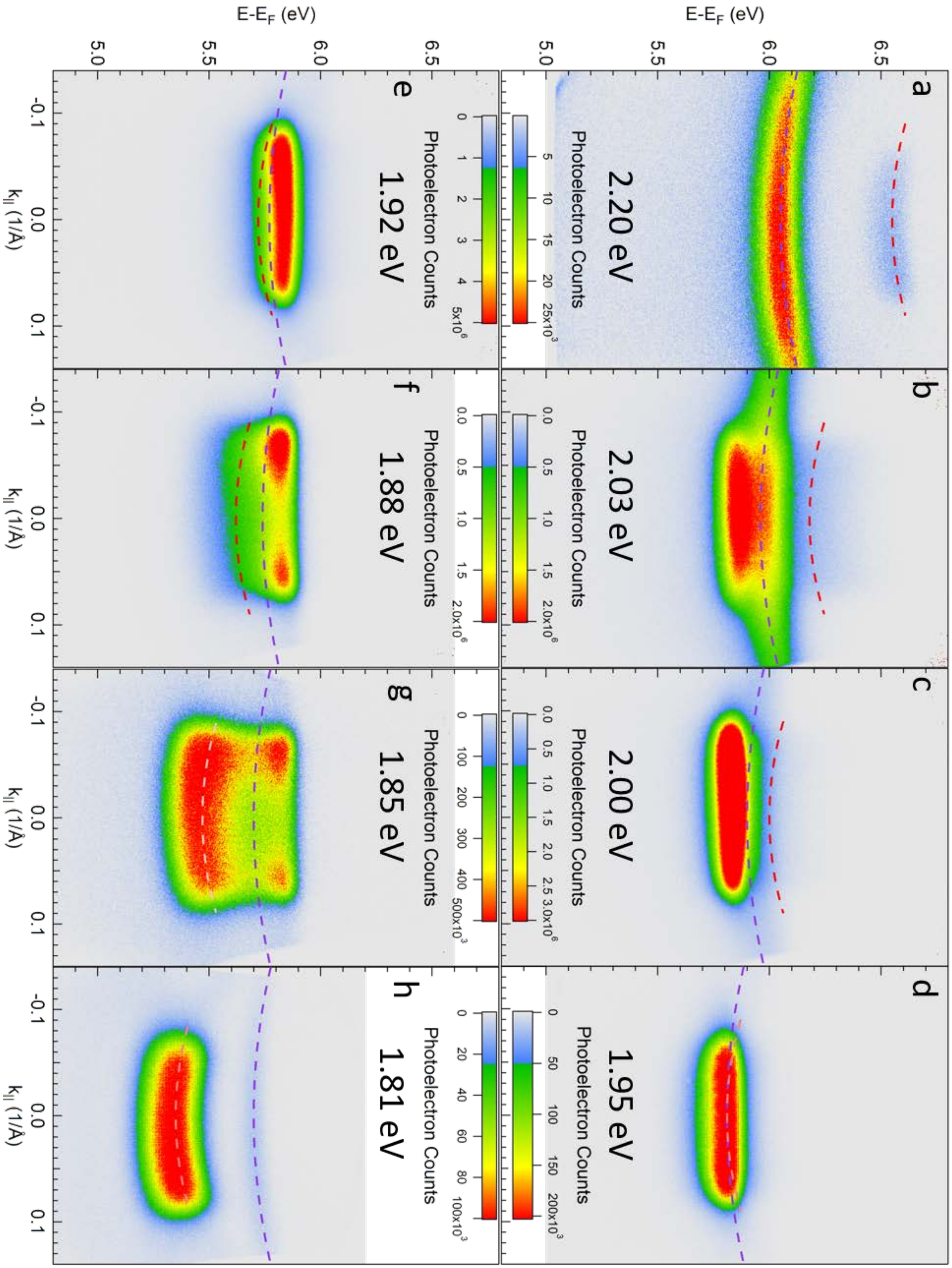

Figure 4-4 Photoemission spectra when tuning photon energy across 2 photon SS to IP resonance

Figure 4-4 displays the experimental results of energy and momentum resolved spectra. SS is marked with red or light red dash curve with limited extension over parallel momentum, and IP is marked with purple dash curve with much wider extension over parallel momentum. SS has a larger curvature due to smaller effective mass of $0.4m_e$ compared with the IP effective mass of $1m_e$. The energy positions of SS and IP are predicted by the band structures in Figure 4-3 combined with the excitation photon energy.

When the two photon SS to IP resonance at $\hbar\omega_{res} = 1.93 \pm 0.02\ eV$ is outside of the bandwidth of the excitation laser spectrum, we observe only the SS and IP features in the photoemission spectra (see Figure 4-4a & Figure 4-4h). However, when the excitation laser spectrum overlaps the resonance $\hbar\omega_{res} = 1.93 \pm 0.02\ eV$, a new photoemission spectral feature emerges. It has the following salient properties:

1. It is not dispersive with parallel momentum implying an infinite effective mass, or strong localization.
2. It has the same parallel momentum range as the SS.
3. Its intensity dominates over other features like the SS and IP bands, suggesting transition moment enhancement.
4. It appears at a constant final state energy of $E_{final} = 5.82 \pm 0.03\ eV$, as the excitation photon energy is tuned between 2.03 to $1.85\ eV$. Such behavior could be caused by a final state at $5.82\ eV$, but we know for the Ag(111) surface it does not exist, and therefore, must have a different explanation.

Those features are unique, and have not been observed on other metals where band structures like SS and IP appear; they can be explained, however, with the concept of a transient exciton (TE).

The TE is a localized superposition state composed of all the occupied SS states below the Fermi level and the corresponding electrons split off from the U_{SP}, whose parallel momentum range is limited by Equations 4.6 and 4.7. To create the localized TE state requires the entire parallel momentum range of the occupied SS band. The TE wave function is given by Equation 4.5, which implies that its transition moment derives the enhancement from the summation over all the available interband transitions between the SS and U_{SP} bands.

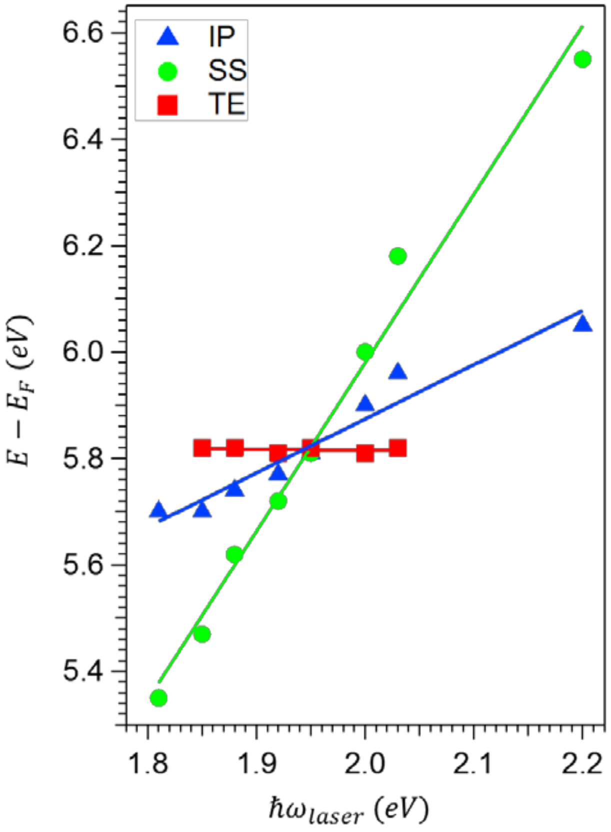

Figure 4-5 Tuning photoemission features with photon energy

We performed interferometric time-resolved measurement to investigate TE on Ag(111) with $\hbar\omega_{laser} = 2.05\ eV$; the excitation wavelength has $\Delta = 2\hbar\omega_{laser} - \hbar\omega_{resonance} = 0.12\ eV$ detuning from the SS to IP state two-photon resonance. For this detuning the 3PP spectra show distinct SS, IP and TE features. A 3DCEPS measurement creates a movie of E(k) distributions as a function of pump-probe delay. Figure 4-6 displays a cross section through a 3DCEPS movie for $k_{||} = 0\ \text{Å}^{-1}$. Figure 4-6a shows photoemission counts for different final state energies and time delays. Figure 4-6a is an enlargement of a part of Figure 4-6b, in the time delay range from 0 fs to 40 fs; it shows that the signal for different final energies oscillates with a different period, as is expected for a coherent process. Figures 4-6c to 4-6e are line-profiles at the energies corresponding to of SS, IP and TE states, respectively. The beating of IP and TE polarizations indicates that there are complex components contributing to the coherent photoemission process. The distinct time evolutions of SS, IP and TE states mean they have different polarization dynamics in the photoemission processes.

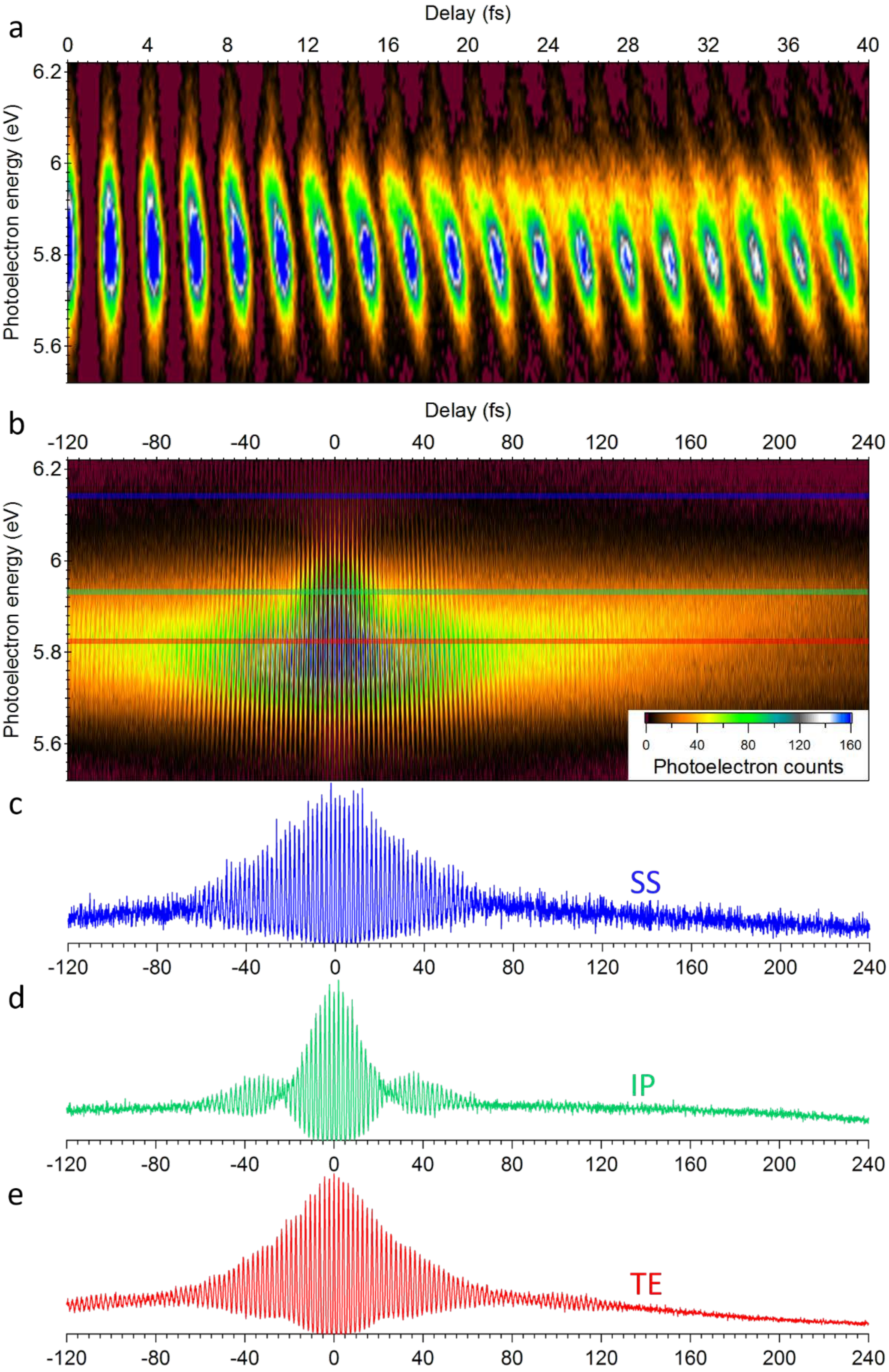

Figure 4-6 Time resolved photoemission spectra for $k_{\|}=0$

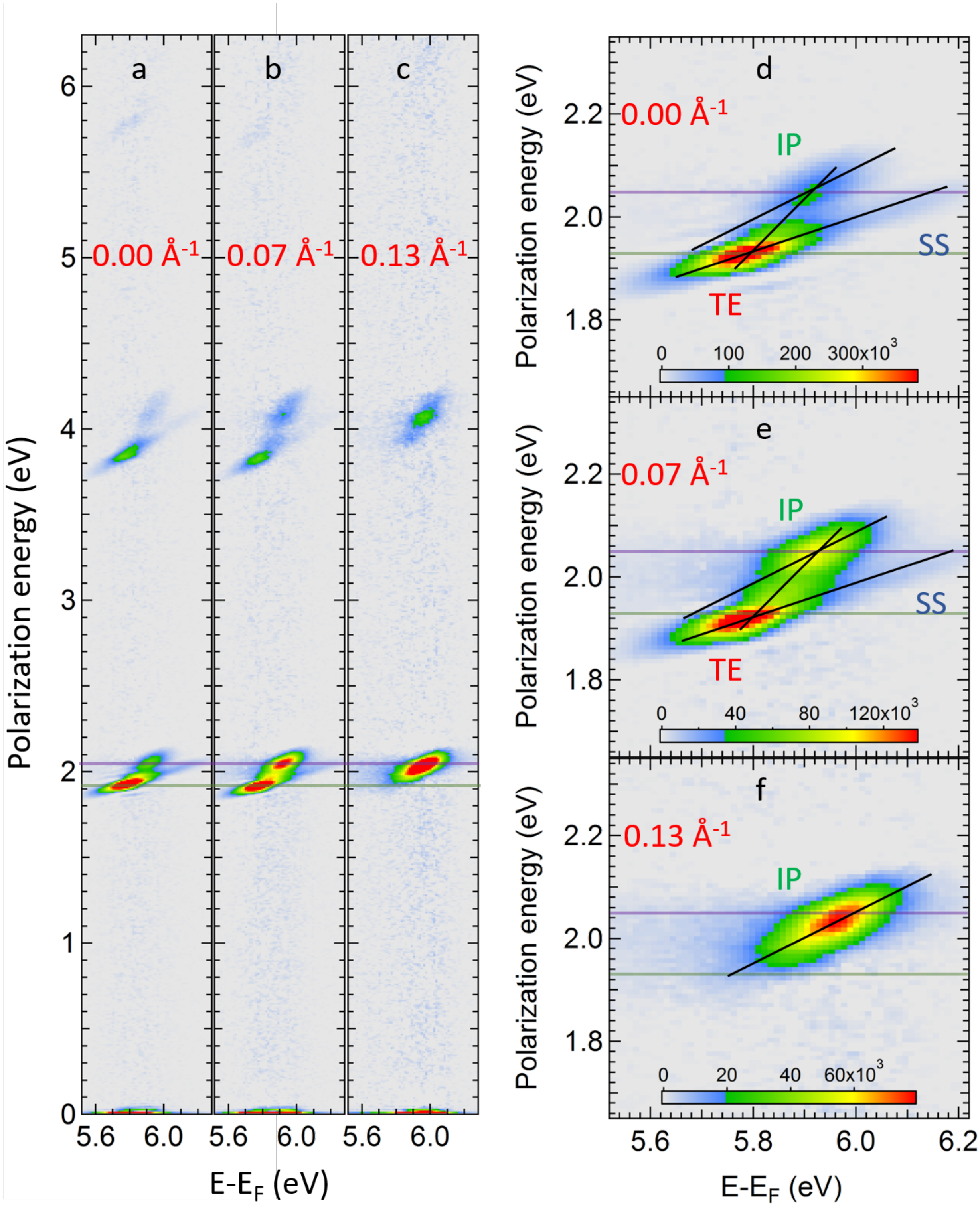

Figure 4-7 2D electronic spectra showing the correlation between polarization energy and final energy

Instead of evaluating the dynamics for every single final state energy, we analyze the co-relationship between SS, IP, and TE signals and the coherent polarizations that contribute to their excitation by performing a Fourier Transformation of the time domain signal to obtain the 2D spectra in Figure 4-7. The oscillatory signal in the time domain represents the frequencies of the coherent polarization fields that give rise to the photoemission signals. Figure 4-7a to Figure 4-7c show the 2D spectra for $k_{||} = 0.00,\ 0.07,\ 0.14\ \text{Å}^{-1}$, respectively. These 2D spectra have significant amplitudes at the integer number (0, 1, 2, …) times of the photon energy, because the dominant coherent response is at the driving frequency, its harmonics, and the rectified frequency. The driving frequency, $\hbar\omega_{laser} = 2.05\ eV$, is marked with light violet horizontal line in each of the 2D spectra, while $\hbar\omega_{resonance} = 1.93\ eV$ is marked with light green horizontal line. The most interesting information about the coherent polarization can be found in the at the fundamental of the laser frequency. For $k_{||} \leq 0.07\ \text{Å}^{-1}$, the observed coherent response mainly occurs at $\hbar\omega_{resonance}$ instead of $\hbar\omega_{laser}$. Similar information is observed again at the second harmonic of the laser frequency. The information at the third harmonic is too weak to consider, and no response is observed at the fourth and further higher harmonics in repeated measurements.

Next, we consider the responses at the fundamental frequency for the selected $k_{||}$, which are enlarged in Figure 4-7d to Figure 4-7f. The contributions to the 2D spectra from TE, IP and SS are identified by their final energies, which are known from the energy-momentum resolved spectra, such as in Figure 4-4b. The TE and SS signals have a limited $k_{||}$ range, and therefore do not appear in Figure 4-7f. The polarization and final energy of TE is nearly constant for $k_{||}$ in Figure 4-7d and Figure 4-7e. The IP shifts to higher final energy from Figure 4-7d to Figure 4-7f due to its dispersion, but it barely moves along the polarization axis. The SS and IP states amplitudes have the intensity centered at $\hbar\omega_{laser} = 2.05\ eV$, while TE state has its intensity at $\hbar\omega_{resonance} = 1.93\ eV$ instead. Thus, the 2D spectra tell that the TE signal is excited by $\hbar\omega_{resonance}$, which is solely determined by the band structure of Ag(111), rather than by the external laser field. This explains why the TE does not tune with the laser photon energy. The 2D spectra also show that even with a detuning as large as $\Delta = 0.12\ eV$, local field at $\hbar\omega_{resonance} = 1.93\ eV$ dominates the photoemission processes. The polarization at $\hbar\omega_{resonance}$ is generated by the external field within the wings of its broad spectrum. The excitonic response of the Ag(111) surface generates a local excitonic field. Thus, the observed mPP process is a product of the laser polarization that varies on the optical wavelength scale and the excitonic polarization that is enhanced by the many-body response of the sample and oscillates on the atomic scale. This local field enhancement enables the near resonant excitonic response overwhelm the response at the driving laser frequency.

Another interesting feature of the 2D spectra is that the TE, IP and SS spectral features are shaped like tilted ellipses. The slope the main axis of TE and SS ellipses is 1/3, which is a sign of a coherent three-photon photoemission process. Because it is retarded in time, the IP state cannot participate in the coherent three-photon process. Electrons in the IP state are created by laser pulses in a coherent two-photon process, and the 2D spectra feature of the IP state displays the slope of its main axis as 1/2. This channel exists for IP states of any parallel momentum and is not associated with the excitation out of SS. In addition to this channel, a feature in the 2D spectra connects TE to IP with slope of 1 shows another channel where the IP signal emerges from TE signal and is photo-emitted by a subsequent one-photon process. This corresponds to the TE evolving into the IP state. Within the band gap of Ag(111), the TE can dephase into an energy conserving state only at the IP energy. The non-adiabatic screening process can transform the primary exciton to a real excitation of the surface only at the IP state energy, where the IP state is the asymptotically evolved state of the screening process.

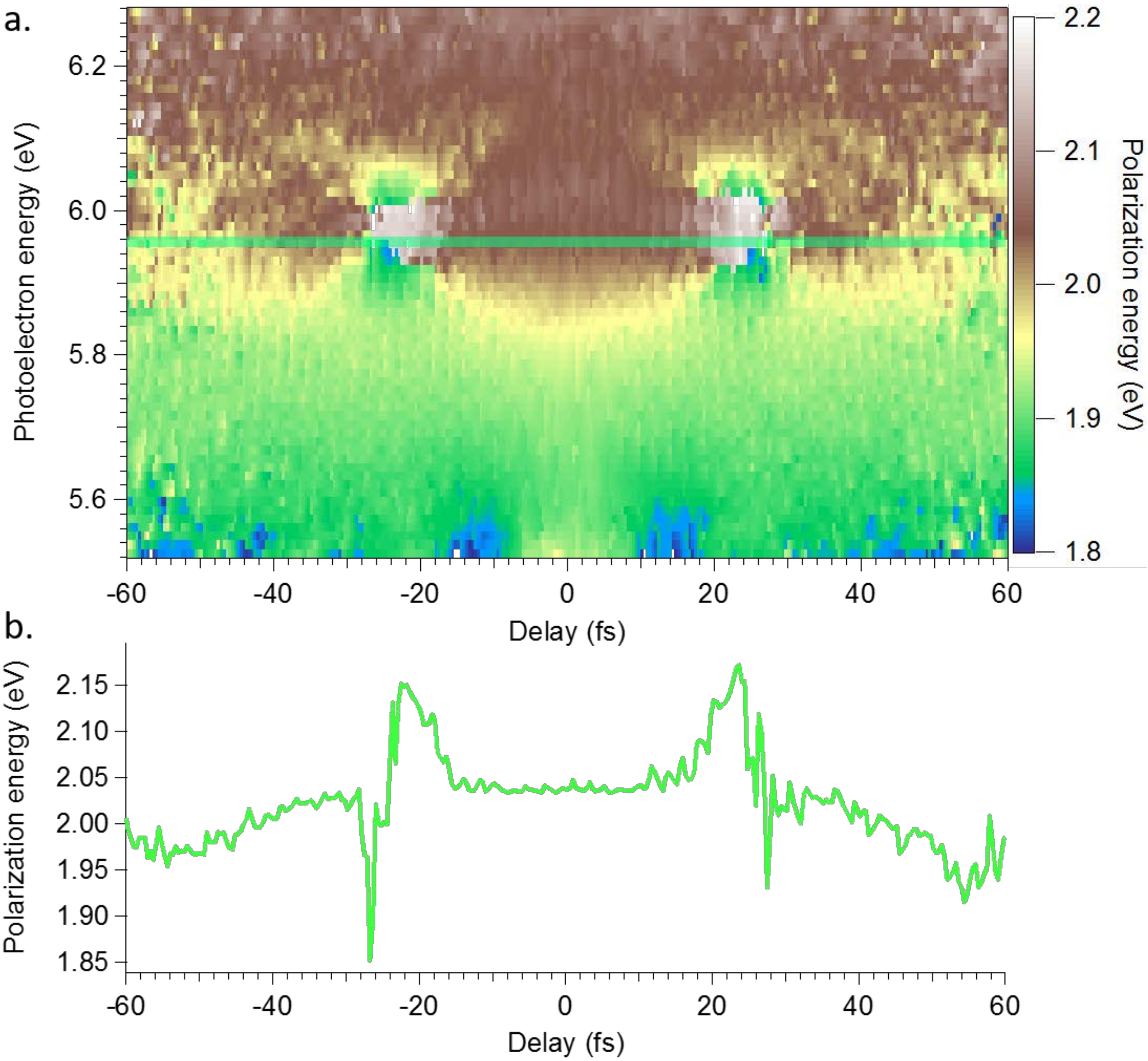

Figure 4-8 Polarization energy evolution for different photoelectron energies and delay times

An alternative way to present the experimental results is shown in Figure 4-8. Figure 4-8a shows the time-windowed frequency analysis[76] of the interferogram in Figure 4-6b. The x, and y axes are the time delay and photoelectron energy, respectively; however, the intensity or color axis is the polarization energy from a time-windowed Fourier transform analysis instead of photoelectron counts. A line profile for IP state is shown in Figure 4-8b. It shows that the IP state photoelectron is initially driven by $\hbar\omega_{laser} \approx 2.05\, eV$. However, $\hbar\omega_{laser}$ this only happens while the laser is on, i.e., for $< 20\, fs$. At longer delays, the frequency tends to the $\hbar\omega_{resonance}$, which overtakes and dominates the photoemission process. The singular point around ($\pm 20\, fs$, $6.0\, eV$) in Figure 4-8a corresponds to the polarization beating, when the two frequencies are out-of-phase and have comparable amplitude. Because of the destructive interference the frequency analysis cannot give a well-defined frequency at these singular points. The beating is also observed in Figure 4-6d.

4.2 TE ON Ag(111) BY ULTRAVIOLET OR INFRARED LIGHT

In the last section, transient excitons are created at Ag(111) surface by near-resonant SS to IP state two-photon transition. Similar phenomena could potentially be observed with one or three photon resonances. In this section, I will present the results of such experiments.

Figure 4-9 shows the momentum resolved photoemission spectra of Ag(111) excited by ultraviolet laser with wavelength and photon energy marked. The blue and red curves are the expected IP and SS state dispersions, respectively, predicted by the common values of the state minima and effective masses, and displaced by adding one or two photon energy. In addition to the SS and IP states, there is also an extra feature that does not tune with the photon energy, which is marked with the yellow bar; this is the TE.

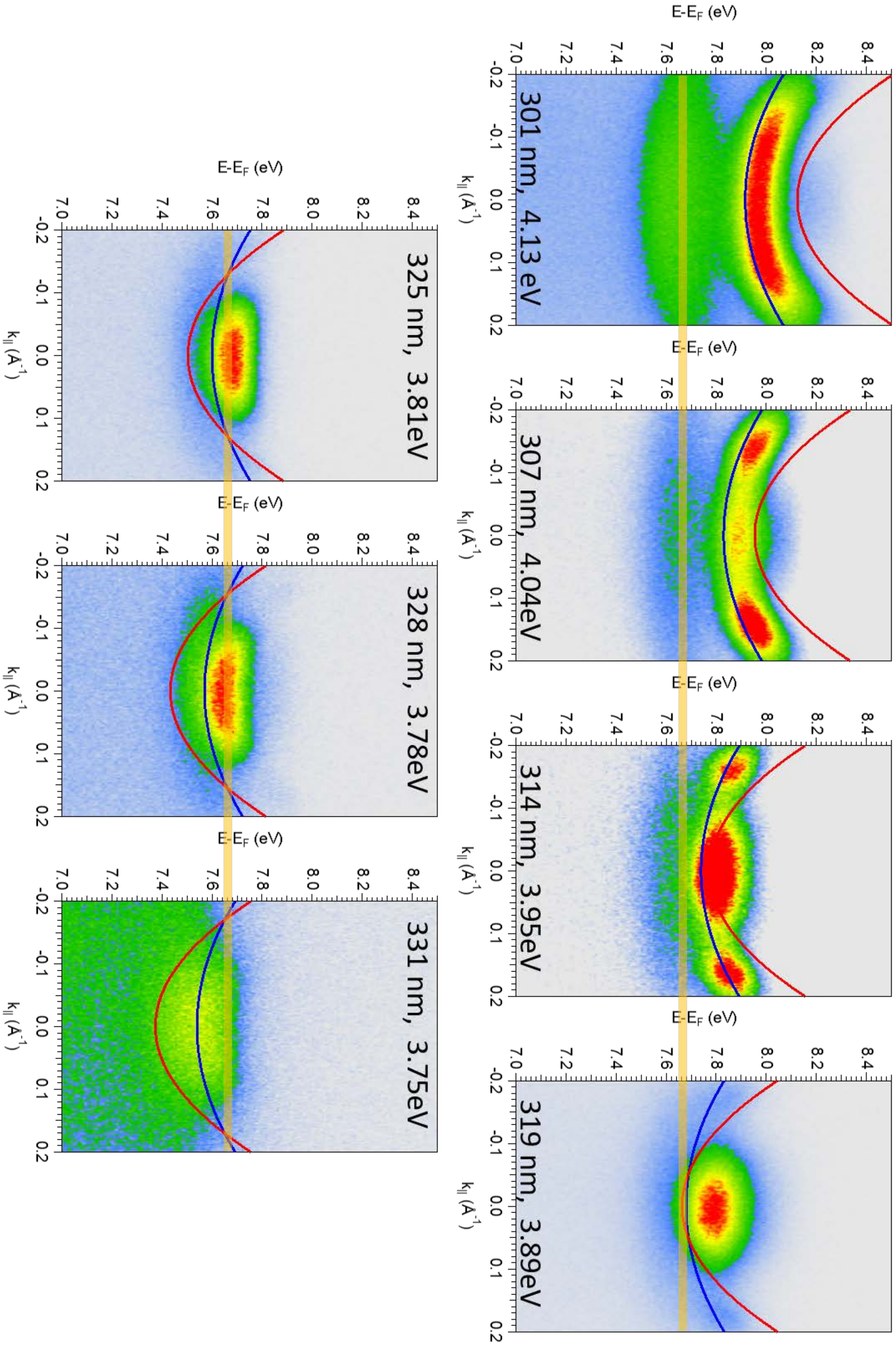

Figure 4-9 TE by ultraviolet laser

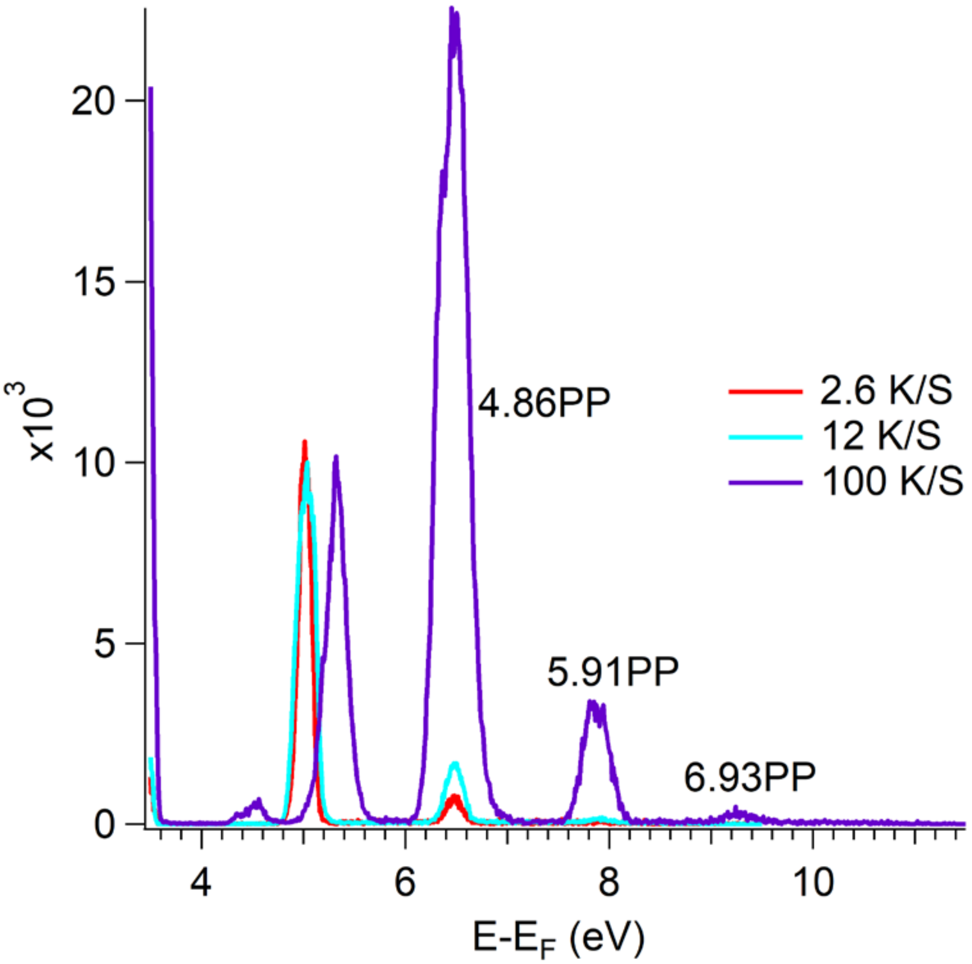

Figure 4-10 High order TE when increasing the laser fluence

Figure 4-10 shows the line profiles of mPP spectra at $k_{||} = 0\ \text{Å}^{-1}$ of Ag(111) when it is excited by 920 nm (1.35 eV) light, which near the three photon resonance between SS to IP. The experiments are taken under different laser intensities, and cause the increase of counts rate from 2.6 K/S to 12 K/S and to 100 K/S. The peaks correspond to different orders of TE. The higher orders would normally be interpreted as above threshold photoemission[77–80]. For higher orders $(m > 4)$, the peaks appear very close to energies corresponding to absorption of an integer number of photons from SS. However, the TE energy close to 4PPE is fluence dependent. The underlying reason could be space charge or the onset of non-perturbative effects, and needs further investigation.

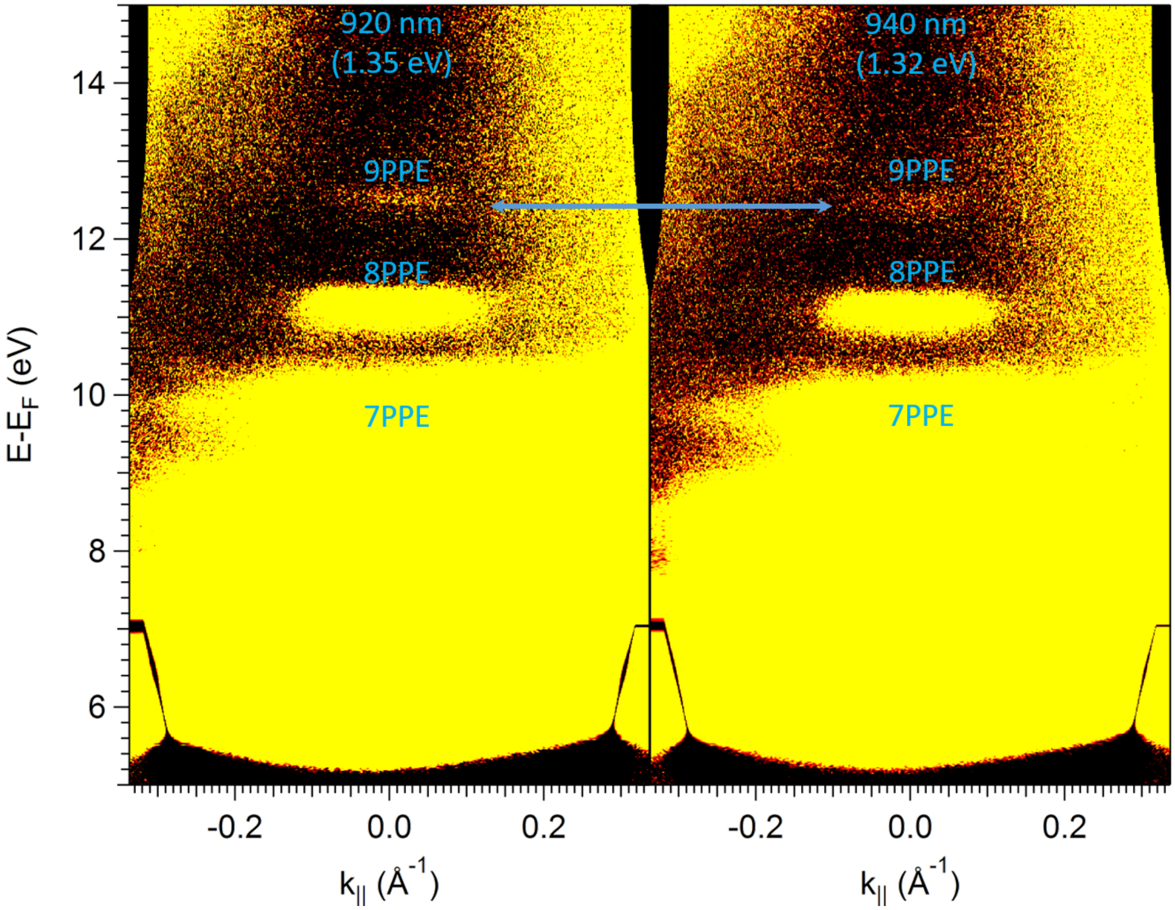

Figure 4-11 TE by infrared laser

Figure 4-11 shows the comparison of momentum resolved photoemission spectra excited by strong intensity laser of two different infrared wavelengths. And we are again able to find the characteristic properties of the TE states:

1. The TE spectra are straight, i.e., non-dispersive.
2. The parallel momentum range of TE states is limited to that of the occupied part of SS.

3. The excitation of TE states is enhanced. And, the enhancement enables us to observe up to 9PPE.
4. The energies of TE states do not tune with the laser photon energy, as demonstrated by comparing the energy positions with 920 and 940 nm excitation.

5.0 3DCPES ON COPPER SURFACE

In last chapter I discussed photoemission studies of a Ag(111) surface. In this chapter, I will present the mPP results from copper surfaces[37,81–87]. Copper and silver have similar electronic band structures[24,25]. The most distinct feature of copper is the copper color, which comes from the relatively shallow d-bands (-2.0 eV) of copper[88] as compared with 3.8 eV for Ag. The possible excitation of the d-bands will yield some interesting results.

5.1 (111) SURFACE OF COPPER

5.1.1 Cu(111) excited by UV light

We performed a time-resolved measurement with a 393 nm (3.15 eV) at Cu(111) surface to study dynamics of the polarization field.

In Section 2.3, the method of the interferometric time-resolved measurement[11,46,89,90] was introduced. We control and automate the time delay between two pulses by applying a linearly rising voltage to piezo-system, integrate the energy-momentum spectra for 12 ms for each time delay during each scanning, and repeat 400 times scanning for a typical measurement. In this set of measurements, we slightly change the way we perform the time-resolved measurements. The change of the time delay between the two identical pulses causes interference between them, which can be recorded with an optical spectrometer. Specifically, if the time delay is N (N is an integer number) times of the period of laser pulse carrier frequency, we expect a constructive interference between the laser pulses at the carrier wave frequency; similarly, if the time delay is N+0.5 times of the period of laser pulse carrier frequency, we expect a destructive interference between the laser pulses carrier wave frequency. We can achieve constructive or destructive interference by translating a pair of mirrors in the Mach-Zehnder interferometer (see Figure 2-5), and identify the delay between the two pulses by monitoring their laser interference spectra.

The time resolved method introduced here has a worse sampling of the time delay axis than the way introduced in Chapter 2, and requires extra attention to avoid careless mistakes. The benefits are that we can integrate the energy-momentum spectra for a longer time (40 s in this measurement) for every sampling time delay points, and thus we gain much better signal to noise ratio and of course better resolution in energy and momentum axis.

Figure 5-1 shows energy-momentum resolved photoemission spectra when the two pulses are perfectly in phase and out of phase. The curved band around 6.0 eV is the SS of Cu(111), and the straight line around 4.9 eV is the vacuum level. The two images of Figure 5-1 look similar, but the image with 0 delay has significant counts because of the constructive interference between the two pulse. When the delay between the two pulses is shifted by-half wavelength (π), however, the counts are rather low. Instead of interpreting the image with low counts as interference between two pulses, we can also interpret it as the inference between the polarization induced by the first pulse in the sample and the second pulse. This can be verified in Figure 5-2 and Figure 5-3.

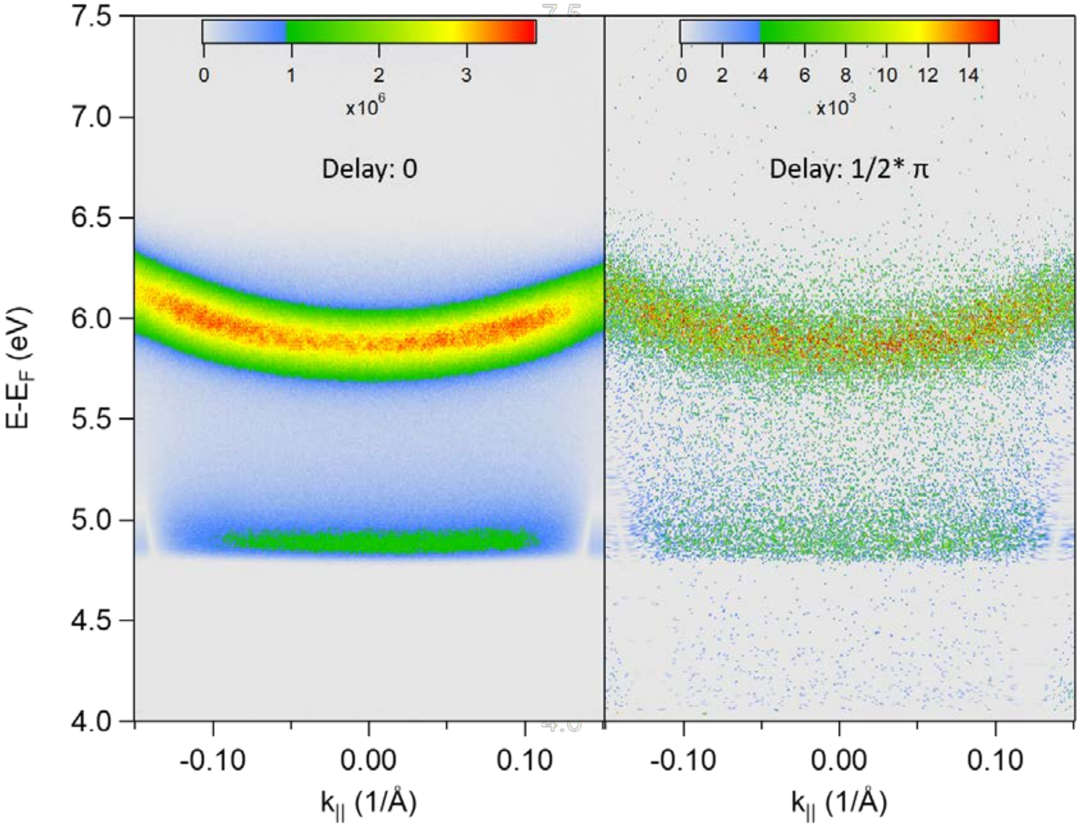

Figure 5-1 Spetra comparison at in phase and out phase

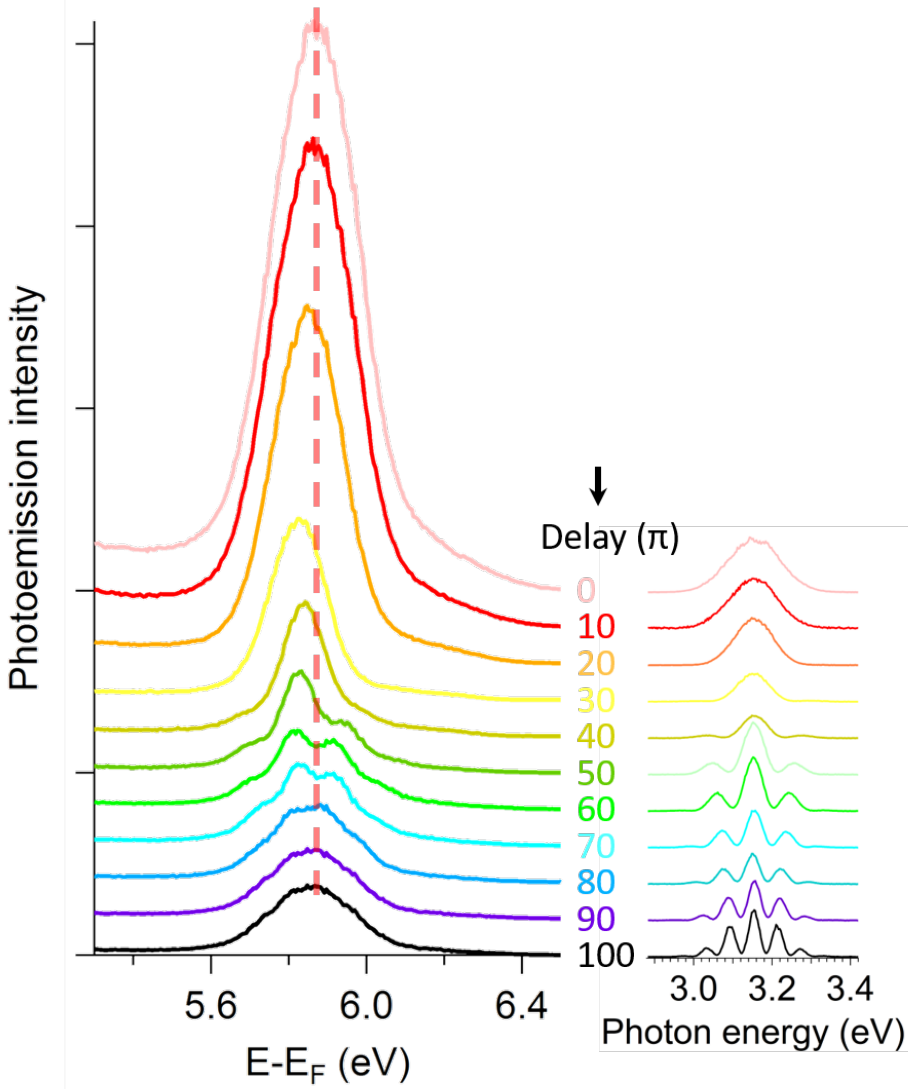

Figure 5-2 Photoemission spectra at $k_{||} = 0$ Å^{-1} for a series in phase delays and correponding laser spectra

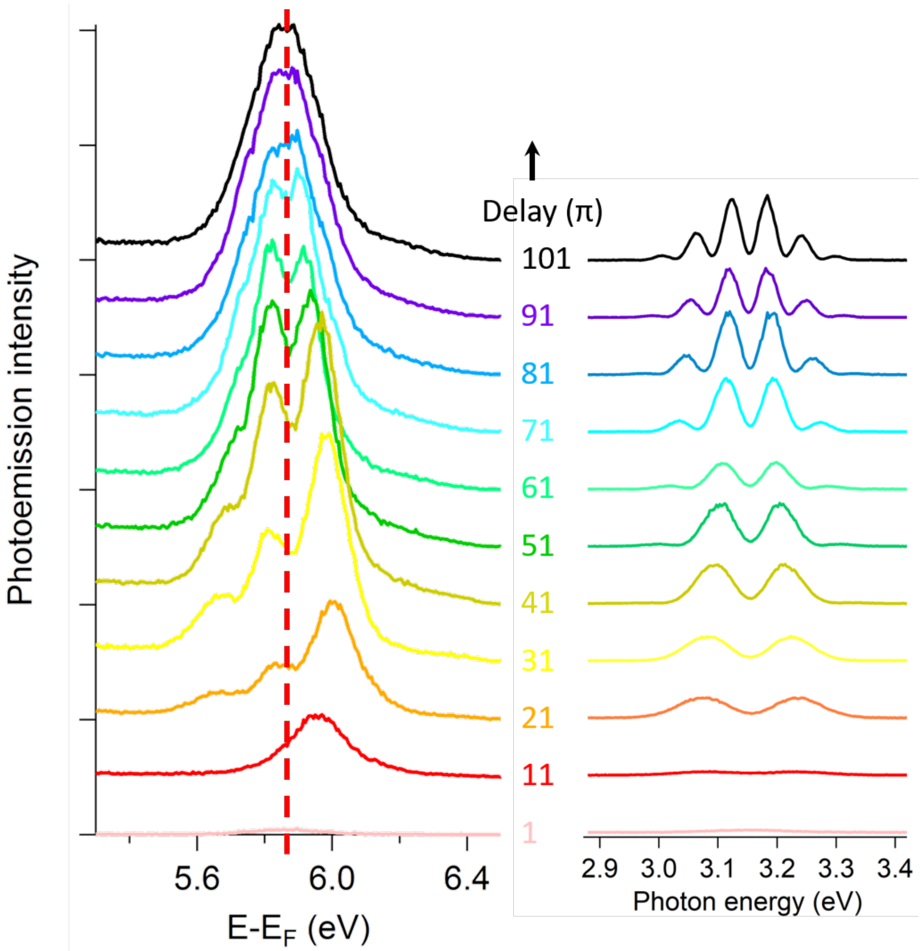

Figure 5-3 Photoemission spectra at $k_{||} = 0$ Å^{-1} for a series out of phase delays and correponding laser spectra

Figure 5-2 shows a series of 2PP spectra for normal direction. They are cut from a series of images similar to Figure 5-1. The spectra are chosen so that their time delays are integer number of optical cycles of the carrier frequency (393 nm)[47]. Also, the corresponding laser spectra of the two pulses acquired by an optical spectrometer with variable delays are shown. From the laser spectra, we learn that the interference is costructive at the carrier wavelength and the interference pattern is symmetric on both sides. But the photoemission spectra on the left is not a nonlinear replica of the optical spectra. Surprisingly, the photoemission spectra at intermediate delays do not show constructive interference at twice the center energy with symmetric interference fringes, but rather the maxima appear on the low energy side of the center energy at the intermediate time delays.

Figure 5-3 shows a series of 2PP spectra for normal emission excited by out-of-phase laser pulse pairs with the denoted time delays. On the right side of the figure are the corresponding laser spectra. As expected for out-of-phase excitation, the spectra have a minimum at their center wavelength, due to the destructive inference between the two pulses, and they are symmetric. The 2PP spectra, however, are again not symmetric, and their maxima are to the high energy side.

In elementary physics courses, we have learned about the driven oscillator, which oscillates at the driven frequency and its amplitude depends on the difference between the driven frequency and its intrinsic frequency. Here we have complex situation of a driven, transient many-body system. We are creating a coherent polarization field in the sample when we perturb it with laser pulses. This polarization field is not an instantaneous replica of laser pulse, and does not necessarily follow the time evolution of laser pulse. This polarization field, induced by laser pulse, depends on the electronic structure of the sample.

Next we perform a 3DCPES measurement on Cu(111) surface with 400 nm pulses, using the method introduced in Chapter 2.3. The interferogram of enegy-time resolved photoemission spectra at $k_{||} = 0\ \text{Å}^{-1}$, and its line profiles at $E = 6.00, 5.93, 5.80\ eV$ are shown in Figure 5-4. From the figure, we can see the coherent interference oscillation extends for a longer delay time for lower final energy than the higher. The dephasing lifetime has energy dependence.

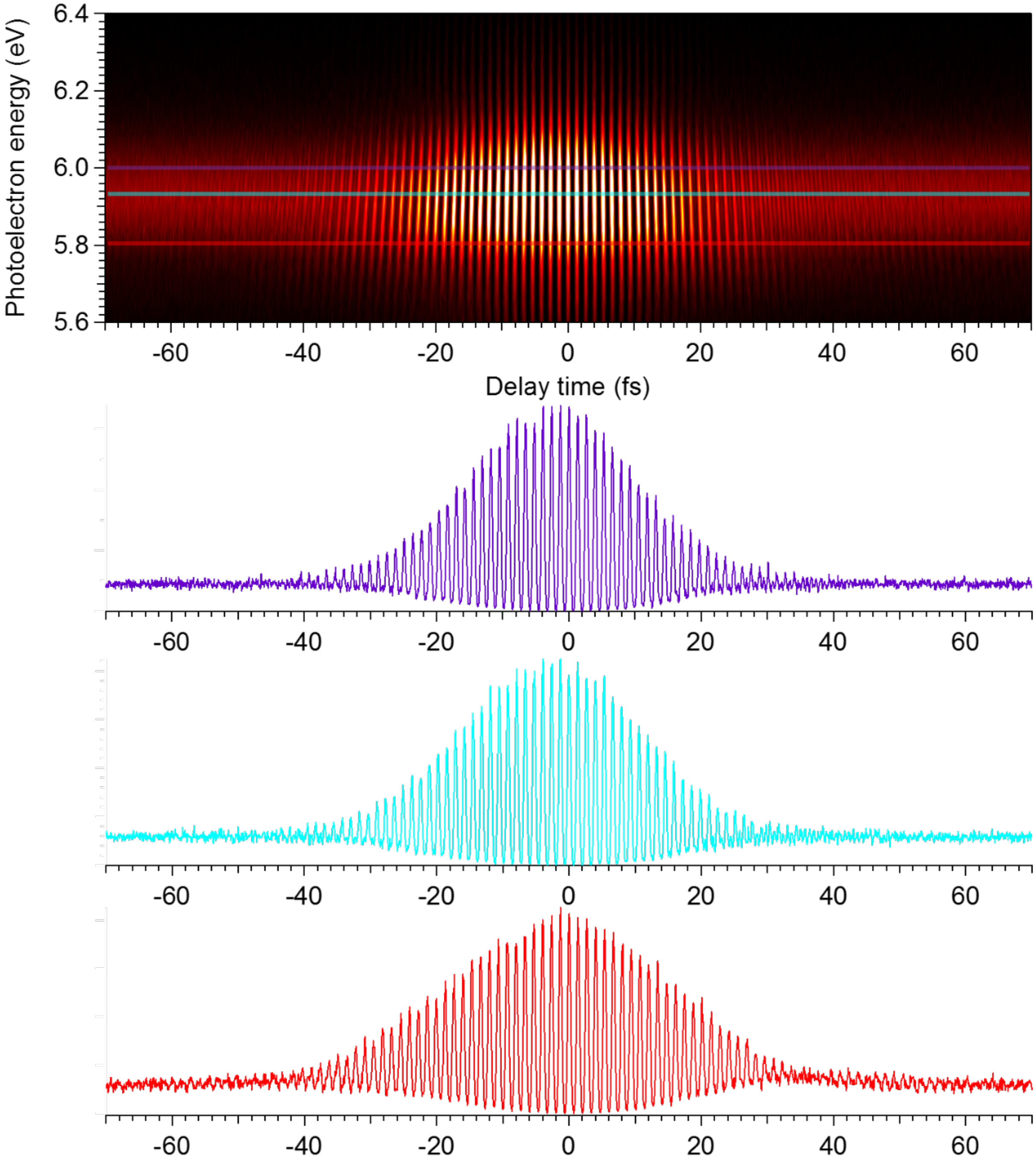

Figure 5-4 Enegy-time resolved photoemission spectra of Cu(111) excited by 400 nm at $k_{||}$ = 0 Å, and line profiles for E=6.00, 5.93, 5.80 eV

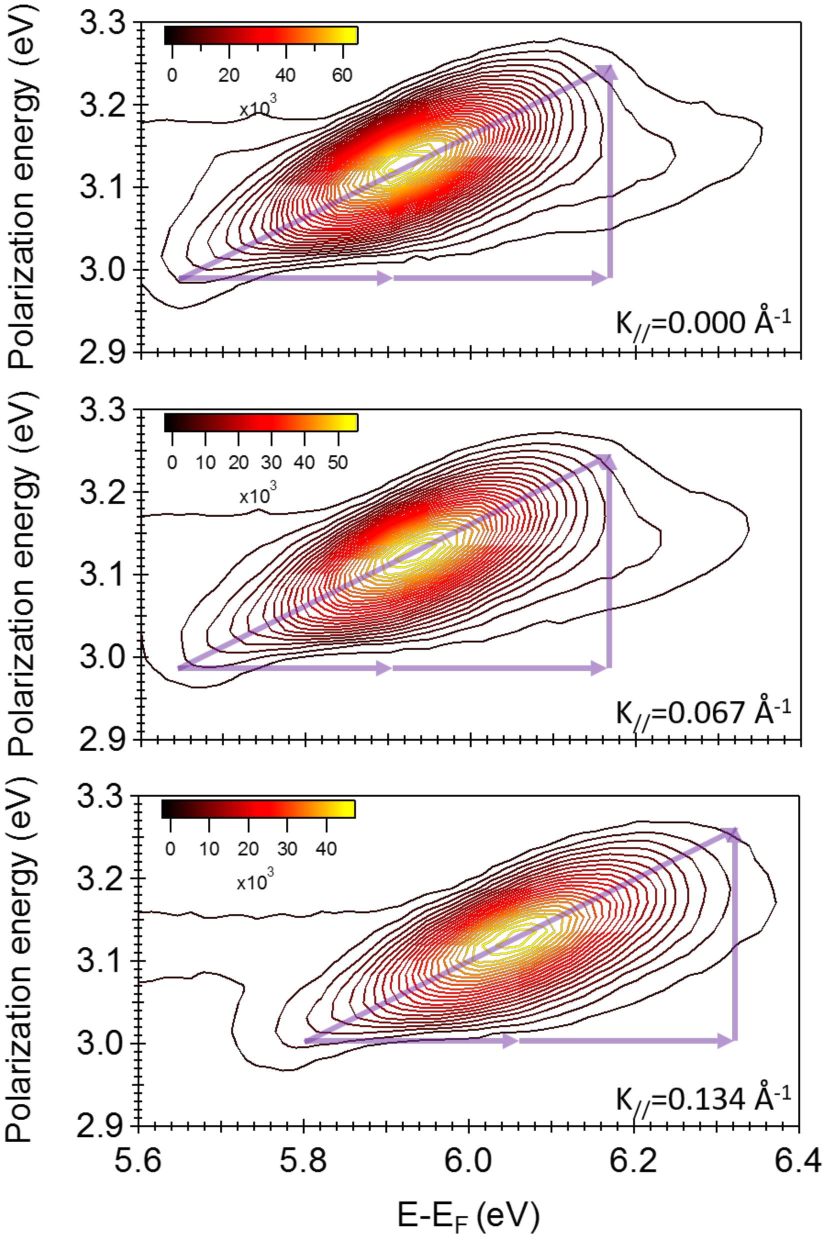

Figure 5-5 Contour plots of the linear polarization field vs the final energy from Fourier Transform of 3DCPES of Cu(111) excited by 400 nm pulse laser

We performed a Fourier Transform on the data of Figure 5-4 as well as data at larger $k_{||}$, and display the linear part of the polarization field; contour plot images are shown in Figure 5-5. The arrows marked on the figure shows that this is a coherent two-photon process. The peaks of the contour plots shift to higher final energy for higher $k_{||}$ due to the positive dispersion of SS at Cu(111). The peak features extend over energy and polarization axes. The width along the final energy axis is related to the width of the laser pulse spectrum, while the width along the polarization axis gives information on the polarization lifetime, i.e., the dephasing time, which is encoded by Fourier Transform: the narrower a specific final energy point is along the polarization field, the longer the corresponding lifetime is. Thus, we get the similar information: the lower final energy electrons are excited by polarization frequency of longer lifetime.

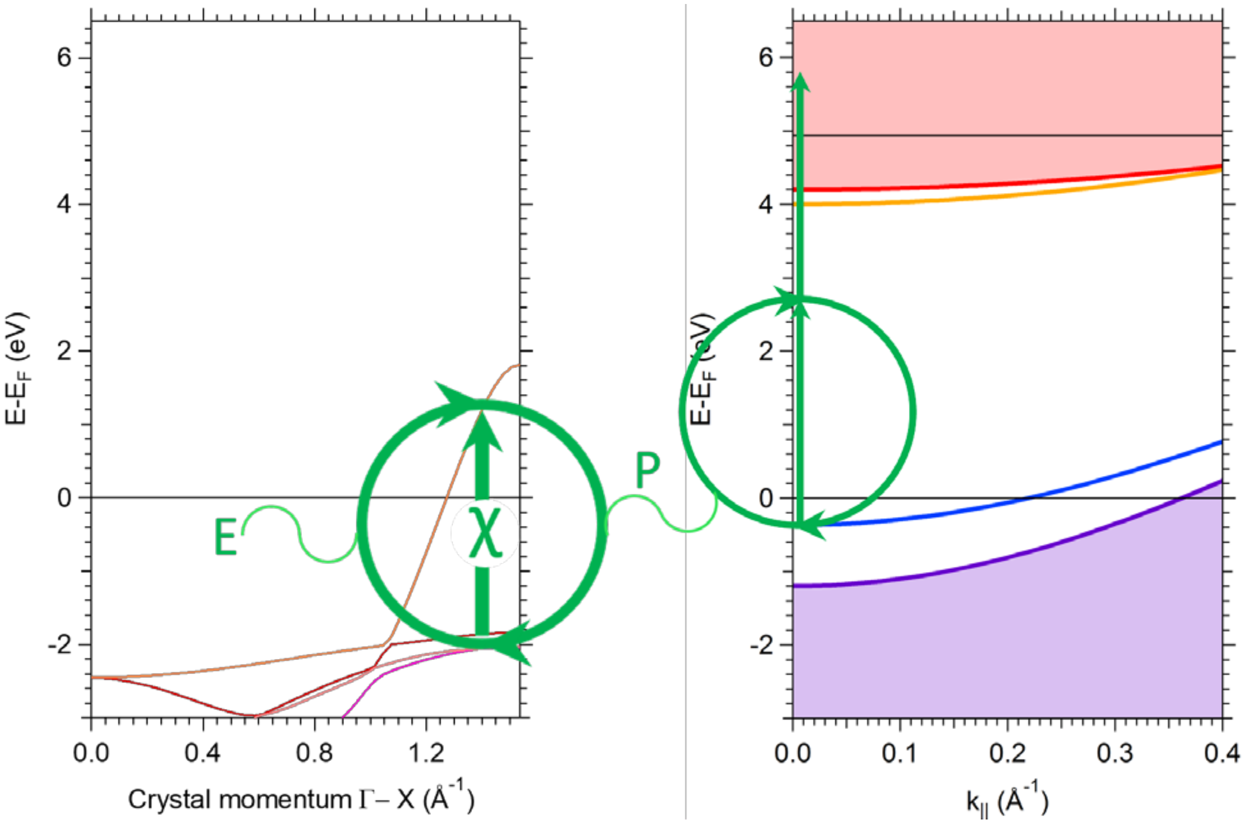

Figure 5-6 d-sp polarization

That the lower final energy electrons are excited by polarization frequency of shorter lifetime can be interpreted from Figure 5-6. The left figure shows the energy bands along the Γ to X crystal momentum direction, and the right figure shows the surface energy structure (including SS and IP shown as blue and yellow curves) of Cu(111) plotted with respect to parallel momentum. With violet pulse laser (393nm and 400nm), we are exciting electrons out of SS by coherent two-photon process. In this process, there is sp-band gap at Cu(111) and no intermediate states exist around 1 photon energy above the SS state. We would expect an extremely short lifetime of coherent polarization around the one-photon energy because the excitation is detuned from the real IP by ~1 eV. In Figure 5-4 and Figure 5-5, however, we can see there is a linear coherent polarization field that is longer than the pulse duration. The long-lived linear coherent polarization field at one photon energy is created by transitions from d-bands to sp-band, as indicated on the left image of Figure 5-6. This local polarization field can act on the SS electrons just like the external field to drive the nonlinear photoemission process. The absorption of photons from the external field to generate the local field, and then from the local field to drive the non-linear photoemission from SS of Cu(111) can be considered as a nonlinear Auger process whereby the coherent recombination of electron-hole pairs between sp-band and d-bands excites electrons from the SS of Cu(111). Also, the polarization associated with the d-bands to lower-sp band transition has a longer decoherence lifetime than the non-resonant excitation from the SS, and the lower frequency components of this polarization are expected to have longer dephasing time.

5.1.2 Cu(111) excited by visible light

In section 5.1.1, we discussed the polarization field associated d-bands to sp-band by a UV light pulse, and we argued that lower frequency components of this polarization field have a longer dephasing time, because the coupled states were closer to the Fermi level. It is therefore interesting to observe what happens when we scan the excitation at even smaller photon energies through the d-to-sp-band transition threshold[5].

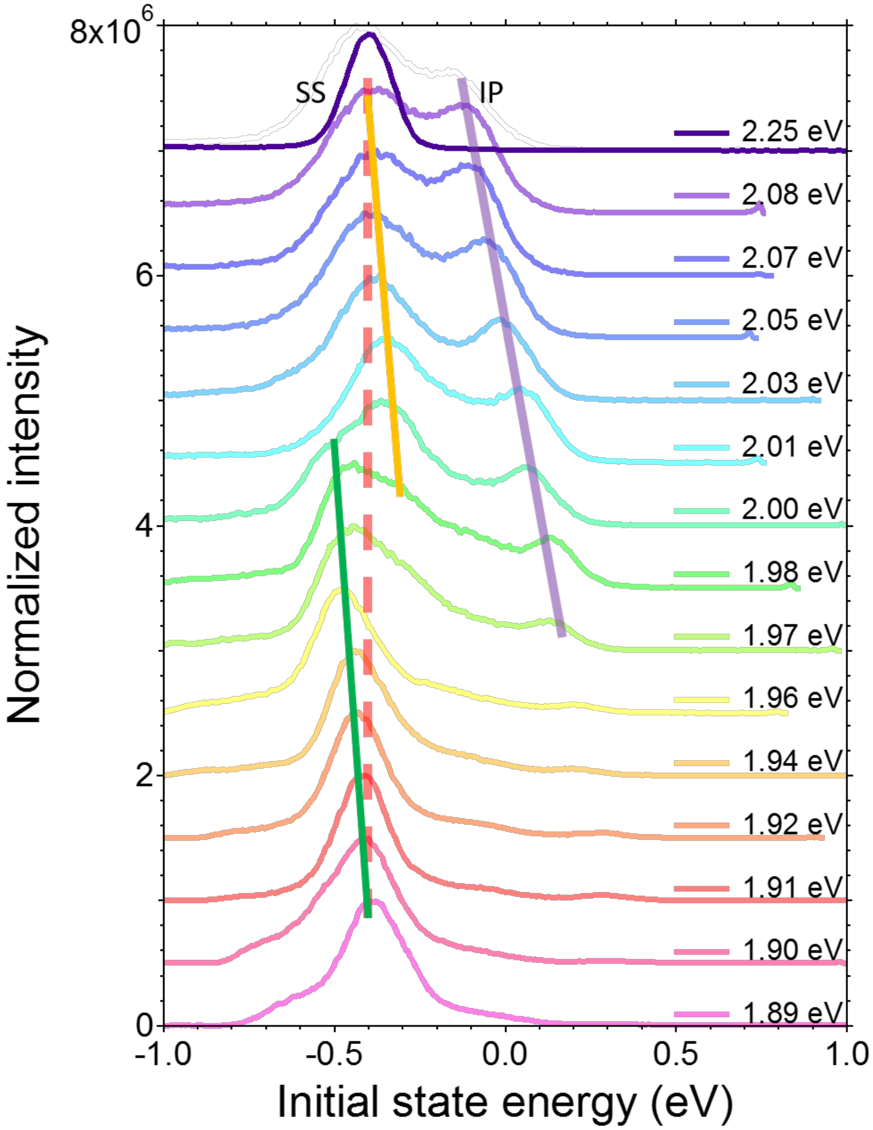

Figure 5-7 3PPE spectra of Cu(111) for normal direction. The energy scale is given with respect to the initial state by substracting the 3 photon energy from the final energy.

We performed a series of measurements by exciting Cu(111) with our tunable NOPA laser. Figure 5-7 shows the photoemission spectra for normal direction, plotted against the initial state energy by subtracting the 3-photon energy from the final state energy. The excitation tuning range from 1.89 to 2.25 eV crosses the 2 eV threshold for transitions near the top of the d-bands to the sp-band at the Fermi level crossing. According to conventional one-photon photoemission spectra, the SS on Cu(111) surface has a binding energy of -0.40 eV below Fermi Level. For the high and low photon energies in the reported range in Figure 5-7, the SS peak is at the expected initial energy and has approximately Gaussian shape. However, as the photon energy approaches the 2 eV d-sp interband excitation threshold from either side, the apparent initial state energy of SS deviates from the expected energy (dashed line) in a manner of an avoided crossing, as shown by the solid yellow and green lines. Moreover, the spectral line shapes become complex. We expect the SS energy and spectral function to be independent of the photon energy. The unexpected complex appearance of the SS in the 3PP spectra is related to the interference between 3PP processes induced by the external optical and local interband d-sp polarization fields.

In addition, Figure 5-7 includes a contribution of 3PP or 4PP via the IP intermediate state, which is indicated by the purple line. IP relative intensity with respect to SS is increasing as the photon energy increases towards the two-photon resonance from SS at 2.25 eV. When the SS and IP are in near the two-photon resonance, one might anticipate the spectra to be dominated by a transient exciton interaction, as discussed in Chapter 4.1. This is not the case for Cu(111) surface due to more efficient screening of Coulomb the interaction[74].

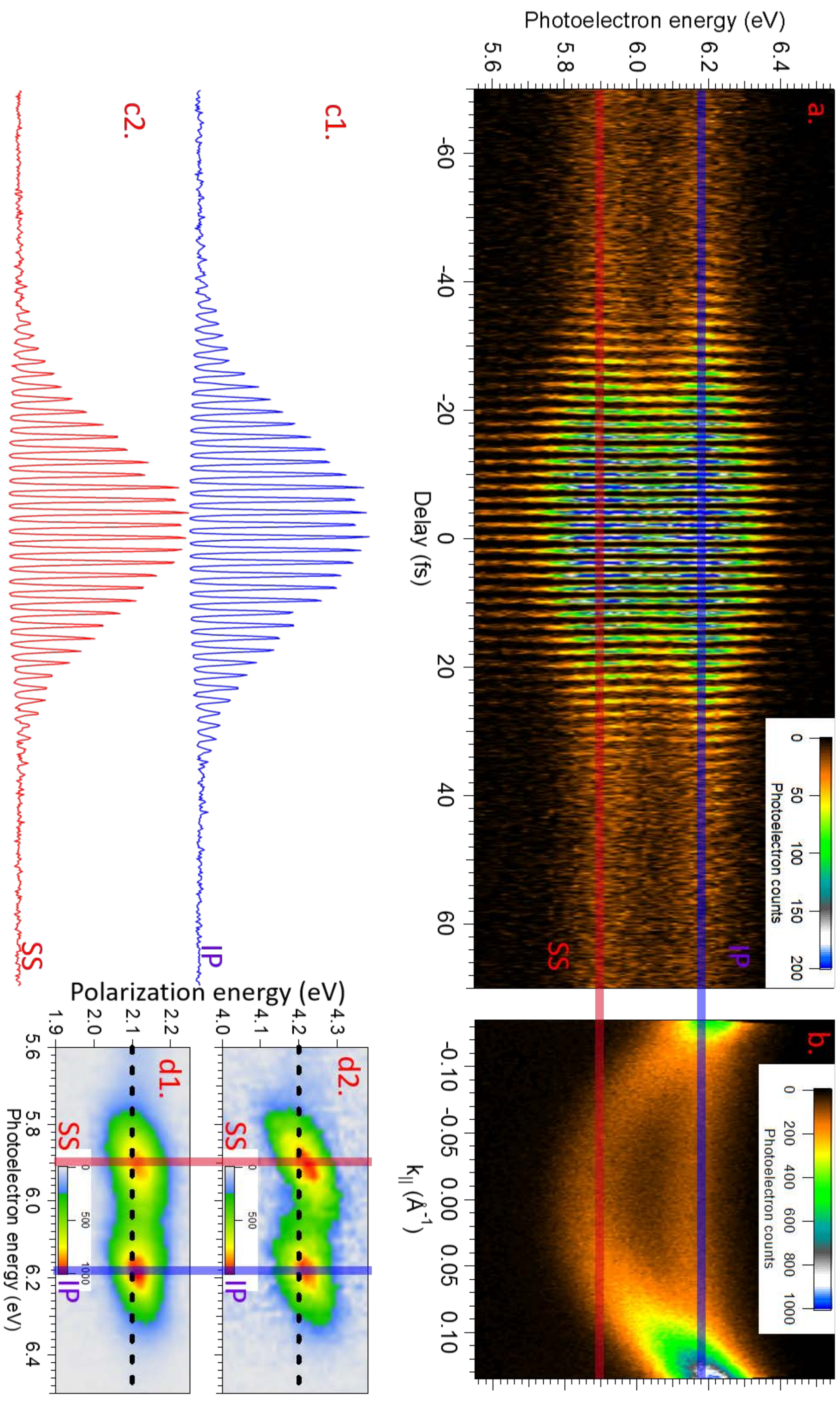

Figure 5-8 Interferometric time-resolved measurement of Cu(111) by 590nm (2.10 eV) laser

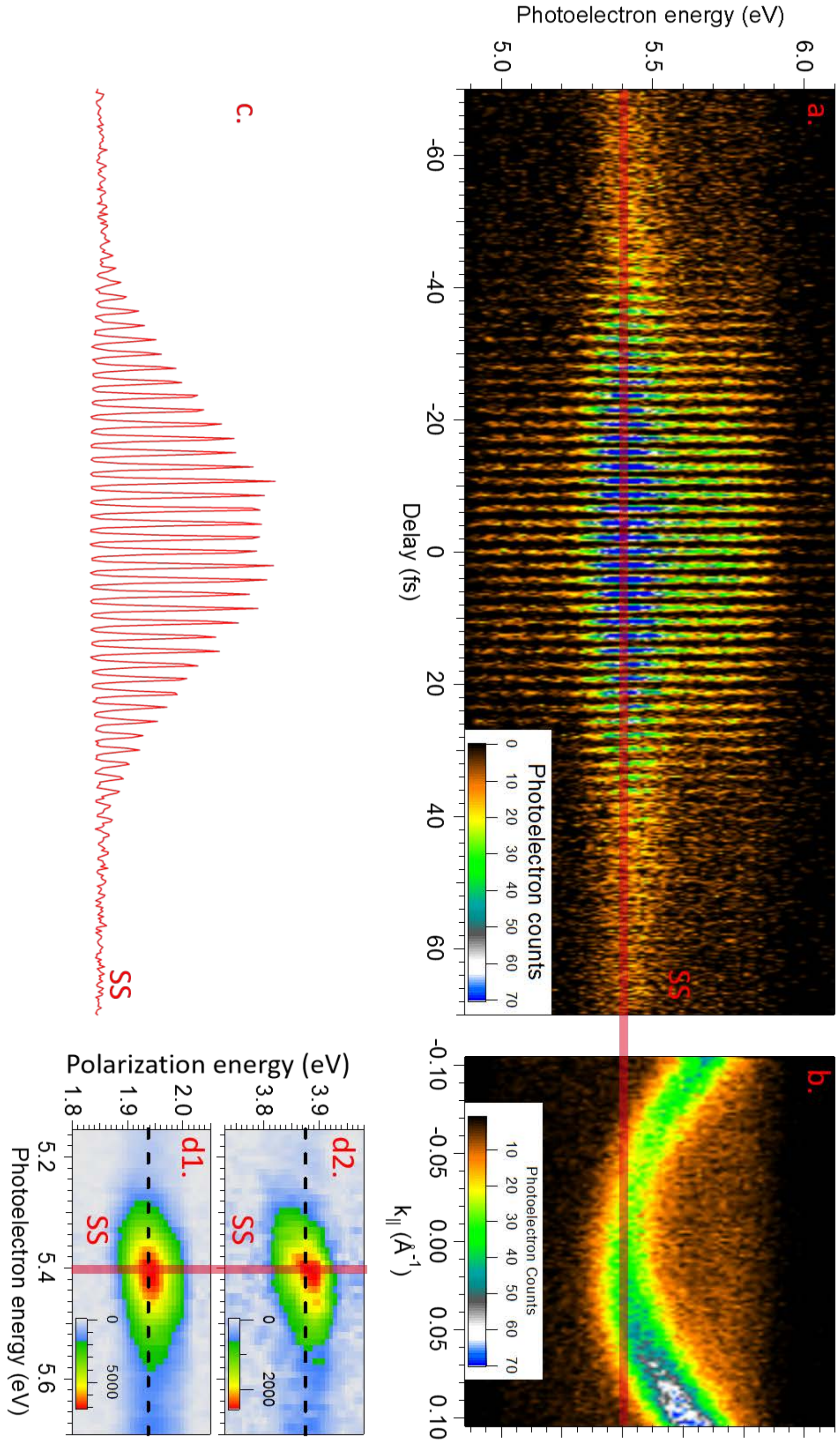

Figure 5-9 Interferometric time-resolved measurement of Cu(111) by 640nm (1.94 eV) laser

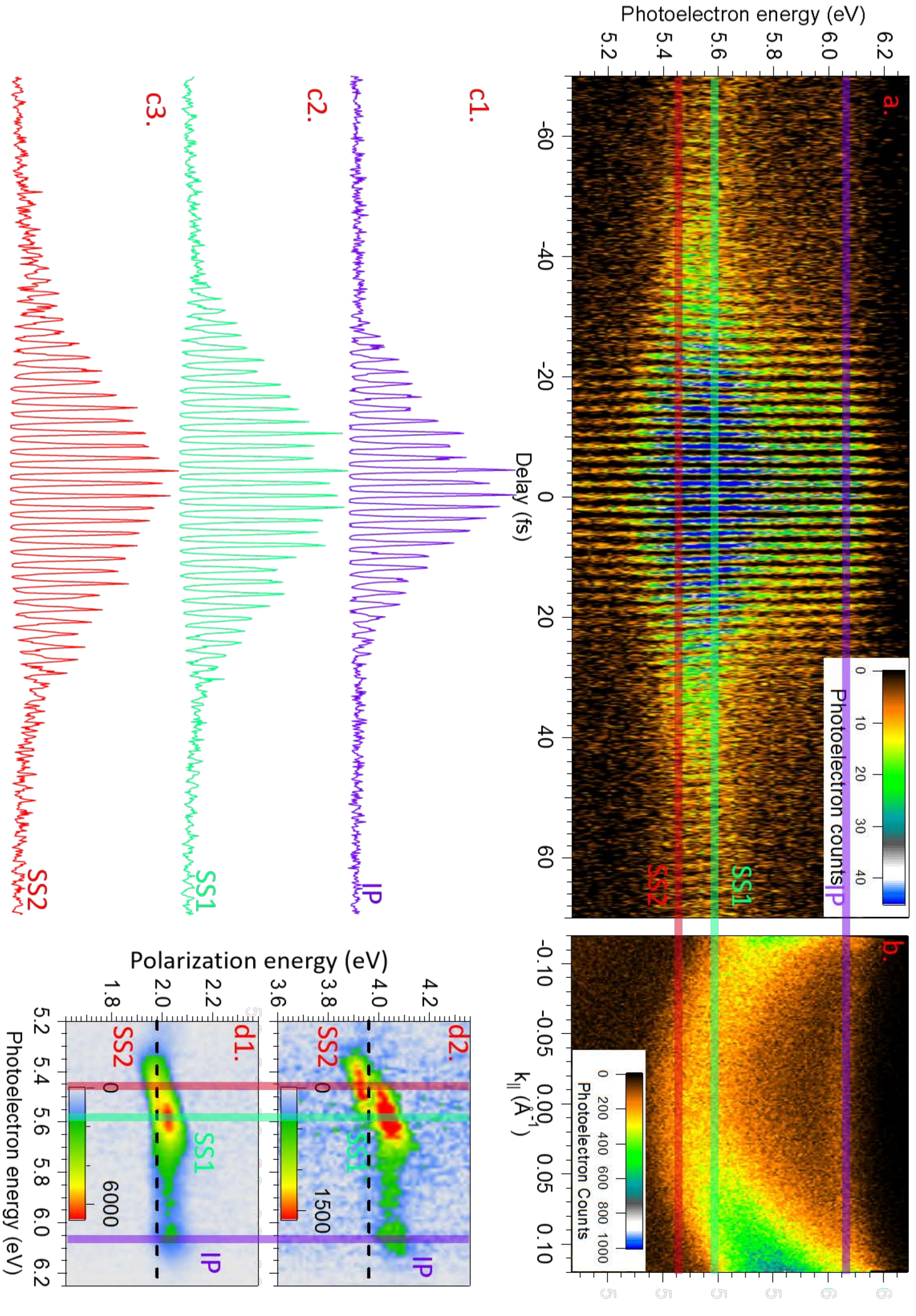

Figure 5-10 Interferometric time-resolved measurement of Cu(111) by 627nm (1.98 eV) laser

To get further information on the coherent polarization dynamics, we measure the 3DCPES of Cu(111) with the photon energy tuned through the d-sp excitation threshold. The results are shown in Figure 5-8, Figure 5-9, Figure 5-10.

Figure 5-8a, Figure 5-9a, Figure 5-10a show the interferometric two-pulse correlation measurements and their corresponding 2D electronic spectra of Cu(111) for excitation with 2.10, 1.94, 1.98 eV light. The excitation wavelengths are chosen to be above, below, and near resonance with the transition threshold from the top of the d-bands to the sp-band at the crossing with the Fermi level. In each of the Figures the b) panels show energy-momentum resolved spectra excited equivalently by a single pulse or by two pulses with 0 fs delay. The c) panels show cross sections through the data in a) for energies indicated by the solid vertical lines of the corresponding color. The panels d1) and d2) are Fourier Transforms of the data in a) for the linear and second order nonlinear coherent polarizations.

Comparing the three images, IP peak intensity increases when the photon energy gets closer to the two-photon resonance. SS peak displays a symmetric shape when photon energy is remote from the 2.0 eV d-sp transition threshold (See Figure 5-8 and Figure 5-9). However, when the photon energy is close to the transition threshold, SS becomes broad and deviates from a Gaussian-shape (see Figure 5-7). Moreover, the Fourier Transform images in Figure 5-10d show that the polarization fields that are responsible for the SS having a complex structure. The SS breaks up into 2 peaks in the 2D spectra in Figure 5-10d2, with one component above and the other below the driving frequency. The higher energy component also drives the IP state photoemission.

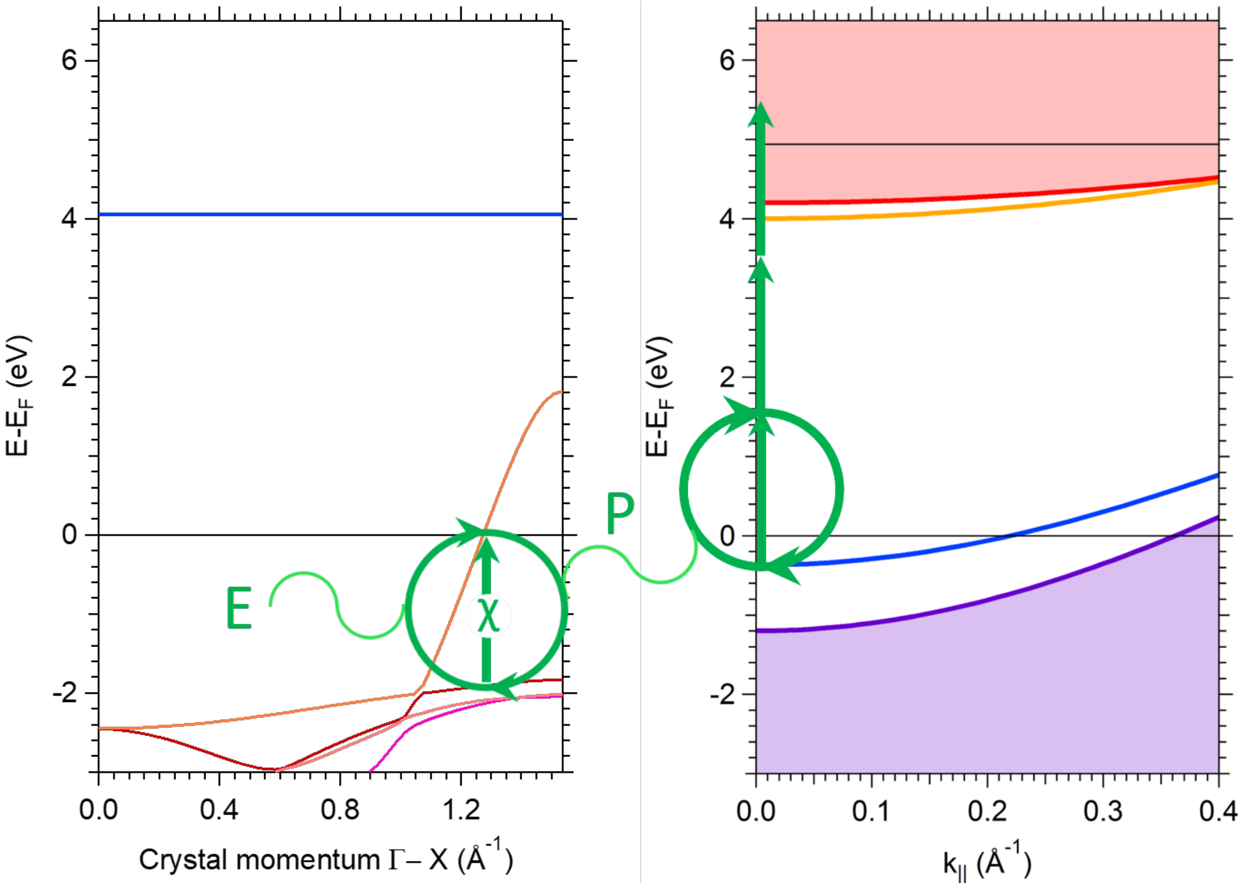

Figure 5-11 The excitation of 3PP by the local polarization field associated with the d-sp transition threshold

We interpret the anomalous 3PP spectra and coherent polarization dynamics shown in Figure 5-7 as photoemission of SS excited by both external laser field and internal induced polarization associated with the d-sp band polarization, as described in Figure 5-11. The most significant processes when copper is excited with 2 eV light and at higher energies are transitions from the d-bands to the sp-band. Due to a limited scattering phase space, the coherences associated with these excitations have rather long lifetimes[5]. It is also possible that there is excitonic enhancement of these transitions as originally predicated by Mueller and Phillips[70] in 1967. Thus, as the excitation proceeds, the polarization associated with d-sp band transition threshold builds up on the time scale of its dephasing or the laser pulse duration, whichever is shorter. This generates an intense local field, which is retarded with respect to the incident filed, and can act on the SS electrons in the mPP process, just like to external field. Thus, the 3PP spectrum is contains contributions from both the external field, and the retarded local filed it created in the sample.

5.1.3 Laser intensity dependent spectra of surface states of Cu(111)

Energy band structures of a material are dependent on its chemical composition, and geometrical arrangement of the atoms within the crystal structure[24]. A Shockley surface state[28] is created by terminating the infinite crystal lattice, and the Image Potential state[91] is created by the screening response to an electron excited from metal. These surface state electrons are located at the surface, and thus are sensitive electro-magnetic perturbation at the surface. Berland[92] et al. have shown computationally that Shockley surface state of Cu(111) can be modified by an external DC electric field. According to calculations, the energetic position and effective mass change with a linear dependence over a broad range of field strengths when a DC electric field is applied normal to the Cu(111) surface. My experiments show that both the energies and effective masses of SS and IP states can be modified by an applied optical field of a laser excitation pulse.

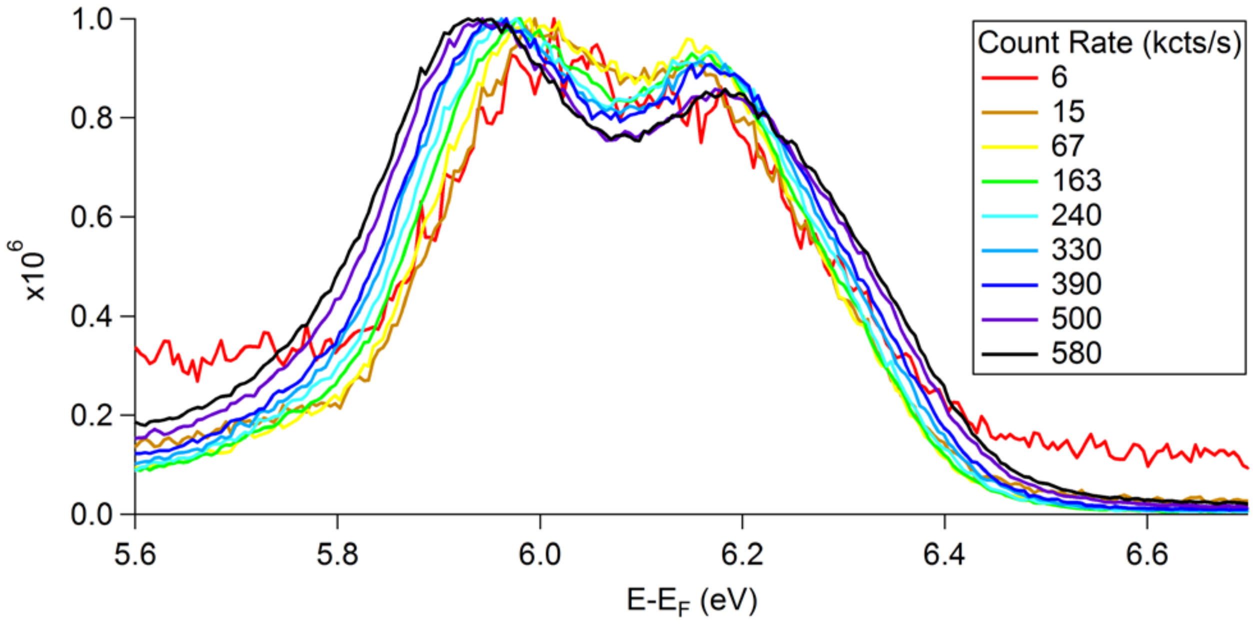

Figure 5-12 SS and IP lineshapes of Cu(111) for normal emission as a function of laser intensity

Figure 5-12 displays normal emission 3PP spectra of the SS and IP states of Cu(111), which appear at ~5.9 and ~6.2 eV with 580 nm (2.14 eV) excitation. The 3PP spectra are measured as a function of laser fluence, which causes repulsion between the nearly resonant states. To understand how we vary the laser intensity, refer to Figure 2-6 of the photoemission instrument. The focusing of the laser light onto the surface is accomplished with a CaF_2 lens, which also acts as a barrier between the laboratory and UHV environment. The lens position is variable along the optical axis enabling the tuning of the laser focus on the sample surface. Assuming pulses of 20 fs duration, with 60 mW average power focused to 100 μm diameter circular area, the instantaneous peak electric field of the laser is estimated about 0.06 V/Å. We can vary the AC electric field by changing the lens focus while monitoring the total counts per second (count rate, CR) integrated over the whole spectrum image, where the SS and IP make the dominant contributions. Figure 5-12 shows the comparison of the final energy peak positions and the spectral lineshapes of 3PPE spectra of SS and IP for different fluences, which are represented in terms of the Counts Rate. It is evident that as the CR increases, the SS and IP states are repelled and lineshapes broaden. Even though the CR for 500K and 580K are not very different, it is easy to visually discern the shifts and broadenings in the spectra of Figure 5-12. The trend of state repulsion and broadening is reproducible and occurs in 3PP spectra with other excitation wavelengths with similar magnitudes.

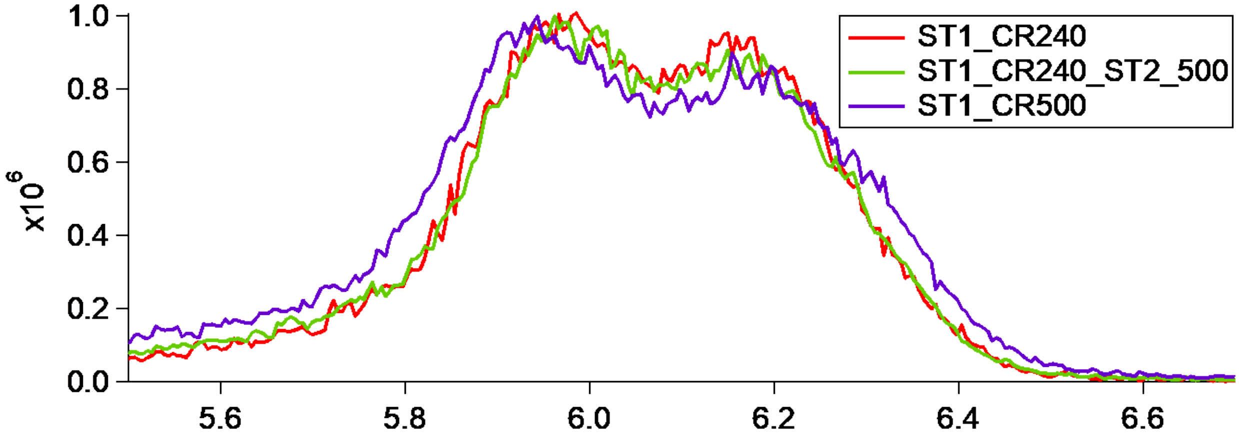

Figure 5-13 SS and IP of Cu(111) modification is not related to space charge

To understand the origin of the shifts and broadenings, we performed some test measurements. One count rate dependent artifact could be the space charge effect, which could become important when a large number of electrons are emitted per pulse. Figure 2-7 shows the diagram of the hemispherical electron energy analyzer. There is a set of slits mounted between the electron collection lens and the hemispherical analyzer, which is marked by a blue square. The role of the slits is to limit the size of the electron source before they enter the electron energy analyzer. A smaller slit limits the number of electrons that enter the analyzer and increases the spectral resolution.

In this test, a measurement is first performed with the finest slit, Slit 1 (ST1; red curve marked as ST1_CR240), which transmits 240,000 counts/second rate on the whole ARPES image. Then without changing the focus, the slits are switched to Slit 2 (ST2; green curve marked with ST1_CR240_ST2_500), which is twice as wide and allows 500,000 counts/second rate on the whole ARPES image. Next, the slits are switched back to Slit 1, and the counts rate is increased back to 500,000 counts/second rate by adjusting the focus (violet curve marked with ST1_CR500). Comparing the of red and green lineshapes, the SS and IP peak energies and are not changed, even though the count rate, and therefore the density of electrons entering the analyzer is doubled by using the larger slits (red and green curves). However, when the focus is changing while the count rate is kept constant there is a distinct change in the SS and IP peak positons and linewidths (green and violet curves).

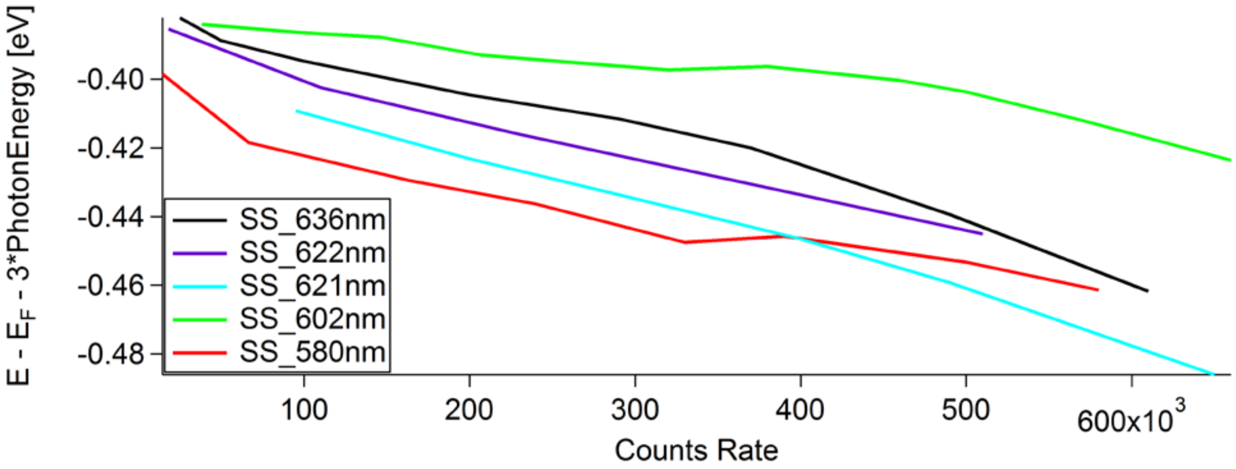

Figure 5-14 SS shifts left to lower energy under higher laser intensity excited by different wavelength

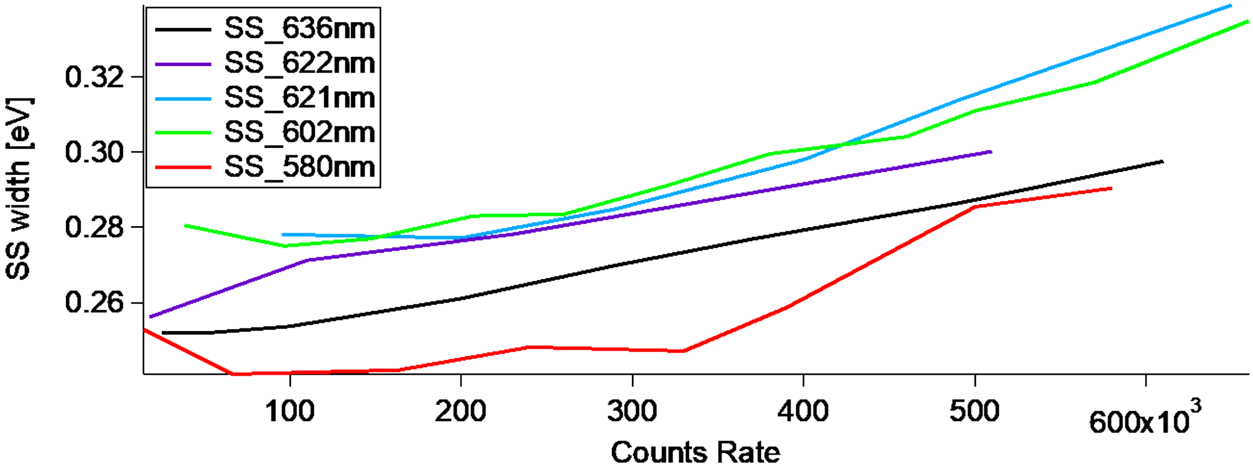

Figure 5-15 SS broadens under higher laser intensity excited by different wavelength

The modification of SS under stronger laser intensity is not unique under the excitation of 580 nm laser. Figure 5-14 shows that SS shifts to lower energy under stronger intensity excited by different wavelengths. Figure 5-18 shows that SS broadens when laser intensity goes stronger and it is observed for different wavelength. The modification of IP is hard to observe because in larger wavelength, IP peaks become weaker, and it is difficult to determine the exact positions and shapes of IP peak to make comparison.

An intuitive explanation is that SS and IP electrons expel each other. Both of these states are on the surface of copper and outside of the bulk. So there will nothing between them to affecting the Coulomb expelling. SS is closer to the bulk and the IP is outside of SS. See Figure 3-4. The expulsion between them makes SS closer to the bulk and IP farther outside of bulk. So the SS has lower energy, and IP increases energy. A better model and simulation is still needed.

5.1.4 Spectra islands from high angle of 3PPE on Cu(111)

According to Figure 2-7, in mPP measurements light excites the sample at an angle of 45° from the surface normal. Because the momentum of light is essentially zero, and photoemitted electrons emerge from a sample in a circular cone with its apex at the point where light interacts with the sample; the central axis of this cone is aligned with the central axis of the lens of the hemispherical electron energy analyzer. In the wide-angle operation mode, our analyzer has an acceptance angle of ±15°.

This angular acceptance limits the $k_{||}$ range we can observe. Specifically, it is too narrow to observe the point where SS crosses the Fermi Level. To expand the $k_{||}$ range, we can rotate the sample so that the sample is not normal to the analyzer axis. The sample is rotated so that the sample normal direction still in the optical plane.

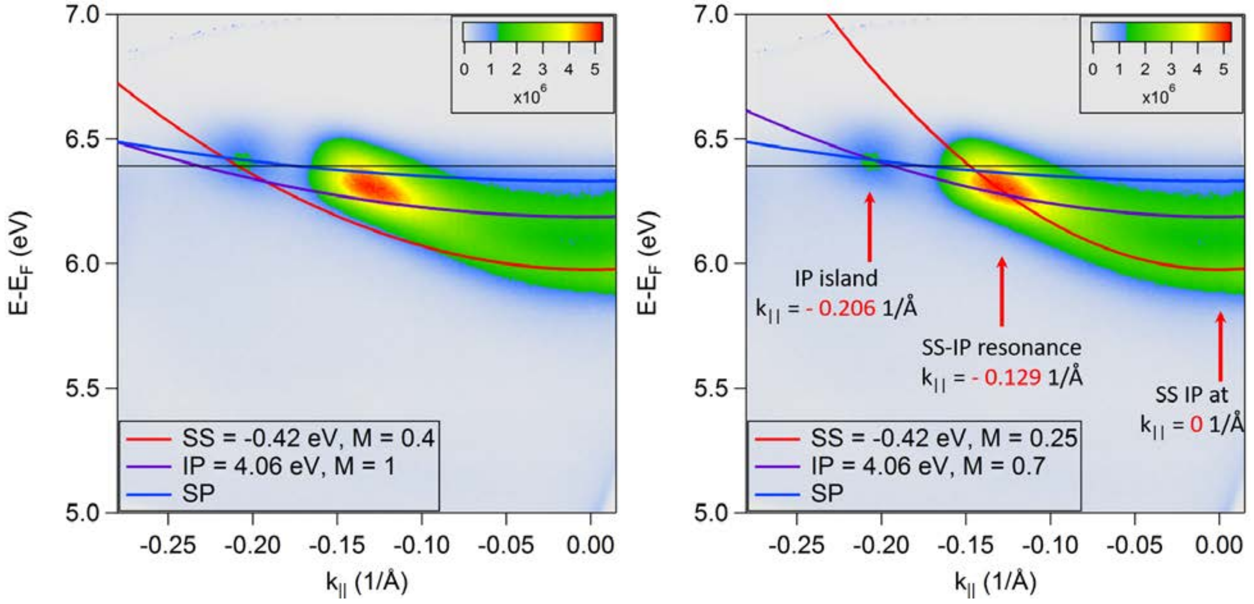

Figure 5-16 Island spectra at high $k_{||}$ momenta for Cu(111) surface excited by 582 nm (2.13 eV) light

The 3PP spectra of rotated Cu(111) sample excited by 582 nm (2.13 eV) light is shown in Figure 5-16; the left panel shows a fit of the SS and IP states using the literature values[27,31,93] for their band minima and effective masses, and the right panel shows the same data with the best fit parameters. The best fit parameters deviate from the literature values because of the fluence dependence that is reported in Section 5.1.3. The spectra now show a wider range of $k_{||}$ momenta, to access the region where SS crosses the Fermi level. The two images show the same data, and it is interesting that show an island spectrum at about $k_{||}$ = -0.206 1/Å, which is separated from the main SS and IP dispersive bands. SS and IP are marked by the red and violet lines, and the band minimum and effective masses (M) that reproduce the spectra are given in the figure. The upper sp-band is also marked with the blue curve[32]. The black horizontal line gives the position of three-photon energy above the Fermi level. As discussed in Section 5.1.3, the surface states SS and IP are modified at the higher fluence, and therefore the fitting with the literature values for them is not successful. Fitting of the SS and IP band dispersions gives a better result with modified band minima and effective masses, which represent the renormalization at high laser fluence. The enhancement in the spectra at $k_{||}$ = - 0.129 1/Å is due to SS to IP two-photon resonance, which is predicted to occur at $k_{||}$ = - 0.19 1/Å based on the literature band dispersions.

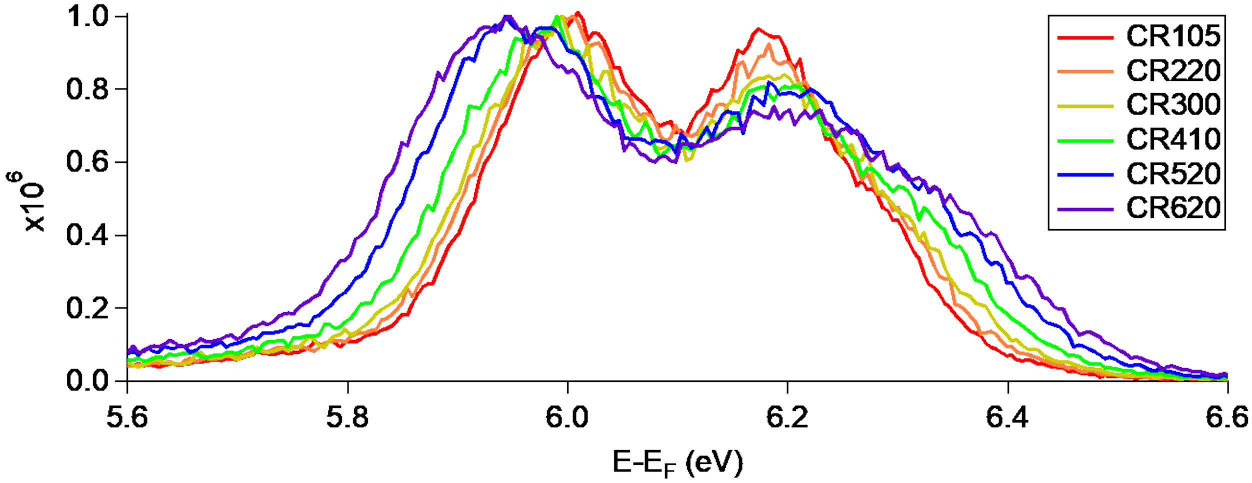

Figure 5-17 SS and IP at $k_{||}$=0 modified by laser intensity

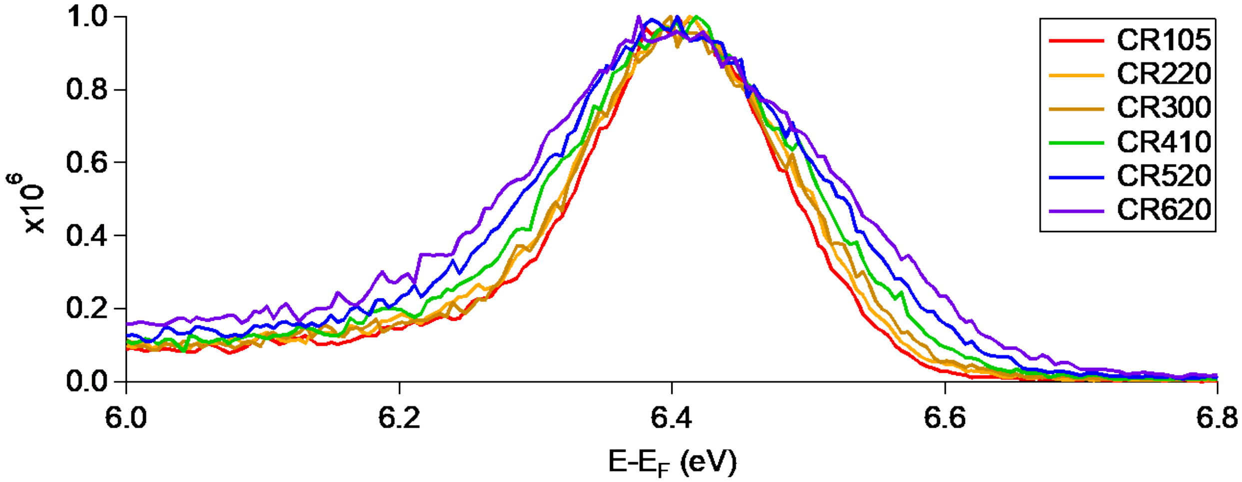

Figure 5-18 Energy position of IP island modified by laser intensity

Figure 5-17 and Figure 5-18 show how laser intensity modifies the photoemission spectra at high $k_{||}$. Figure 5-17 again demonstrates that at higher laser intensity, SS and IP at $k_{||}$ = 0 are repelling each other, and also the lineshapes are broadened, as discussed in the last section. Figure 5-18 shows that, the IP island moves little under higher intensity, but its broadening is very clear.

Even though the IP island energy is constant, as shown in Figure 5-18, it is interesting to know whether it moves along the momentum axis. To check on this point, I sum the angle-resolved 3PP spectra along the energy axis, and plot the result with respect to the $k_{||}$. Then the energy axis reduced spectra are compared for different laser intensities, as shown Figure 5-19. The upper sp-band, (shown as blue curve in Figure 5-16) has a small dispersion, so that a small change of the island along the momentum axis causes an even smaller change in the energy axis, which is too small to discern.

I have observed such IP island spectra over several years, and could reproduce the result with laser wavelengths from 536 to 580 nm (2.31 to 2.14 eV); therefore it is a robust aspect of the 3PP process at these wavelengths. Interferometric measurements confirm that the island spectra are excited by a 3PPE process.

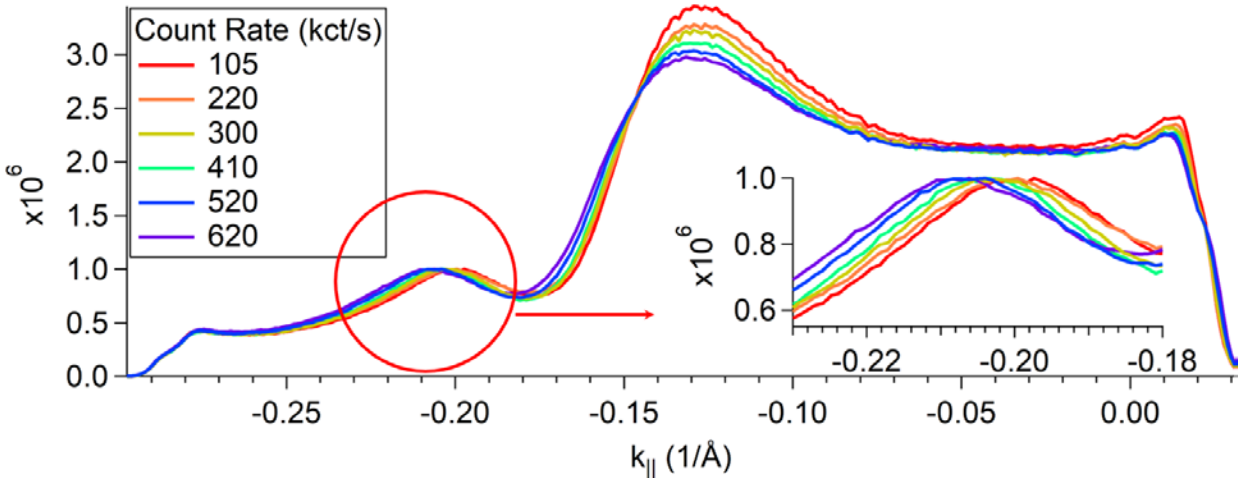

Figure 5-19 Momentum position of IP island modified by laser intensity

Figure 5-19 shows the whole momentum range of Figure 5-16, and the inset shows the shift of the IP island to larger $k_{||}$ as the laser fluence is increased.

Based on the data in Figures 5-16 and 5-19, we can construct the following scenario for the island feature considering the modification of the SS and IP state dispersions with the fluence. As the excitation with the femtosecond laser pulse proceeds, the surface states evolve dynamically. At low fluence, there is a two-photon resonance from the SS crossing of the Fermi level to the IP crossing with the upper sp-band, as can be seen in the left panel of Figure 5-16, which can create coherent polarization and excite population in the excited states. As the laser fluence rises during the excitation pulse, the SS and IP state band dispersions are renormalized so that the pulse-averaged situation is represented by the right panel of Figure 5-16; the SS to IP resonance shifts to lower energies and momenta with respect to the low fluence case. The upper sp-band, being a bulk state, is most likely unperturbed or only weakly perturbed at high fluence. Therefore, the dynamical change of the surface bands turns off the resonant excitation from the SS crossing with the Fermi level only after some population has been transferred to the upper sp-band. Thus, the IP island actually represents the bulk upper sp-band population that was excited at low fluence, and became stranded as the laser field renormalized the surface bands. This stranded population is detected by absorption another photon into the photoemission continuum during the excitation process.

5.2 THE IMAGE POTENTIAL STATE OF THE Cu(100) SURFACE

In the last section, we have seen the intense laser field in an mPP experiment can modify the well-known band dispersions and other features of the SS and IP states. In this section, I will explore how the line shapes of IP state on Cu(100) is affected by underlying bulk electronic structure of copper.

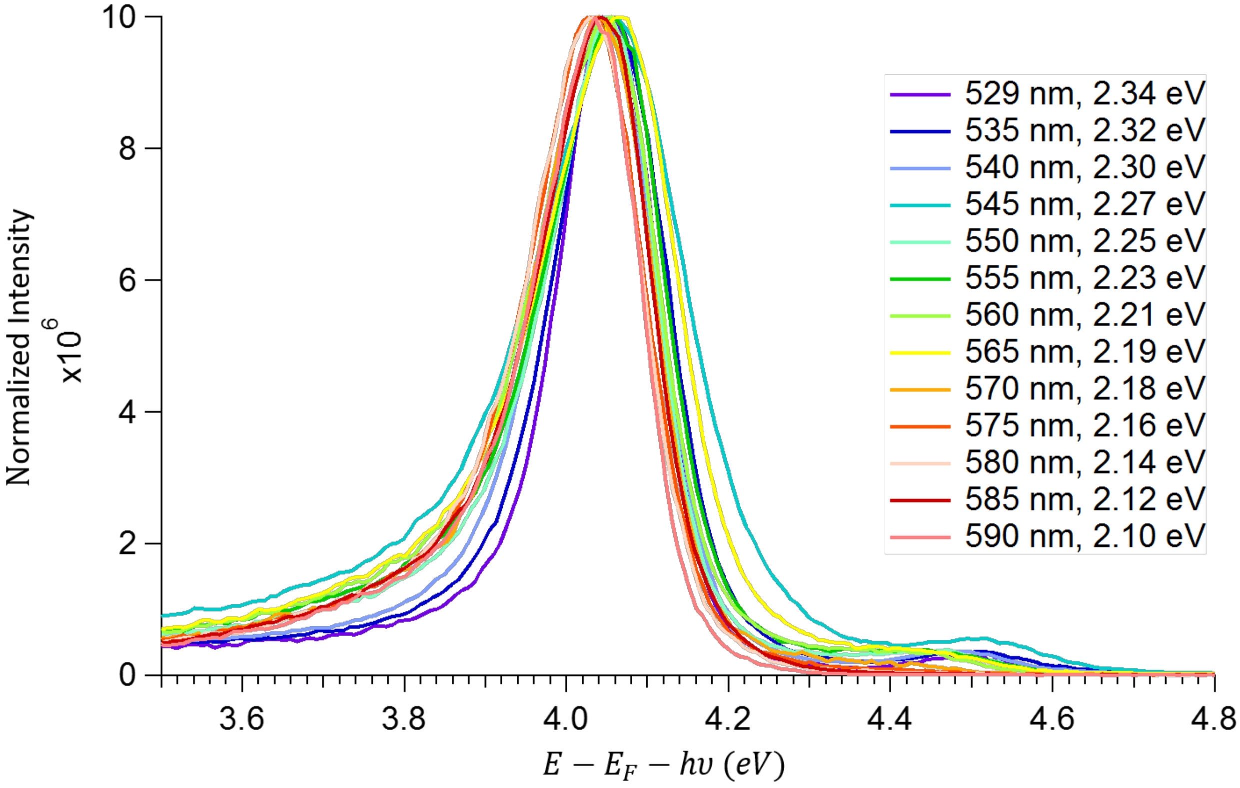

Figure 5-20 Line shapes of the IP state in 3PP spectra when tuning the photon energy above the two photon resonance from the Fermi level to the IP state

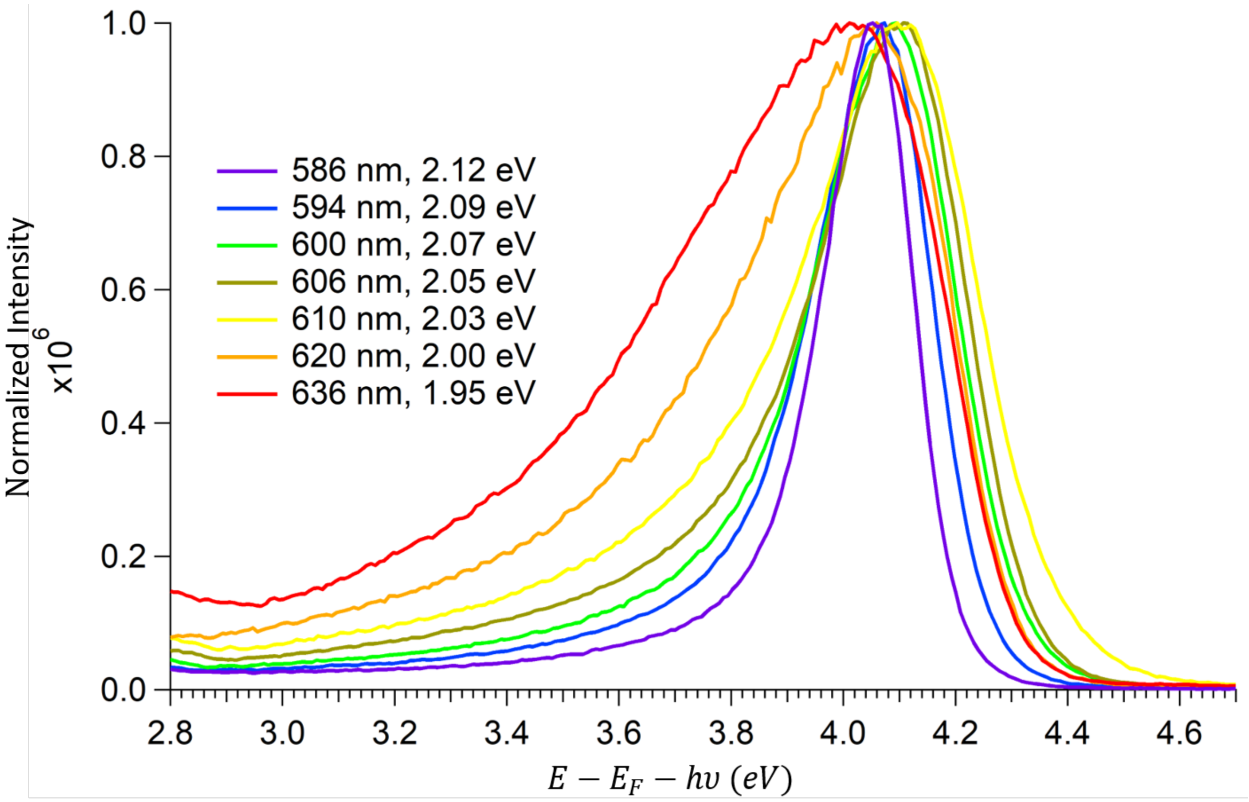

Figure 5-21 Line shapes of the IP state in 3PP spectra when tuning the photon energy across and below the two photon resonance from the Fermi level to the IP state

Figures 5-20 and 5-21 show the changing lineshapes of the *n*=1 IP state on Cu(100) surface as the excitation wavelength is from 2.10 to 2.34 eV and 1.95 to 2.12 eV. The line shapes are plotted with respect to the intermediate state energy state, $E_i = E_f - h\upsilon$, which is obtained by subtracting one photon energy from the final photoemission energy E_f. Because the IP state is the penultimate state in the 3PP process, subtracting the photon energy should cause all of the spectra to align at the same photon energy. This is not the case, and indicates that the excitation process is more complex than implied by simple electronic energy level climbing. The two-photon resonance from the Fermi level to the *n*=1 IP state is at 4.05 eV; therefore, Figure 5-20 shows the data for tuning photon energy above the two-photon resonance, while Figure 5-21 is for tuning photon energy from above to below the resonance. Both figures show that the asymmetry of the IP line shapes increases when photon energy is decreased from 2.34 to 1.95 eV and the IP state peak energy shifts below the energy that is reported in two color 2PP measurements[94,95]. These wavelength dependent features are a product of the coherent interactions that are involved in the 3PP process. A qualitative explanation for the asymmetry of the IP lineshapes can be found in Figure 5-22.

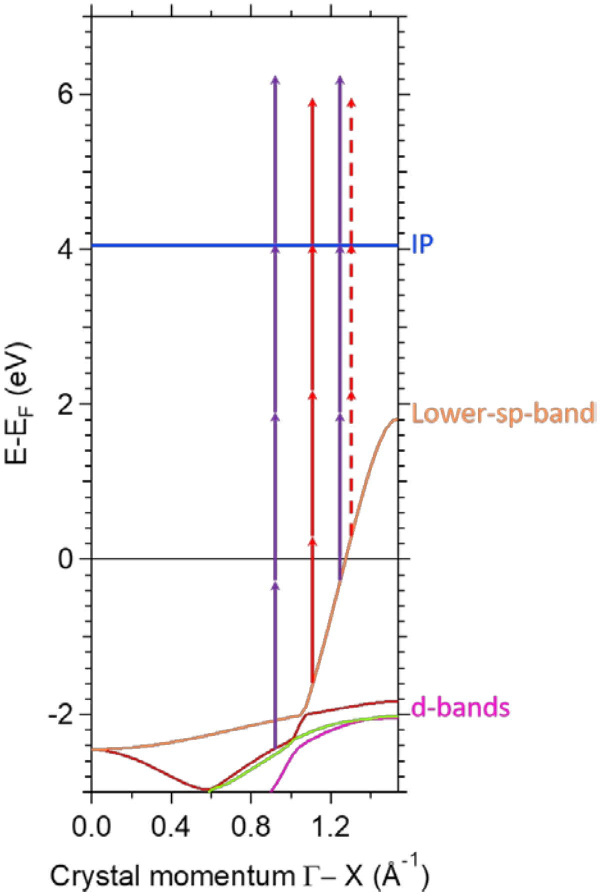

Figure 5-22 Excitation Pathways for 3PP and 4PP via the IP state of Cu(100)

Figure 5-22 shows the bulk band structure of copper along Γ-X crystal momentum direction with 3PP and 4PP excitation pathways indicated by arrows. The Γ-X direction is normal to the (100) surface. The band structure is shown for $k_{||} = 0\ \text{Å}^{-1}$ where the IP state has a minimum, which is marked by a blue horizontal line. The *n*=1 IP state is within a projected band gap that extends from 1.8-7.9 eV; being far from the band edges, it is weakly coupled to the bulk bands, and therefore has long phase and energy relaxation times[96]. Because there is no occupied surface state on Cu(100), the initial states for 3PP and 4PP excitation must be the bulk bands. As suggested by Figure 5-22, the mPP spectrum can have contributions from both the 3PP and 4PP processes. The 3PP occurs near the Fermi level where the band dispersion of the sp-band is steep and the hole spectral function rapidly broadens as the hole energy deviates from the Fermi level. The 4PP process has contributions from both the sp-band and the d-band; the d-hole lifetimes near the top of the d-bands are long compared to the sp-band and the density of states is large[5]. This favors the 4PP process to occur. For low photon energy excitation (red arrows in Figure 5-22), the initial state for 3PP is above the Fermi level, so the 4PP process with significant d-band character dominates, and pulls the excitation to lower energy. As the photon energy is increased, as shown by the violet arrows, the 3PP with dominant sp-band character dominates and restores the IP state closer to its expected energy. The IP state lineshape is asymmetric throughout because of the contributions from 4PP, which favors the low energy wing of the lineshape. The wavelength dependent IP state spectra highlight the importance of coherence in the mPP process; such effects have not been reported in two-color 2PP experiments where the photoexcitation is incoherent.

6.0 MULTIELECTRON DYNAMICS AT A Cs/Cu SURFACE

In the last chapter, I introduced several mPP experiments on the clean Cu(111) surface, especially the parallel-excitation of SS by the laser field and induced local field. In this chapter, I will introduce experiments on Cs deposited Cu(111), and interpret the data in terms of generation of a local field by a multi-electron (ME) process[97–107].

6.1 EXPERIMENTAL RESULTS

The experiments discussed in the chapter were performed by my lab mate, Ms. Shengmin Zhang.

The Cu(111) surface was prepared by cycles of sputtering and annealing until work function converges and clean SS and IP are observable. Then Cs atoms were deposited onto Cu(111) from a getter source while monitoring the angle resolved mPP spectra until σ and π resonances of alkali atoms appeared. The phenomena reported here also appear for Rb/Cu(111), but for simplicity I will just refer to the Cs/Cu(111) surface.

The band structure of Cs deposited on Cu(111) is shown in Figure 6-1c. In addition to the well-known SS and IP, σ and π resonances[108] are introduced by Cs atoms; the σ resonance is derived from the 6s atomic orbital, and the π resonance is derived from the $6p_x$ and $6p_y$ orbitals. The salient feature of the π resonance is that it is weak at Γ point, and has higher intensity at higher momentum. Angle resolved multiphoton photoemission spectrum of Cs/Cu(111) excited by 650 nm (1.91 eV) light is shown in Figure 6-1a. And Figure 6-1b shows the line profile cuts at Γ point.

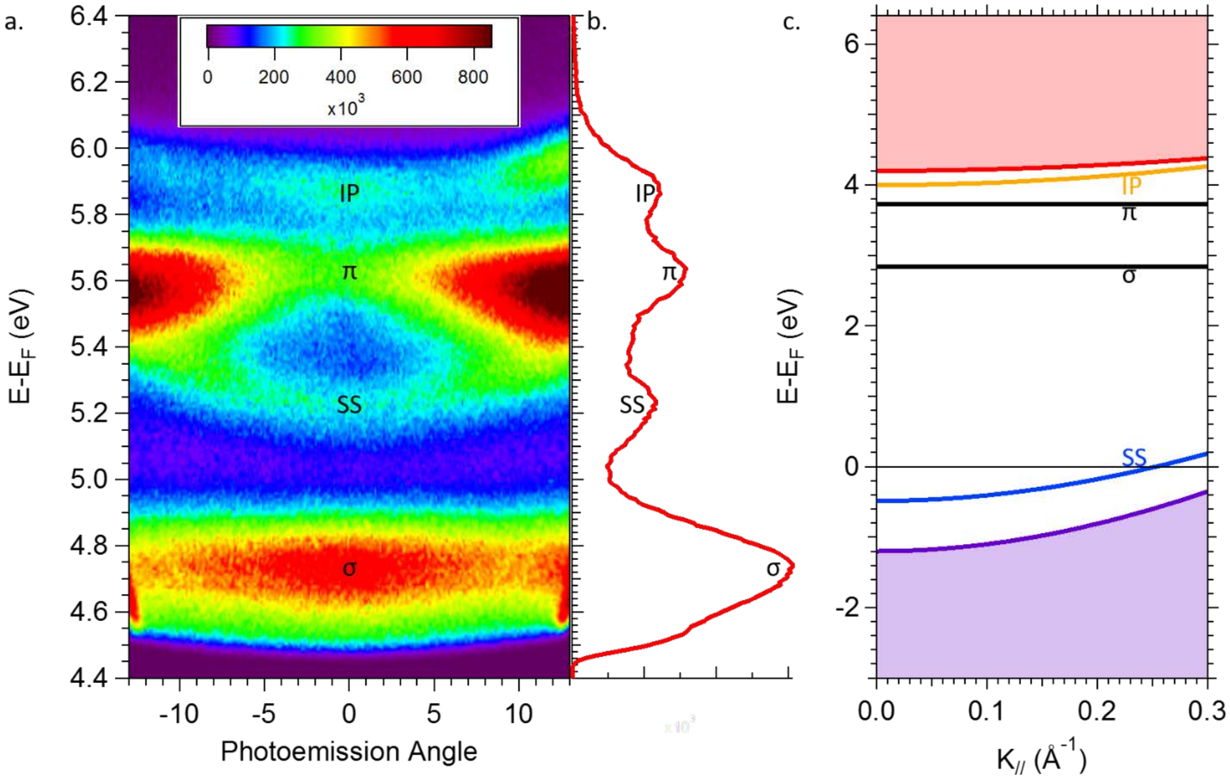

Figure 6-1 a. angle resolved photoemission spectra of Cs/Cu(111) excited by 650 nm (1.91 eV) light. b. lineprofile of the spectrum in 0 degree angle. c. The band structure of Cs deposited on Cu(111)

The experiments and the associated physical mechanism will be covered in detail in Shengmin's dissertation. In my thesis I focus only on the main experimental finding in Figure 6-2. Figure 6-2a shows the interferometric two-pulse correlation measurement of the σ resonance. Though the interferogram has an approximately bell shaped envelope of the oscillations, there is an additional beating within the envelope corresponding to enhancement of the fringes every 3 optical cycles. This is unique to the σ resonance of Cs and Rb deposited on Cu(111) for excitation with 650 nm (1.91 eV) light pulses. Other spectral features in Figure 6-1a do not show the behavior, and it happens in a narrow range of excitation photon energies. The interferometric two-pulse correlation is analyzed by Fourier Transformation, and the result is presented in Figure 6-2b. Figure 6-2b shows the frequency components that are responsible for the oscillatory signal in Figure 6-2b; in addition to the main components at the fundamental and second harmonic of photon energy, there are fractional components at approximately 1/3, 2/3, and 5/3 fractions of the excitation frequency, which are outside of the laser spectrum and beyond expectation. These frequency components seemingly violate the energy-time uncertainty, because they should decay on the time scale that is governed by their detuning from the excitation frequency, which is roughly 1 fs, yet they persist throughout the excitation pulse of ~20 fs duration.

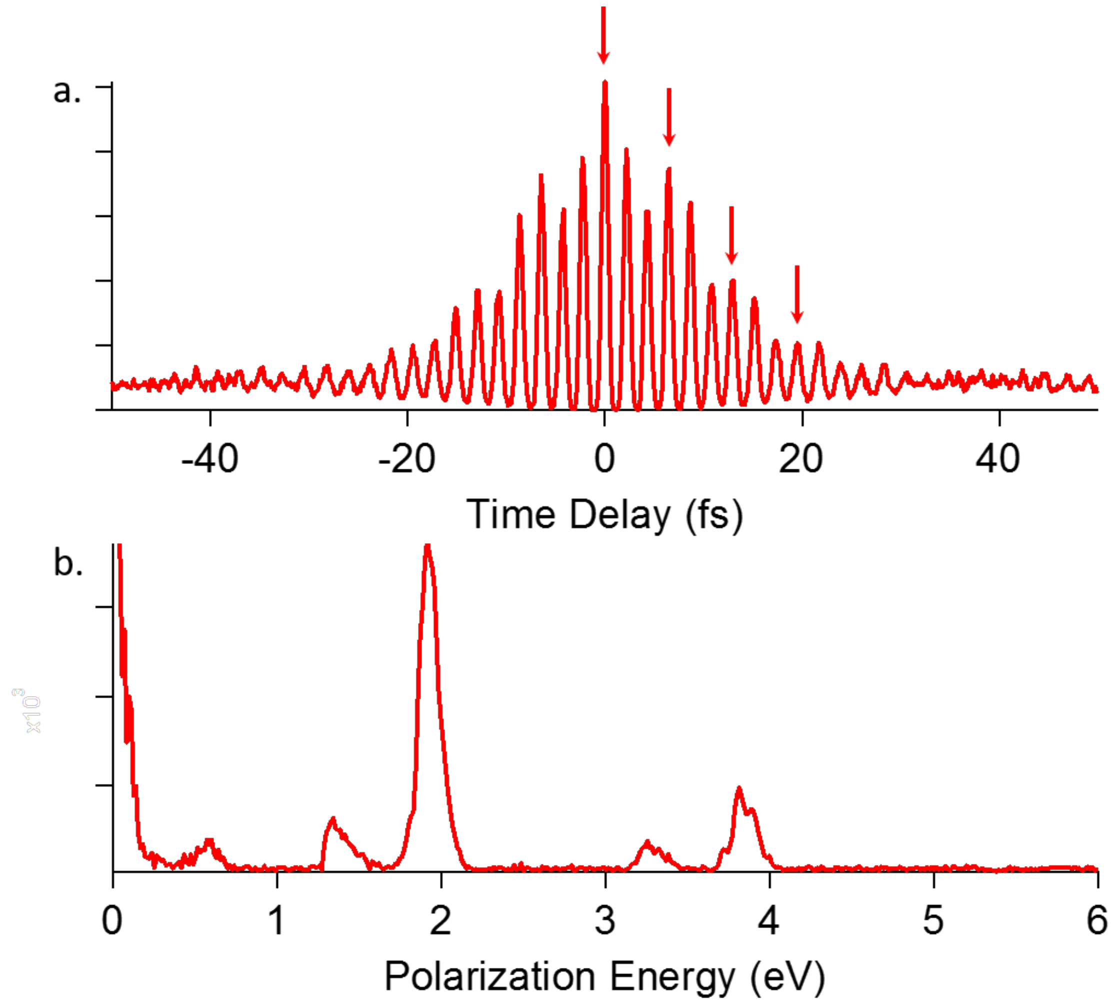

Figure 6-2 Interfermetric two pulse correlation measurement at the σ resonance of Cs/Cu(111) with excitation at 1.91 eV, and (b.) its Fourier Transform

6.2 SIMULATION RESULTS

The excitation process for the σ resonance of Cs/Cu(111) is explained in the Figure 6-3. When Cs resides on Cu(111), the outer shell of 6s state electron is transferred to the SS of Cu substrate[109], and Cs exists as a cation, whose charge is screened by SS. When the system is excited with 1.91 eV light, electrons from SS will be excited into higher energy states. The only available state within the sp-band gap of Cu(111) is the σ resonance, which is 2/3 above the one photon virtual state or 1/3 of the photon energy below the two photon virtual state. Therefore, there is not a dipole transition to the σ resonance that conserves energy. The energy conservation can happen through Coulomb interaction that is turned on when the positive Cs atoms accept an electron. The energy can be conserved by a multielectron process within the Fermi sea. Thus, the joint action of the dipole interaction and the Coulomb interaction it turns on, excites an electron from SS to the σ resonance, and the screening charge density within the 2D electron gas of the SS. Because the strength of the Coulomb interaction is ~1.5 eV[110], the multielectron generation can happen within an optical cycle, which preserves the coherence of the excitation process. My simulation of this multielectron process reproduces the major features of Figure 6-2b.

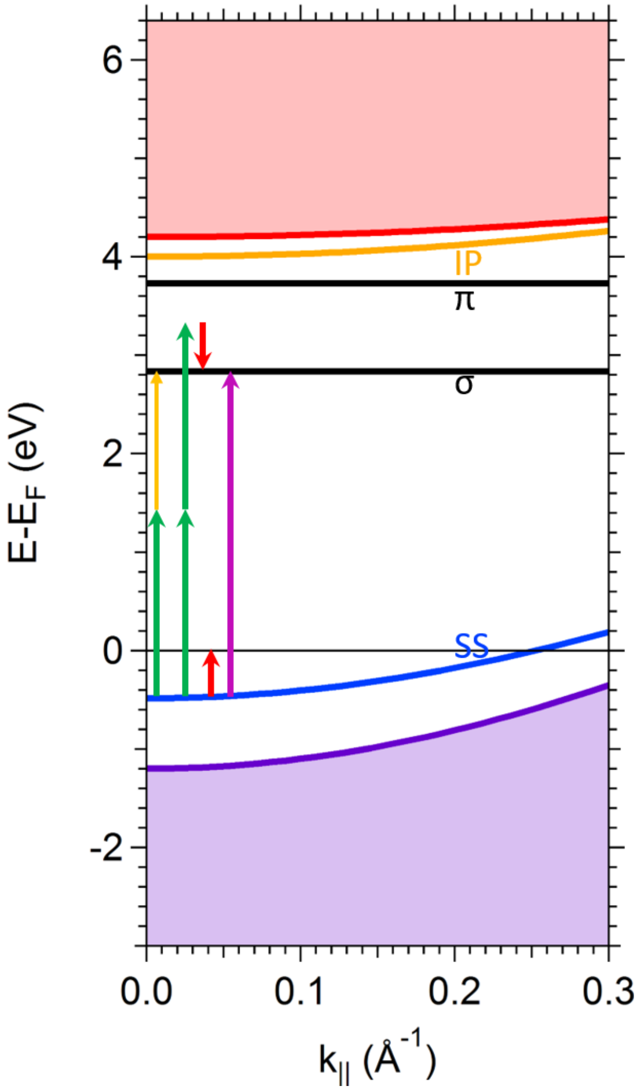

Figure 6-3 Excitation Dynamics of the σ resonance

The multielectron process is simulated by the Optical Bloch Equation approach. The laser field drives the electronic excitations and at the same time creates an induced polarization field. The laser field is of 20 fs pulse duration. The polarization field is modeled by an envelope multiplying the oscillatory term $\cos(\omega_p t + phase)$, with ω_p to be energy difference between the σ resonance and SS state. The phase is chosen to be π, so that the induced polarization field could screen the laser field. The polarization field envelope is shown Figure 6-4, together with the laser field, and the total field, which is direct sum of induced polarization field with laser field assuming that the two fields have the same maximum amplitude. The induced field is likely to be weaker, but its exact amplitude is unknown. The envelope is modeled by the instantaneous electron population in σ resonance excited by the same laser field without induced polarization field taken into consideration. The oscillatory component in the envelope shape is due to the fact that 2-photon energy exceeds the energy for excitation from the SS to the σ resonance.

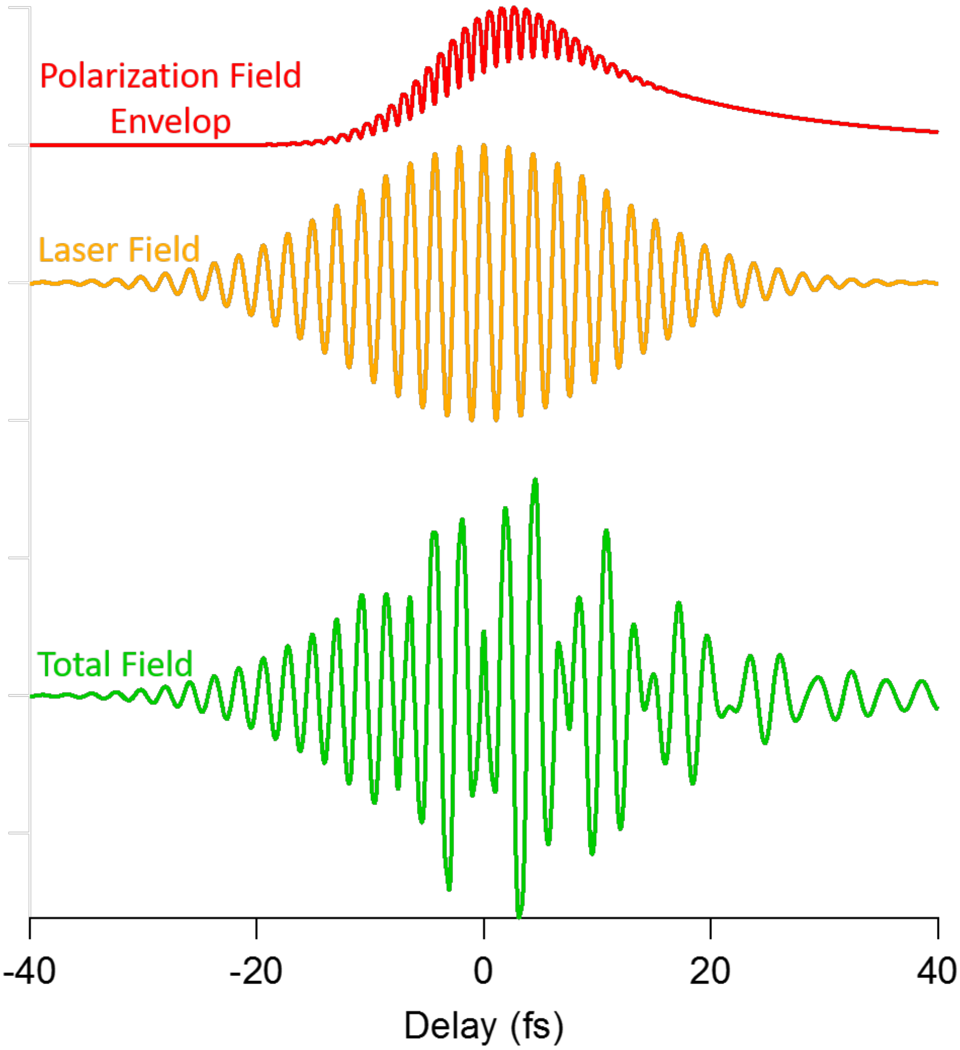

Figure 6-4 The electric fields that drive the σ resonance at 1.91 eV

Figure 6-5 shows the simulation result. We can see that the simulation reproduces the most important features of the experimental data namely the integer and fractional frequencies in the Fourier spectra of the coherent polarization. The simulation result could be improved by tuning the ratio of maximum amplitude between the laser field and the induced polarization field and by adding other fractional frequency components to the induced polarization that are excited by the multielectron process.

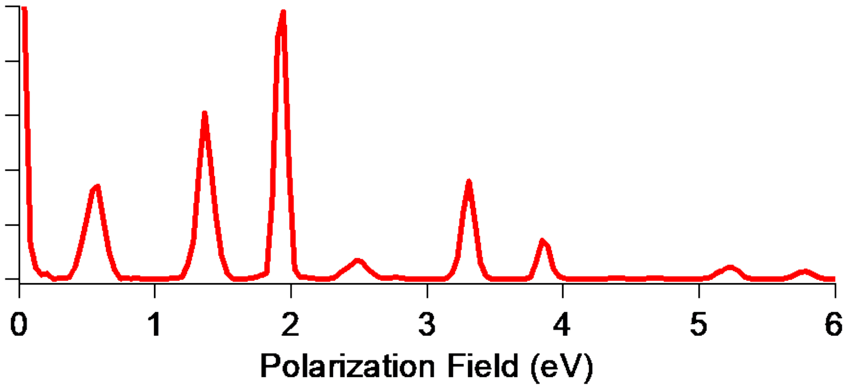

Figure 6-5 Fourier transformed coherent polarization for the simulated time-resolved 3PPE spectra for the excitation of the σ resonance with total field of induced polarization field plus photon field

The simulation again verifies the existence of a local polarization field in mPP excitation at metal surfaces. Though induced and driven by external field, the induced field has its own intrinsic energy and oscillatory frequency that is determined by the electronic energy level structure of the surface. By performing the interferometric time-resolved measurements the different coherent frequency components that lead to mPP are revealed. Optical Bloch simulation, with complex excitation paths but without using the sum of the two fields, has not yet been successful in reproducing the experimental results.

7.0 SUMMARY

The goal of this dissertation has been to study the optical response of noble metals (silver and copper), and the underlying dynamics of coherent polarization fields by means of three-dimensional coherent photoemission spectroscopy.

The principles of the three-dimensional coherent photoemission spectroscopy have been extensively discussed. Three-dimensional coherent photoemission spectroscopy combines traditional angle-resolved photoemission, ultrafast laser excitation of multiphoton photoemission, and interferometric scanning of identical pump-probe laser pulses. The angle-resolved photoemission system provides energy-momentum resolved photoemission spectra. The broadly tunable excitation of the sample from IR to UV is accomplished with a fiber laser pumped NOPA system. The third-dimension time-delay axis is created in an interferometric time-delay scanning system based on Mach-Zehnder interferometer. The time-delay axis is under computer control and is calibrated by measuring interference fringes from a reference channel.

To facilitate the understanding of 3DCPES, we here made simulations of the pump-probe measurements of the multiphoton photoemission process. We calculated the wave functions of the SS and IP applying the Fourier Grid Method and using the pseudopotential proposed by

Chulkov etc. The realistic wave functions enable calculation of dipole transition moments. They are used together with the Optical Bloch Equations to simulate the 3PP processes.

We employed a NOPA system to study wavelength dependent energy-momentum resolved photoemission spectra. Further, we studied the dynamics of the coherent polarization field by performing interferometric pump-probe two-pulse correlation measurements, and obtained three-dimensional coherent photoemission spectra that illuminate the mPP processes on Ag and Cu surfaces. Furthermore, we interpreted the physical process by analyzing the Fourier Transformed two dimensional correlation spectra between polarization field and final photoemission energy.

Our research on Ag provides direct evidence for the existence of transient excitons on a metal surface. Though much research has been done on excitons in molecular systems, semiconductors and insulators, concerning excitons in metals, there has been an on-going debate in the literature since 1967 whether or not they can exist in metals. By definition, metals do not support bound states of the Coulomb potential because dense electron liquids screen the Coulomb interactions. However, this screening takes time for the electrons to rearrange once their distribution is perturbed. And this opens the door to observe excitonic interactions as the excited metal returns to equilibrium. In our multi-photon photoemission spectra we find direct evidence for the existence of a transient excitonic response from Ag(111). When our laser is tuned to be near resonant from the SS to the IP state, in addition to the well-known and expected SS and IP spectra, we observe a new band with much higher intensity, for which the energy is independent of momentum. This is the key signature of a collective localized state of electrons such as the exciton. Also, we offer a picture of the transient dynamics when the transient excitons are born upon the light-metal interaction, the excitation triggers the Coulomb screening, the screening tears the bound exciton states apart into electrons and holes, with the excited electrons asymptotically evolving into the IP state. Furthermore, the time-resolved measurements show that the surface response is dominated by the internal field established by the SS-to-IP two-photon resonance, rather than the external laser field driving the interaction. The same signatures of transient excitons for the SS to IP excitation also appear in one-photon and three-photon resonances.

In order to get a deeper understanding of light-metal interactions, we also investigated the optical response of Cu(111) surface. Because of the faster screening of Cu, no excitonic features are observed, but other features of photoemission spectra still demonstrate the importance of the internal fields on ultrafast surface processes. As we tune laser energy across the d-to-sp-band transition threshold, the SS deviates from its energy, and its lineshape profile becomes complex. We attribute this phenomenon to parallel excitation pathways in which the multi-photon photoemission occurs in response to not only the external laser field but also the internal fields. The interaction of the excitation light with the surface, however, also excites the inter-band transition from top of the d-bands to the sp-band at its crossing with the Fermi level (the highest occupied energy level in a metal). Because the electron and hole dephasing at the origin of the interband spectrum is slow, a local polarization field can build up in the surface, retarded with respect to the incident filed, and drive the three-photon process at the energy of the d-band-to-Fermi level resonance, which is manifested in the Fourier Transformed two dimensional correlation spectra.

The d-bands effects of copper were revisited when performing measurements on Cu(100) surface. When we tuned the laser energy from 2.34 eV down to 1.95 eV, we observed the changing of IP peak position and its symmetry. This is explained by the complex excitation pathways. As the photon energy is decreased, the main feature in photoemission spectra due to the IP state transition from a 3PP process to 4PP process. The 3PP process has its initial state from L_{SP} band, whose hole lifetime decreases as hole energy departs from Fermi Level. The 4PP process involves partially the d-bands and partially the sp-band. The holes at the top of the d-bands have long lifetimes, and their state density is large. Thus, 4PP process enhances the low energy wing of the IP state lineshape.

Finally, my colleague, Ms. Shengmin Zhang, observed polarization beating in interferometric two-pulse correlation measurements for the photoinduced charge transfer excitation of the σ resonance of Cs on Cu(111) surface. The underlying physics is interpreted as a multi-electron process, which is the joint action of the optical dipole interaction and the Coulomb interaction it turns on: exciting an electron from SS to the σ resonance requires the screening charge density of SS to rearrange in response to the sudden transition from an ionic to a neutral Cs impurity atom interacting with the Fermi sea. We simulate this by using a total field composed of laser field and polarization field. The envelope of the polarization field is modeled by the instantaneous electron population in σ resonance excited by the same laser field without induced polarization field taken into consideration; the oscillation occurs at the energy difference between σ resonance and SS state. The simulation reproduces the key features of the experimental data.

These studies demonstrate the unique capability of 3DCPES for revealing the ultrafast coherent response of metals.

APPENDIX

SOFTWARE FOR 3DCPES MEASUREMENTS

We developed a software package, programed in LabVIEW, to take 3DCPES measurements. A LabVIEW program is called a virtual instrument (VI). The principle of making such a measurement is introduced in Section 2.3.

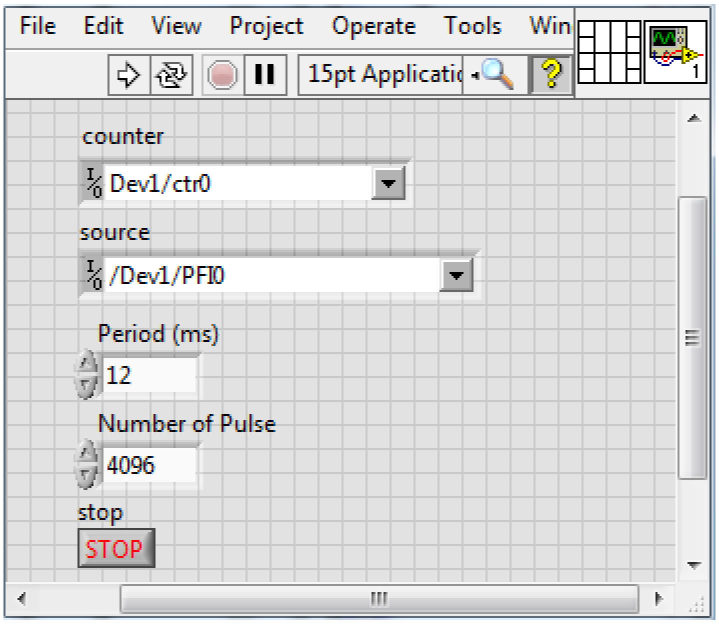

counter: Dev1/ctr0

source: /Dev1/PFI0

Period (ms): 12

Number of Pulse: 4096

stop

Appendix Figure 1 Front panel of TTL signals generation VI

Appendix Figure 1 shows the front panel of the VI used to generating a series of TTL signals, which are shown in Figure 2-9c. The signal of Figure 2-9b is fed into the source connector, and the output comes from the counter output. The period and number of TTL signals can also be configured. Its block diagram is shown in Appendix Figure 2.

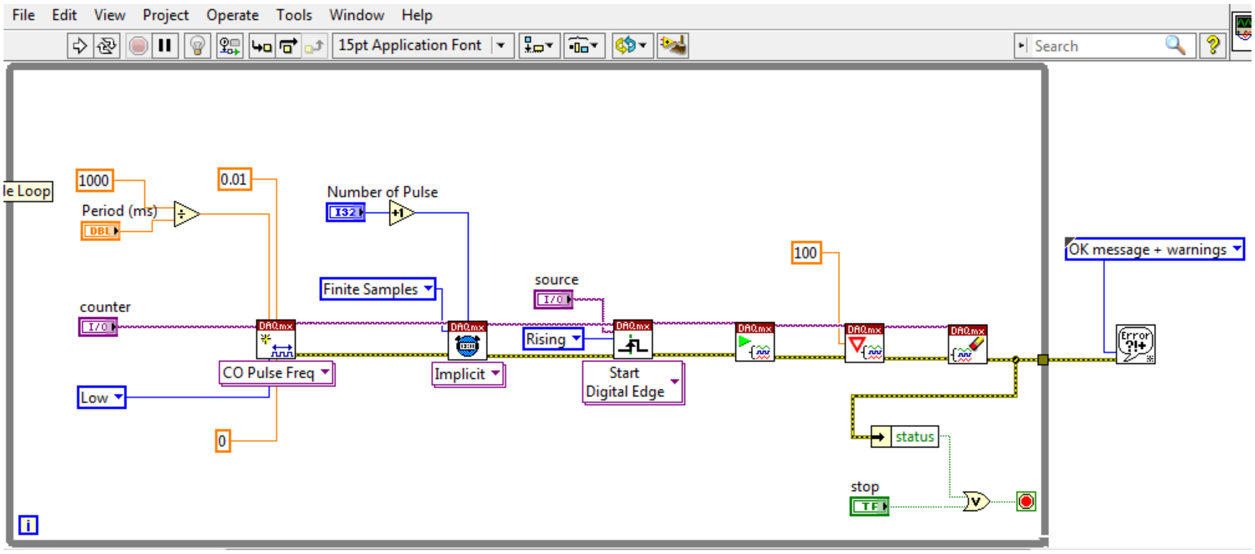

Appendix Figure 2 Block diagram of TTL signals generation VI

Appendix Figure 3 shows the Front panel of the VI collecting laser interferometric signals, which are red sine wave in Figure 2-11. The interferometric signals of pump-probe laser pulses, are fed into the Analog Input Channel connector. The Start Trigger is Figure 2-9b, and the Sample Clock connector connects to the output of Appendix Figure 1. The samples per channel and exp time are the same with Number of Pulses and Period in TTL signals generation VI. And its block diagram is shown in Appendix Figure 4.

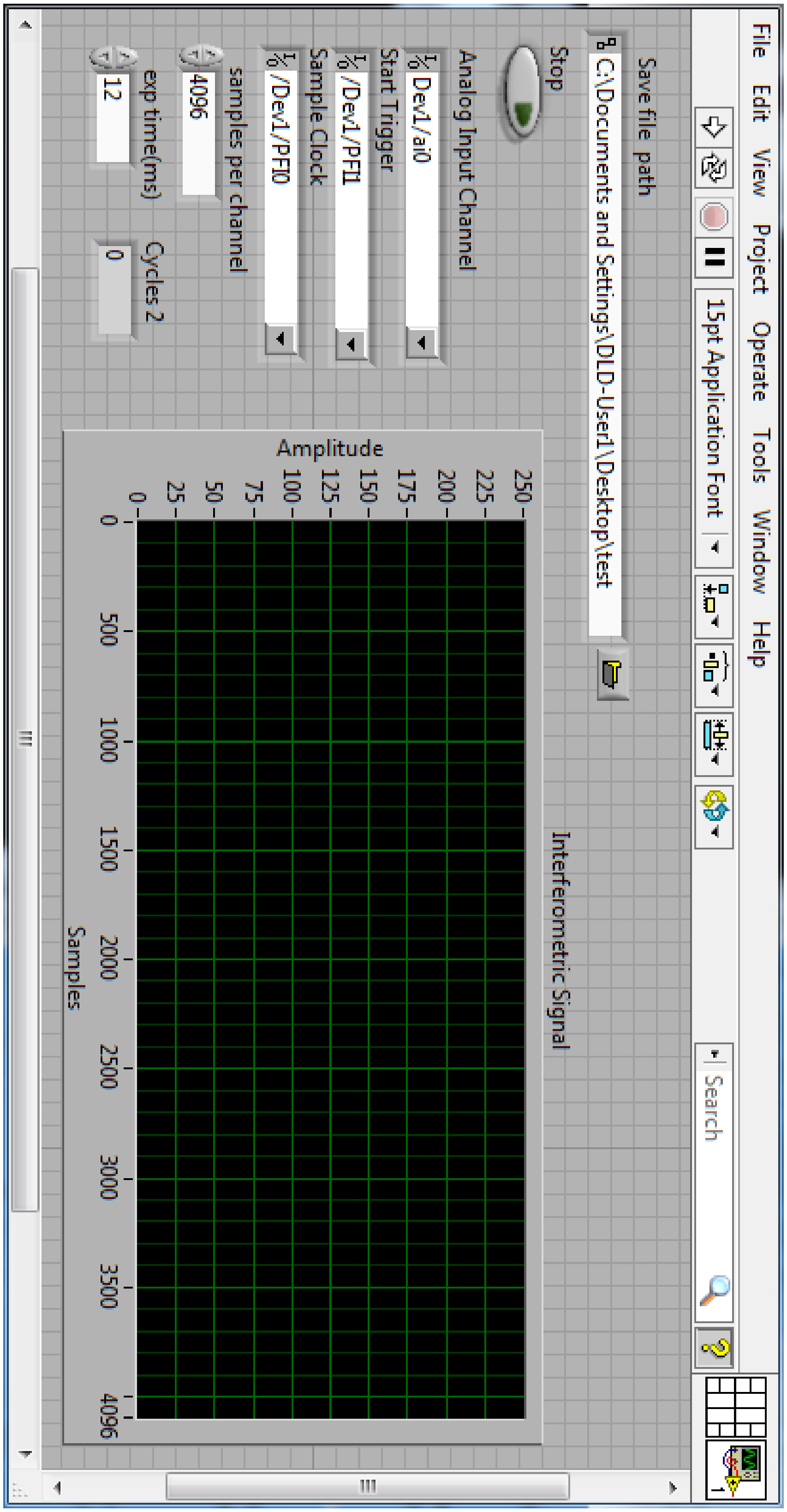

Save file path: C:\Documents and Settings\DLD-User1\Desktop\test

Analog Input Channel: Dev1/ai0

Start Trigger: /Dev1/PFI1

Sample Clock: /Dev1/PFI0

samples per channel: 4096

exp time(ms): 12

Cycles 2: 0

Appendix Figure 3 Front panel of laser interferometric signal collecting VI

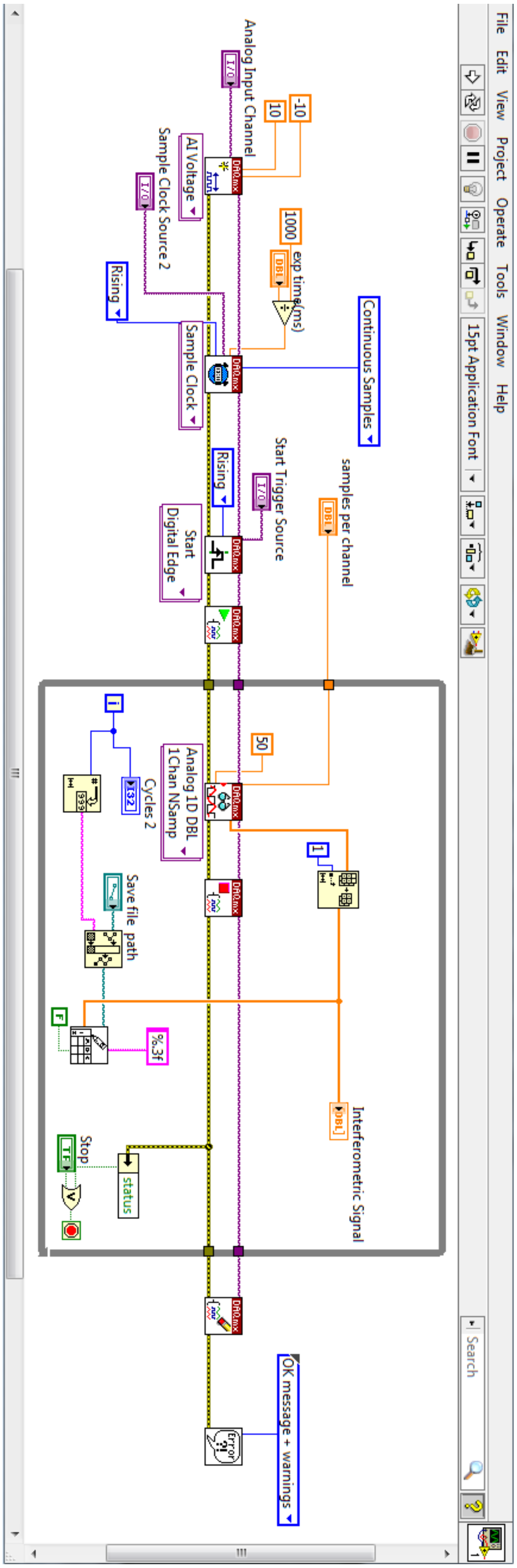

Appendix Figure 4 Block diagram of laser interferometric signal collecting VI

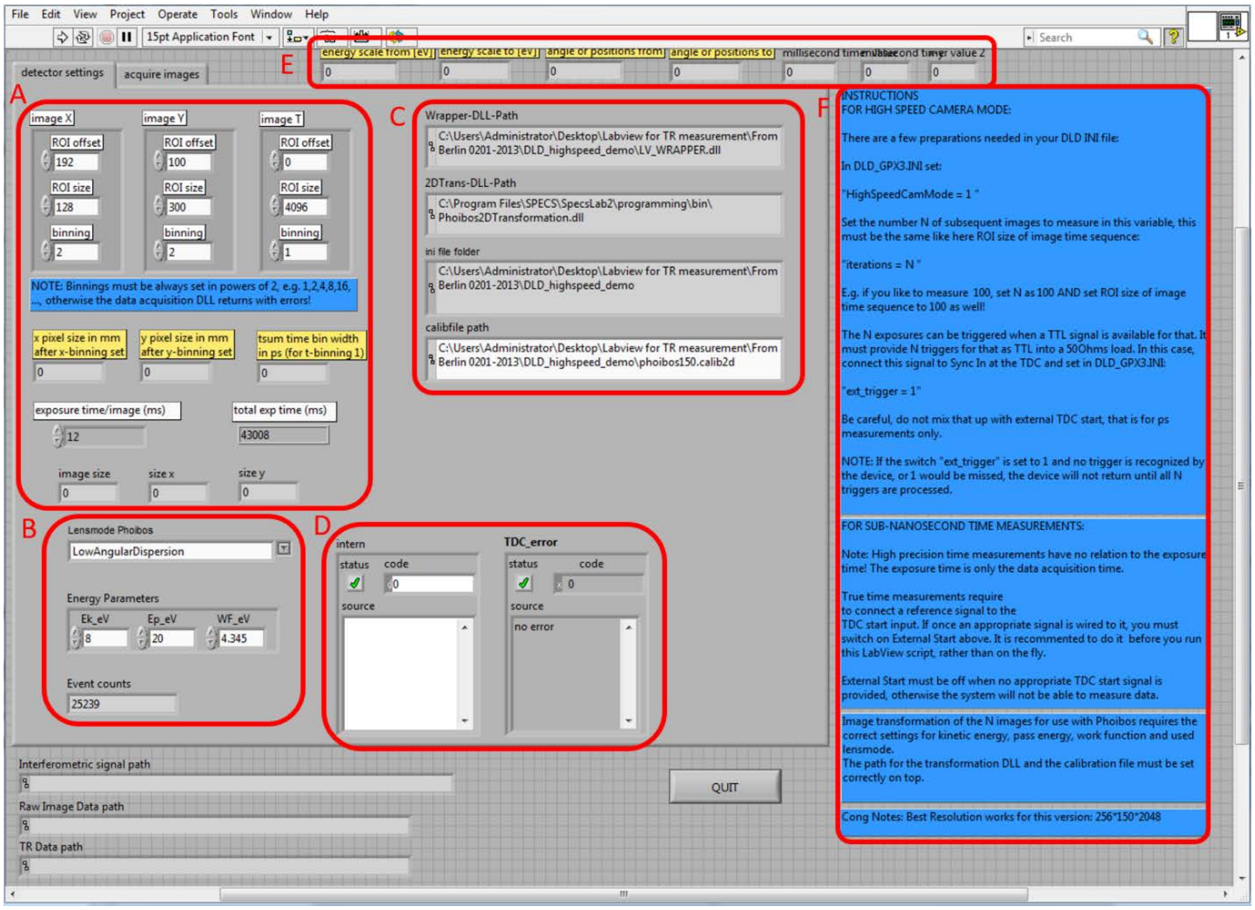

energy scale from [eV]: 0
energy scale to [eV]: 0
angle or positions from: 0
angle or positions to: 0
millisecond timer value: 0
millisecond timer value 2: 0
0

image X: ROI offset 192; ROI size 128; binning 2
image Y: ROI offset 100; ROI size 300; binning 2
image T: ROI offset 0; ROI size 4096; binning 1

NOTE: Binnings must be always set in powers of 2, e.g. 1,2,4,8,16, ..., otherwise the data acquisition DLL returns with errors!

x pixel size in mm after x-binning set: 0
y pixel size in mm after y-binning set: 0
tsum time bin width in ps (for t-binning 1): 0
exposure time/image (ms): 12
total exp time (ms): 43008
image size: 0
size x: 0
size y: 0

Lensmode Phoibos: LowAngularDispersion
Energy Parameters: Ek_eV 8; Ep_eV 20; WF_eV 4.345
Event counts: 25239

Wrapper-DLL-Path: C:\Users\Administrator\Desktop\Labview for TR measurement\From Berlin 0201-2013\DLD_highspeed_demo\LV_WRAPPER.dll
2DTrans-DLL-Path: C:\Program Files\SPECS\SpecsLab2\programming\bin\Phoibos2DTransformation.dll
ini file folder: C:\Users\Administrator\Desktop\Labview for TR measurement\From Berlin 0201-2013\DLD_highspeed_demo
calibfile path: C:\Users\Administrator\Desktop\Labview for TR measurement\From Berlin 0201-2013\DLD_highspeed_demo\phoibos150.calib2d

intern: status ✓; code 0; source
TDC_error: status ✓; code 0; source: no error

Interferometric signal path
Raw Image Data path
TR Data path

INSTRUCTIONS
FOR HIGH SPEED CAMERA MODE:

There are a few preparations needed in your DLD INI file:

In DLD_GPX3.INI set:

"HighSpeedCamMode = 1 "

Set the number N of subsequent images to measure in this variable, this must be the same like here ROI size of image time sequence:

"iterations = N "

E.g. if you like to measure 100, set N as 100 AND set ROI size of image time sequence to 100 as well!

The N exposures can be triggered when a TTL signal is available for that. It must provide N triggers for that as TTL into a 50Ohms load. In this case, connect this signal to Sync In at the TDC and set in DLD_GPX3.INI:

"ext_trigger = 1"

Be careful, do not mix that up with external TDC start, that is for ps measurements only.

NOTE: If the switch "ext_trigger" is set to 1 and no trigger is recognized by the device, or 1 would be missed, the device will not return until all N triggers are processed.

FOR SUB-NANOSECOND TIME MEASUREMENTS:

Note: High precision time measurements have no relation to the exposure time! The exposure time is only the data acquisition time.

True time measurements require
to connect a reference signal to the
TDC start input. If once an appropriate signal is wired to it, you must switch on External Start above. It is recommented to do it before you run this LabView script, rather than on the fly.

External Start must be off when no appropriate TDC start signal is provided, otherwise the system will not be able to measure data.

Image transformation of the N images for use with Phoibos requires the correct settings for kinetic energy, pass energy, work function and used lensmode.
The path for the transformation DLL and the calibration file must be set correctly on top.

Cong Notes: Best Resolution works for this version: 256*150*2048

Appendix Figure 5 Detector settings of the front panel of the 3DCPES collecting VI

Appendix Figure 5 shows the detector settings of the front panel of the 3DCPES collecting VI. It is composed of 6 major function zones marked from A to F. Function Zone A is to configure the range of interest of the whole 3DCPES. Function Zone B is for configuring hardware. Function Zone C is for finding the right dynamic-link library to use the hardware. Function Zone D displays error information. Function Zone E displays information about: energy and angle ranges of 3DCPES, and time elapsed for saving a scanning. Function Zone F is instruction information about how to configure *.ini file to use high speed camera mode of the detector. Function Zone C to F are very intuitive, and do not need to be changed for experiments. Function Zone A and B are zoomed in for a better resolution in Appendix Figure 6.

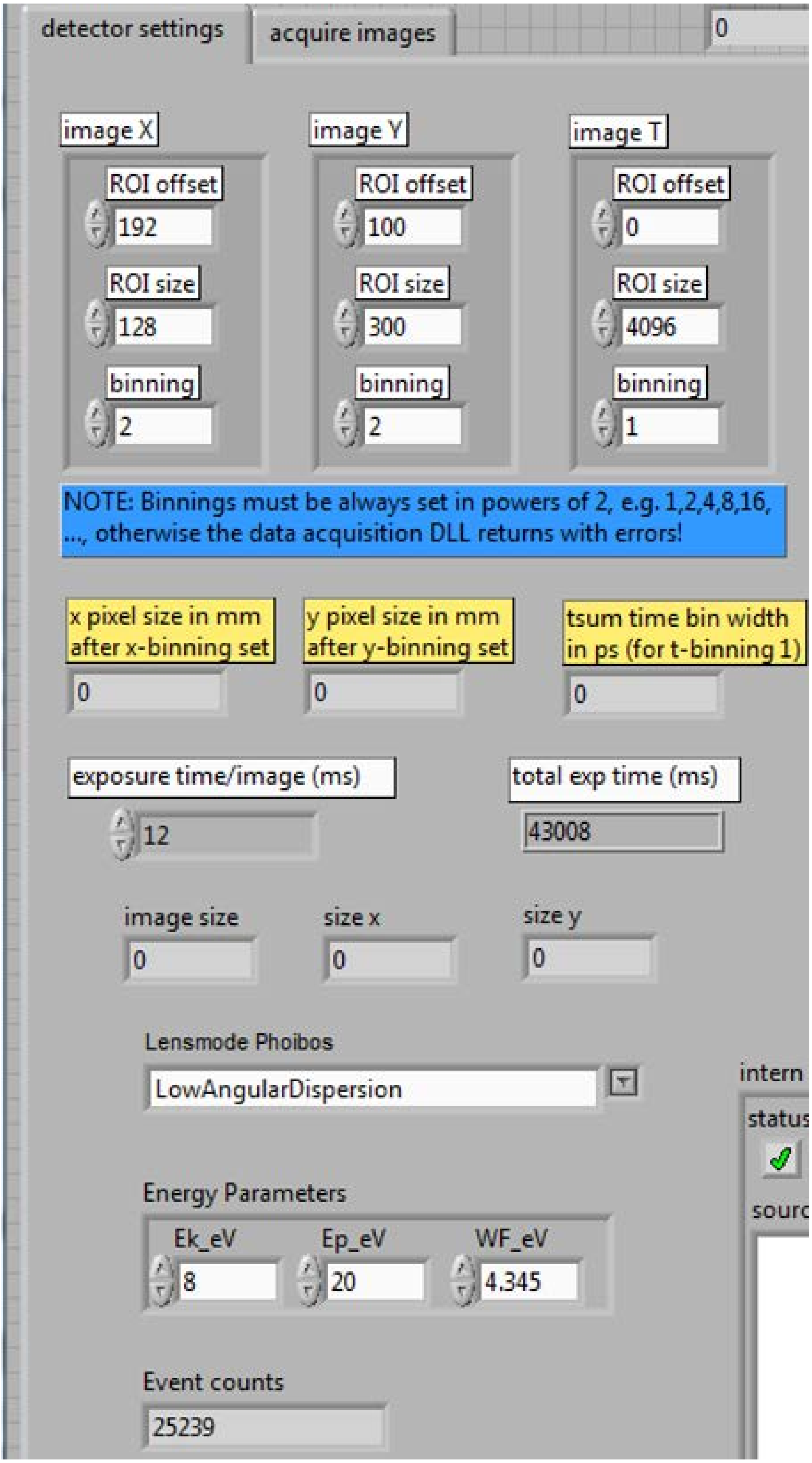

image X

ROI offset 192

ROI size 128

binning 2

image Y

ROI offset 100

ROI size 300

binning 2

image T

ROI offset 0

ROI size 4096

binning 1

NOTE: Binnings must be always set in powers of 2, e.g. 1,2,4,8,16, ..., otherwise the data acquisition DLL returns with errors!

x pixel size in mm after x-binning set 0

y pixel size in mm after y-binning set 0

tsum time bin width in ps (for t-binning 1) 0

exposure time/image (ms) 12

total exp time (ms) 43008

image size 0

size x 0

size y 0

Lensmode Phoibos LowAngularDispersion

Energy Parameters

Ek_eV 8

Ep_eV 20

WF_eV 4.345

Event counts 25239

Appendix Figure 6 Zoomed-in detector settings of the front panel of the 3DCPES collecting VI

In Appendix Figure 6, the top displays 2 tabs marked with detector settings and acquire images. Click on the tab to switch back and forth between detector settings and monitoring acquiring images. Image X, Y and T correspond to energy axis, angle axis, and time axis. The detector pixel resolution is 1024*1024 for energy and angle respectively, with output image pixel resolution 1024*600. We have binned the pixel by 2 to increase signal, and now the whole output image is [1, 512] (a range inclusively from Pixel 1 to Pixel 512) by [101, 400]. For faster saving and processing raw data, we select only a part of the [1, 512] by [101, 400] and stack the images for every time-delay. For example, the configuration displayed in Appendix Figure 6 means that we only collect image from Pixel 193 to Pixel 320 for energy axis, and from Pixel 101 to Pixel 400 for angle axis, which is 128*300 for a single time dely. Then, the energy and angle axis are further binned by 2, and now is an image of 64*150 pixel for a single time delay.

The exposure time in Appendix Figure 6 shall be the same with Appendix Figure 1 and 3. Lensmode Phoibos gives a list of options for different lens mode of the analyzer, and for our experiments, we use WideAngleMode. Energy Parameters let you choose an energy window in which you are interested for the experiments. The larger E_k, the energy axis of your spectra will be centered higher; the large E_p, the range of the energy axis of your spectra will be wider. Work Function (WF) is given by SPECS GmbH for the instrument.

Appendix Figure 7 shows the acquire images tab of the front panel of the 3DCPES collecting VI. Here, fill the Saved file folder text field, give a name of this set of experiment in Measurement text field, then click start acquisition, the program starts to make measurements. In the beginning, the program will create 3 folders under the given folder, two of which are used for store the calibration sine wave, the raw experimental data. The third new folder is for storing processed data. The path of the three folders are shown at the bottom of Appendix Figure 7.

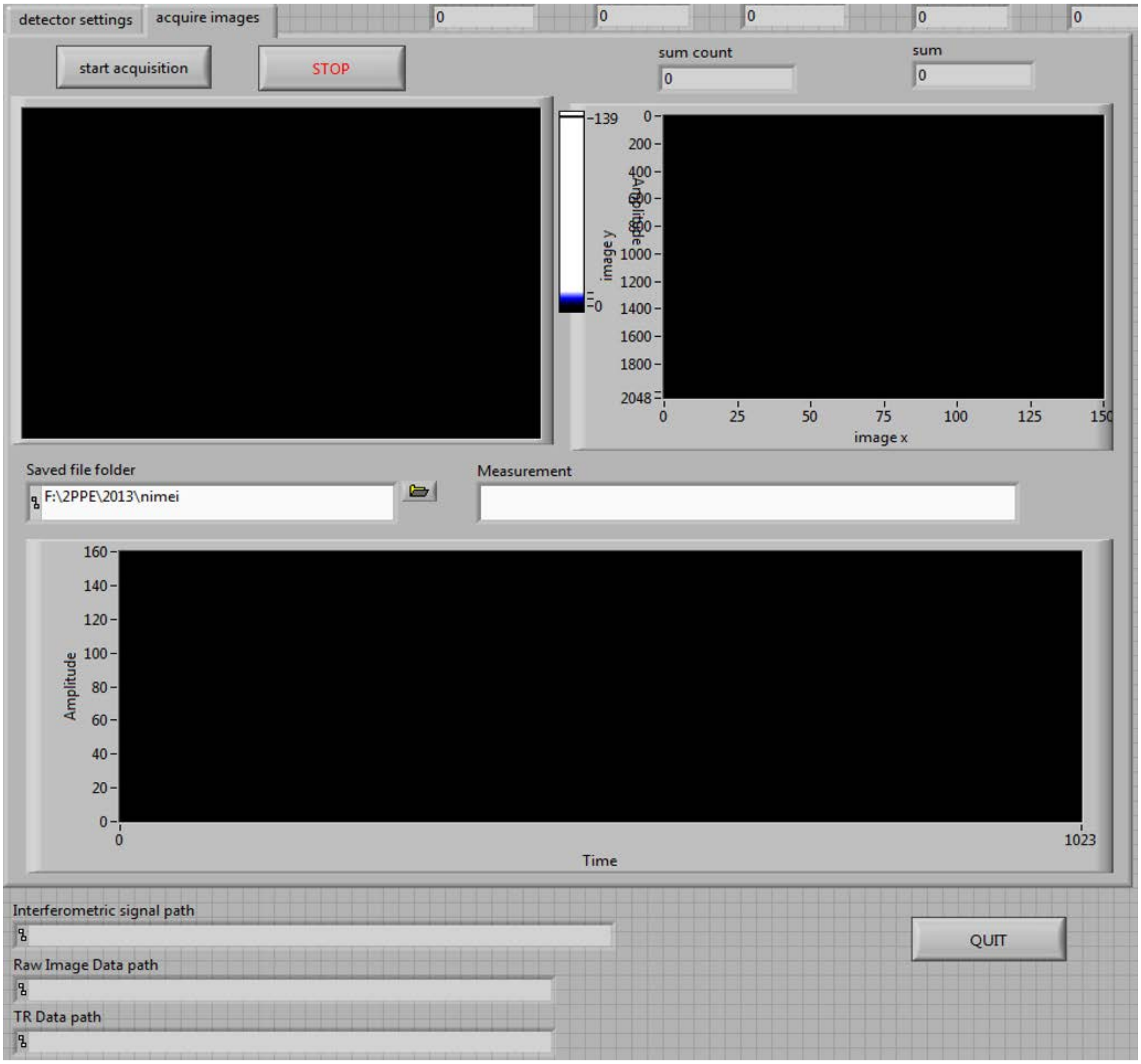

sum count 0

sum 0

Saved file folder F:\2PPE\2013\nimei

Measurement

Interferometric signal path

Raw Image Data path

TR Data path

Appendix Figure 7 Acquire images of the front panel of the 3DCPES collecting VI

The left top monitor of the Appendix Figure 7 shows the image of counts distributed in the angle and energy axes while each scan of the 3DCPES is summed over the time axis. The right top monitor shows the image of counts distribution in the time and energy axes while the angle axis is summed across for each scan. The bottom monitor shows the curve of counts vs time when each scan of the 3DCPES is summed over both energy and angle axes. These monitors help to find problems in an early stage during the experiments.

The block diagram of the 3DCPES collecting VI is a large stacked sequence composed of 3 parts. Part 0 of the stacked sequence: find the binary library folders which are used to operate the detector, and exit if not found. Part 1: call the binary library and boot the detector. Part 2: collect the 3DCPES. The first two parts are shown in Appendix Figure 8 & 9. Part 2 is a large event structure inside a while loop, which follows a diagram calls the binary library to stop detector and quit the program. An event structure means a particular part of program will run if a corresponding event occurs. These events are shown in Appendix Figure 10.

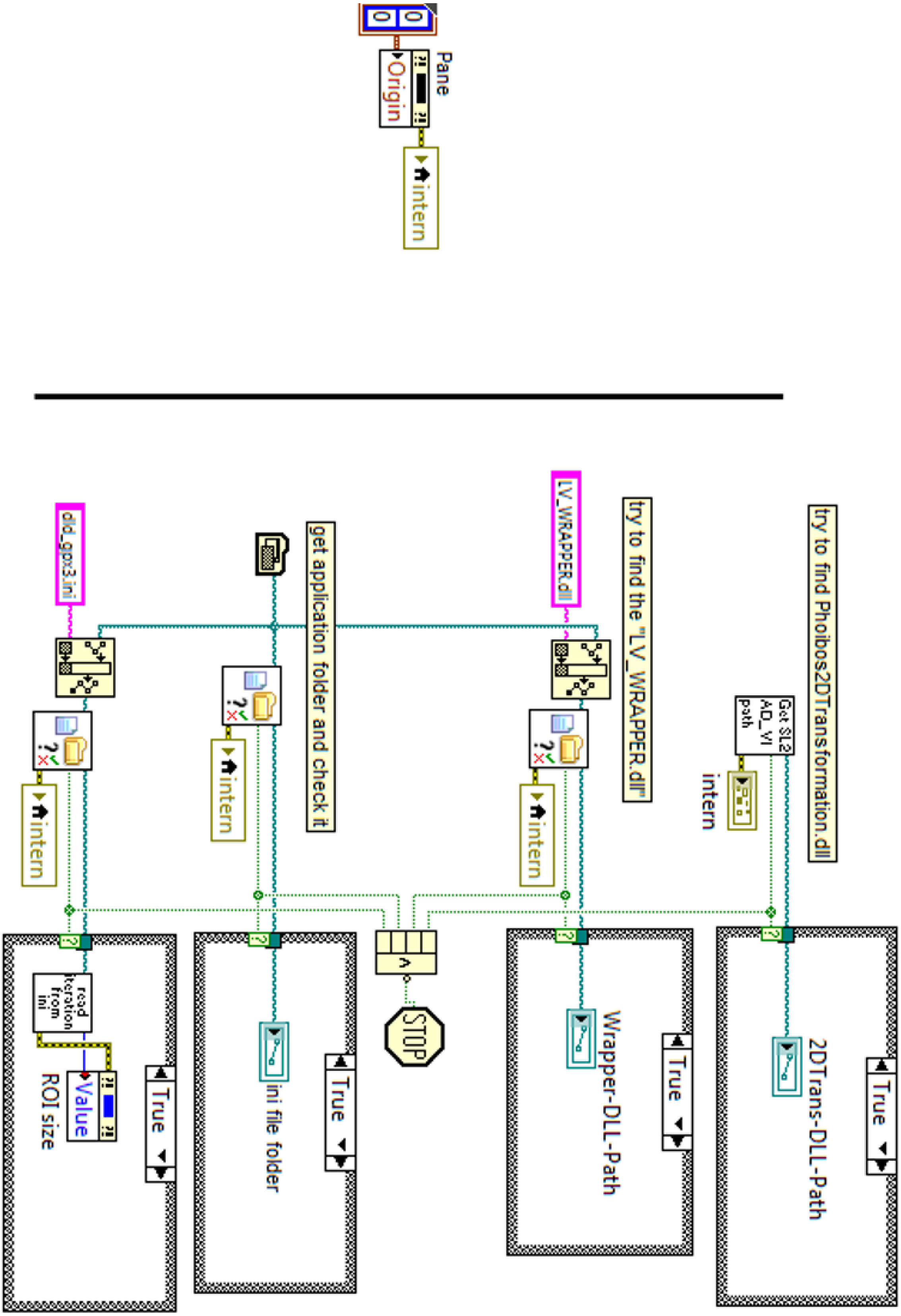

Appendix Figure 8 Find binary folder

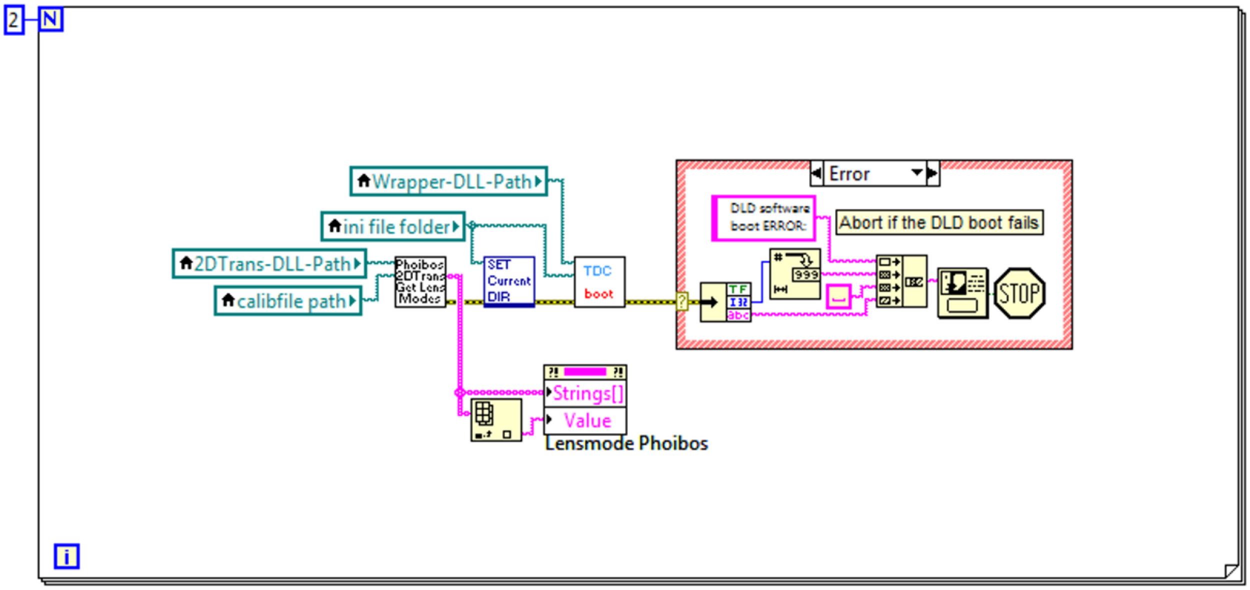

Appendix Figure 9 Boot dector

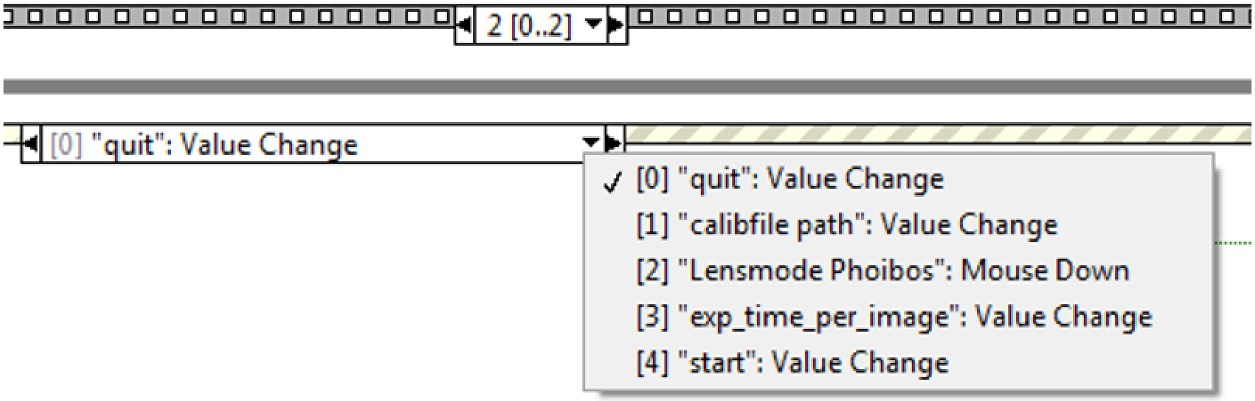

Appendix Figure 10 Events in the event structure

The Event 0 is that you hit the quit button on the front panel, and when Event 0 occurs, the diagram associated does nothing but stop the loop, then program will stop detector and quit. The Event 1 is that the value of calibration file path changes, and associated behavior is to re-find the binary library and call the library to control the detector. The calibration file path is in Section C of Appendix Figure 5. The Event 1 diagram is shown in Appendix Figure 11. The Event 2 is clicking the Lensmode Phoibos pop-up menu, and when this event occurs, a menu showing all lens mode pops out. The Event 3 is changing the value of the exposure time box, which is shown in Appendix Figure 6, and the associated behavior is to update the total exposure time. The Event 4 is clicking the start button, which is shown in Appendix Figure 7. The diagrams in the Event 4 is complex, and is shown in Appendix Figure 12.

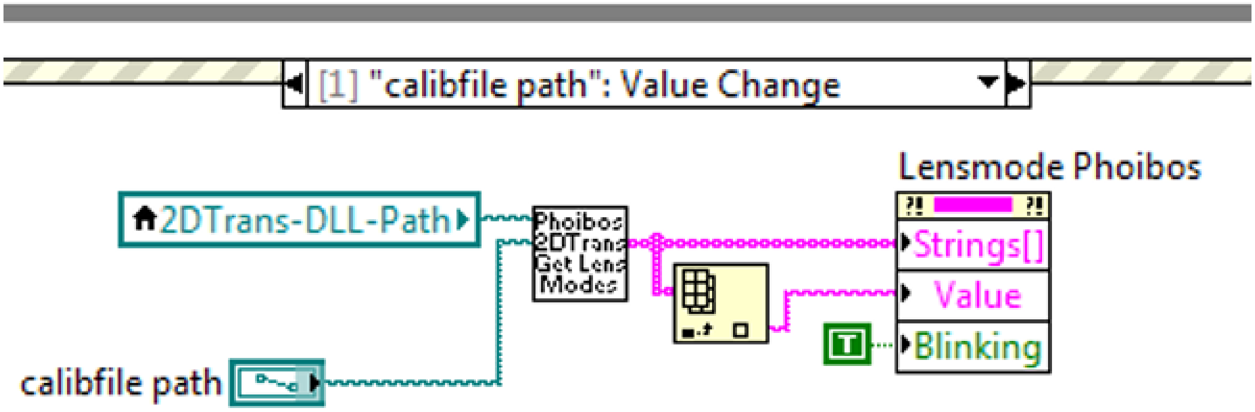

Appendix Figure 11 Event 1: calibration file path changes

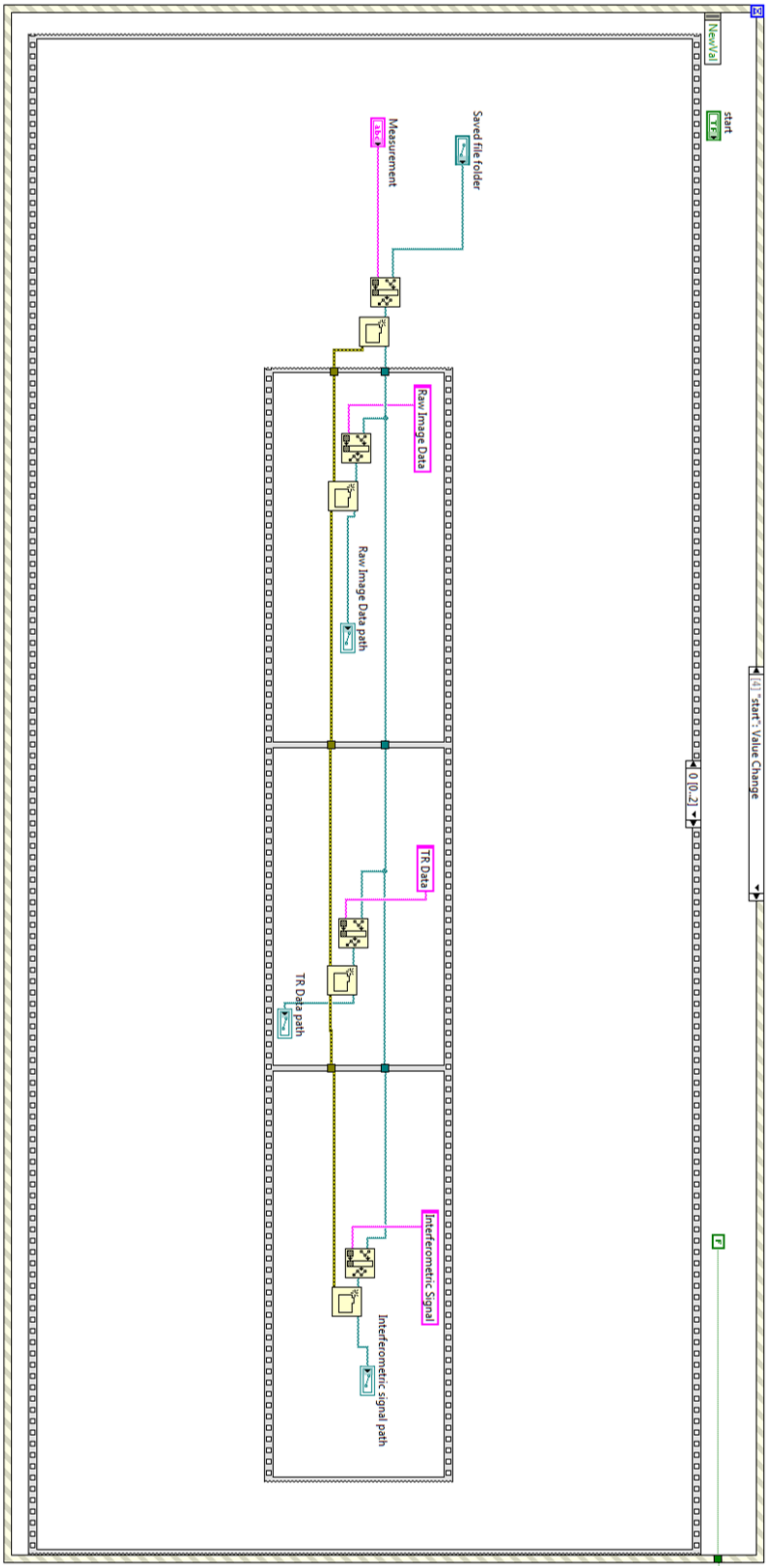

Appendix Figure 12 Event 4: create file folders

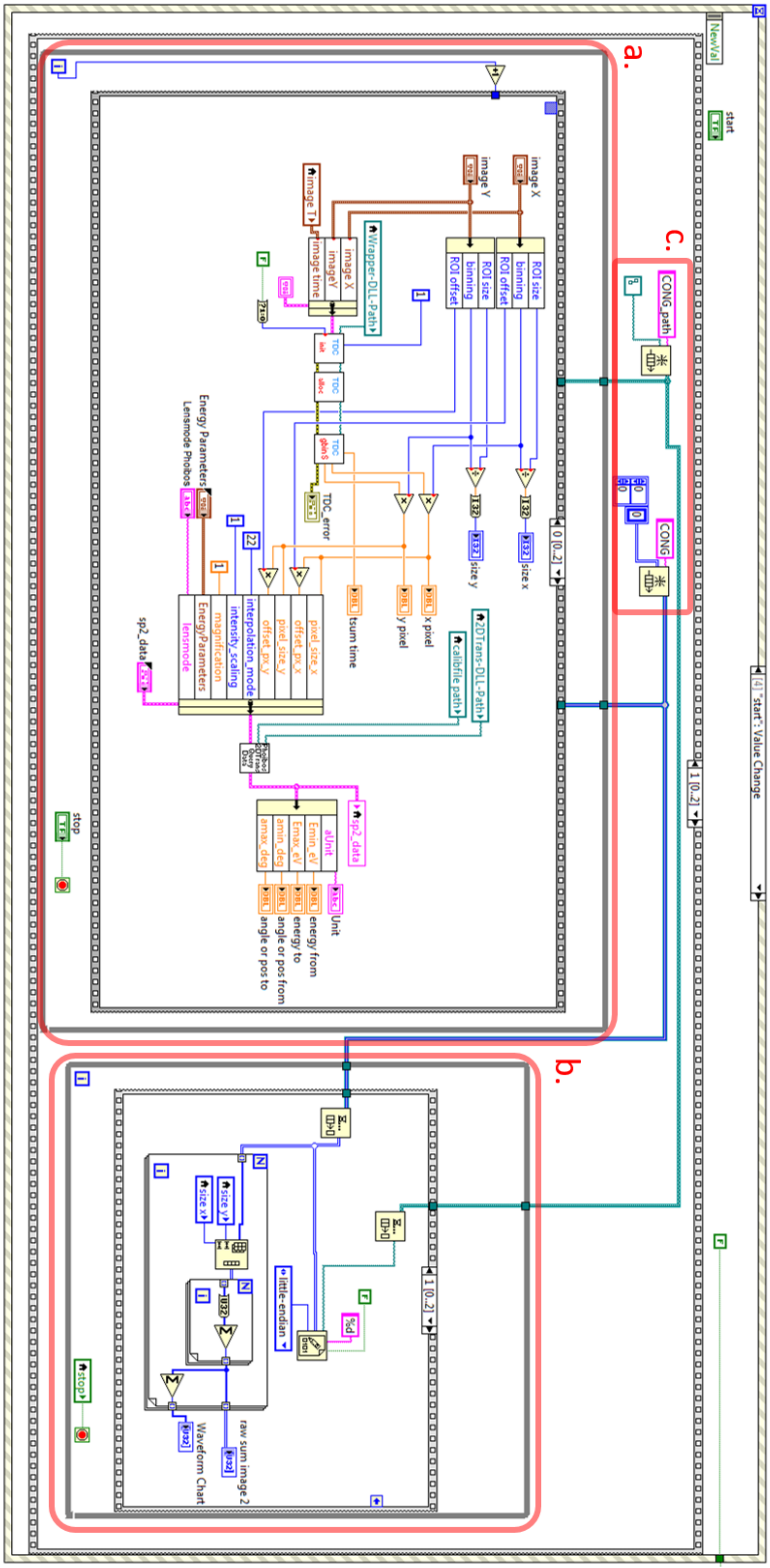

Appendix Figure 13 Event 4: collecting data

The diagrams for Event 4 is a stack sequence composed of 3 in-order actions.

The zeroth thing, illustrated in Appendix Figure 12, is to create 3 folders to store the raw data, and those folder paths are displayed at the bottom of Appendix Figure 7.

The first thing, illustrated in Appendix Figure 13, is to obtain data, and save data. In Appendix Figure 13, Region A is to read data, Region B is to write data, and Region C helps handle data and file names. Region A is a loop, it runs one iteration for one scanning of 3DCPES. Inside the loop, there is a stacked sequence. Sequence 0, is shown in Appendix Figure 13 Region A, and it is calling binary library of detector. Sequence 1 gets the address of the 3DCPES, and pass the address to Sequence 2. Sequence 2 read images from the address and pass data to a heap in Region C, and also creates file path and put it in a file path heap in Region C. Sequence 1 & 2 are shown in Appendix Figure 14. Region B is also a stacked sequence, shown in Appendix Figure 13. The Sequence 0 and Sequence 2 of Region B are to get time stamps and calculate the time consumed for writing data into file, which are shown in Appendix Figure 15, while Sequence 1 is to use data and file paths stored in the data heap and the file path heap from Region C to write data. It helps the stability of the program in separating data fetching and data writing into Region A and Region B.

The second thing for Event 4, is writing some configuration information for a particular single measurement, which is shown in Appendix Figure 16.

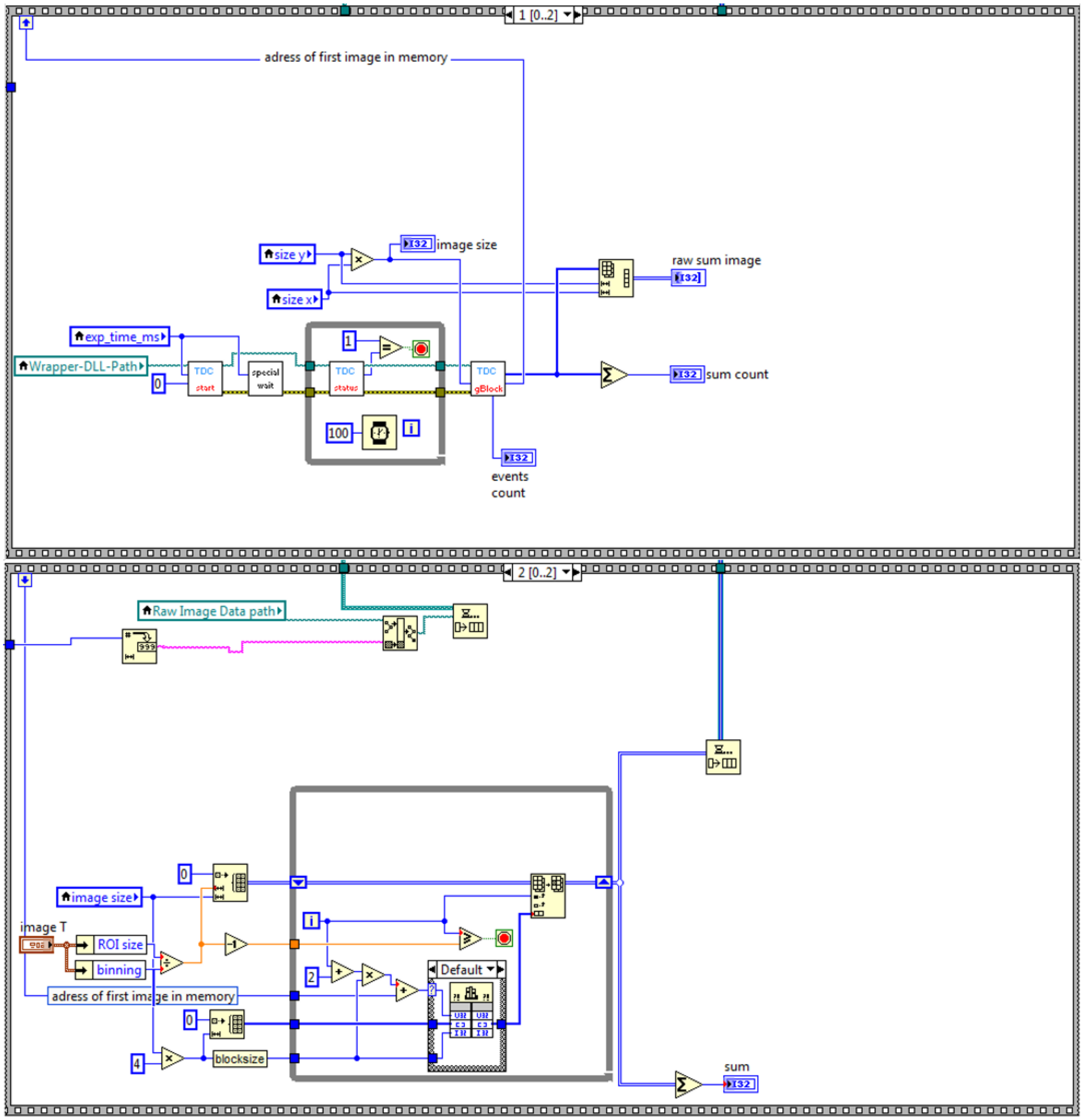

Appendix Figure 14 Sequence 1 & 2 getting one scanning 3DCPES data

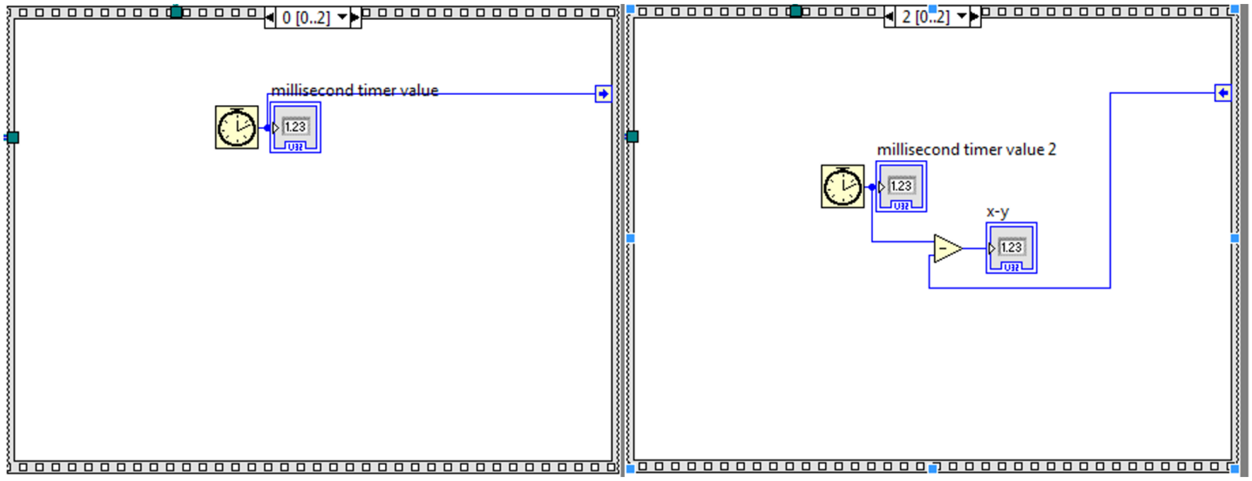

Appendix Figure 15 Calculate file writing time

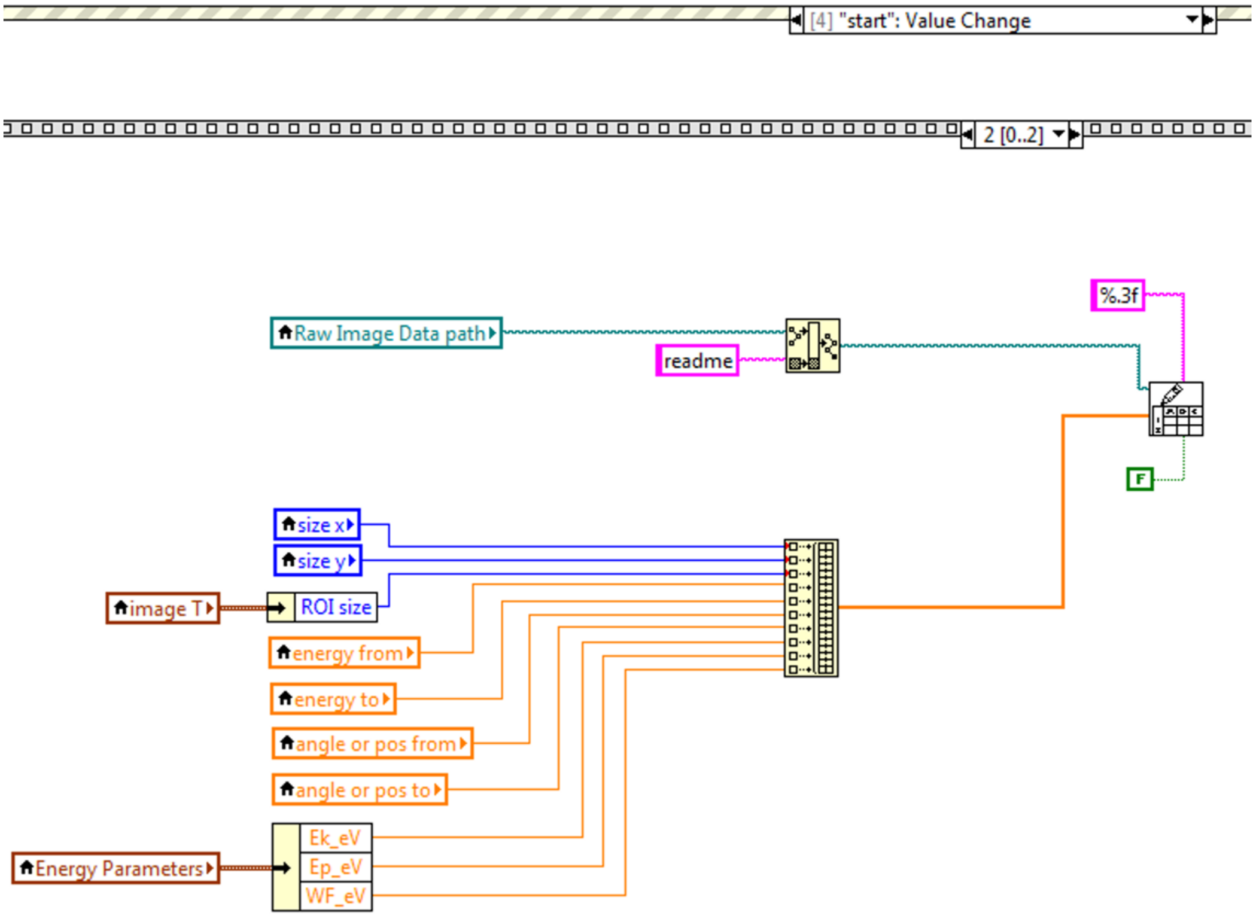

Appendix Figure 16 Saving configuration

BIBLIOGRAPHY

1. Timm, C. & Bennemann, K. H. Response theory for time-resolved second-harmonic generation and two-photon photoemission. *J. Phys. Condens. Matter* **16,** 661–694 (2004).

2. Huber, R. *et al.* How many-particle interactions develop after ultrafast excitation of an electron-hole plasma. *Nature* **414,** 286–9 (2001).

3. Silkin, V. M., Kazansky, a K., Chulkov, E. V & Echenique, P. M. Time-dependent screening of a point charge at a metal surface. *J. Phys. Condens. Matter* **22,** 304013 (2010).

4. Ogawa, S., Nagano, H. & Petek, H. Optical decoherence and quantum beats in Cs/Cu(111). *Surf. Sci.* **427–428,** 34–38 (1999).

5. Petek, H., Nagano, H. & Ogawa, S. Hole Decoherence of d Bands in Copper. *Phys. Rev. Lett.* **83,** 832–835 (1999).

6. Ueba, H. & Gumhalter, B. Theory of two-photon photoemission spectroscopy of surfaces. *Prog. Surf. Sci.* **82,** 193–223 (2007).

7. Petek, H., Nagano, H. & Ogawa, S. Hot-electron dynamics in copper revisited: The d-band effect. *Appl. Phys. B Lasers Opt.* **68,** 369–375 (1999).

8. Gumhalter, B. Transient interactions and coherent motion of optically excited electron–hole pairs in the image potential states at metal surfaces. *Surf. Sci.* **518,** 81–103 (2002).

9. Ogawa, S. & Petek, H. Femtosecond dynamics of hot-electron relaxation in Cu(110) and Cu(100). *Surf. Sci.* **357–358,** 585–594 (1996).

10. Schmuttenmaer, C. A. *et al.* Time-resolved two-photon photoemission from Cu(100): Energy dependence of electron relaxation. *Phys. Rev. B* **50,** 8957–8960 (1994).

11. Nessler, W. *et al.* Energy relaxation and dephasing times of excited electrons in Bi2Sr2CaCu2O8+δ from interferometric 2-photon time-resolved photoemission. *J. Electron Spectros. Relat. Phenomena* **88–91,** 495–501 (1998).

12. Ogawa, S., Nagano, H. & Petek, H. Phase and Energy Relaxation in an Antibonding Surface State : Cs .¯1931–1934 (1999).

13. Knoesel, E., Hotzel, a. & Wolf, M. Ultrafast dynamics of hot electrons and holes in copper: Excitation, energy relaxation, and transport effects. *Phys. Rev. B* **57,** 12812–12824 (1998).

14. Timm, C. & Bennemann, K. H. Response theory for time-resolved second-harmonic generation and two-photon photoemission. *J. Phys. Condens. Matter* **16,** 661–694 (2004).

15. Knorren, R., Bouzerar, G. & Bennemann, K. Theory for transport and temperature effects on two-photon photoemission: Application to Cu. *Phys. Rev. B* **63,** 1–6 (2001).

16. Zaitsev, N. L., Nechaev, I. A., Echenique, P. M. & Chulkov, E. V. Transformation of the Ag(111) surface state due to molecule-surface interaction with ordered organic molecular monolayers. *Phys. Rev. B - Condens. Matter Mater. Phys.* **85,** 1–8 (2012).

17. Petek, H. Photoexcitation of adsorbates on metal surfaces: One-step or three-step. *J. Chem. Phys.* **137,** 0–11 (2012).

18. Onda, K., Li, B. & Petek, H. Two-photon photoemission spectroscopy of TiO2(110) surfaces modified by defects and O2 or H2O adsorbates. *Phys. Rev. B - Condens. Matter Mater. Phys.* **70,** 1–11 (2004).

19. Petek, H., Nagano, H., Weida, M. J. & Ogawa, S. Quantum Control of Nuclear Motion at a Metal Surface. *J. Phys. Chem. A* **104,** 10234–10239 (2000).

20. Long, R. & Prezhdo, O. V. Instantaneous generation of charge-separated state on TiO2 surface sensitized with plasmonic nanoparticles. *J. Am. Chem. Soc.* **136,** 4343–4354 (2014).

21. Pfeiffer, W., Kennerknecht, C. & Merschdorf, M. Electron dynamics in supported metal nanoparticles: relaxation and charge transfer studied by time-resolved photoemission. *Appl. Phys. A Mater. Sci. Process.* **78,** 1011–1028 (2004).

22. Petek, H., Nagano, H., Weida, M. J. & Ogawa, S. Surface femtochemistry: Frustrated desorption of alkali atoms from noble metals. *J. Phys. Chem. B* **105,** 6767–6779 (2001).

23. Petek, H., Weida, M. J., Nagano, H. & Ogawa, S. Electronic relaxation of alkali metal atoms on the Cu (111) surface. *Surf. Sci.* **451,** 22–30 (2000).

24. Ashcroft, N. W. & Mermin, N. D. *Solid State Physics*. (Books Cole, 1976).

25. Eckardt, H., Fritsche, L. & Noffke, J. Self-consistent relativistic band structure of the noble metals. *J. Phys. F Met. Phys.* **14,** 97 (1984).

26. Winkelmann, A. *et al.* Direct k-space imaging of Mahan cones at clean and Bi-covered Cu(111) surfaces. *New J. Phys.* **14,** (2012).

27. Unal, A. A. *et al.* Hybridization between the unoccupied Shockley surface state and bulk electronic states on Cu(111). *Phys. Rev. B - Condens. Matter Mater. Phys.* **84,** 13–15 (2011).

28. Shockley, W. On the surface states associated with a periodic potential. *Phys. Rev.* **56,** 317–323 (1939).

29. Search, H., Journals, C., Contact, A., Iopscience, M. & Address, I. P. Image Potential Surface States *. **669,**

30. Goldmann, A., Dose, V. & Borstel, G. Empty electronic states at the (100), (110), and (111) surfaces of nickel, copper, and silver. *Phys. Rev. B* **32,** 1971–1980 (1985).

31. Reinert, F., Nicolay, G., Schmidt, S., Ehm, D. & Hüfner, S. Direct measurements of the L-gap surface states on the (111) face of noble metals by photoelectron spectroscopy. *Phys. Rev. B* **63,** 1–7 (2001).

32. Ünal, A. A. *et al.* Hybridization between the unoccupied Shockley surface state and bulk electronic states on Cu(111). *Phys. Rev. B - Condens. Matter Mater. Phys.* **84,** 13–15 (2011).

33. Giesen, K. *et al.* Effective mass of image-potential states. *Phys. Rev. B* **35,** 975–978 (1987).

34. Ünal, A. A. *et al.* Hybridization between the unoccupied Shockley surface state and bulk electronic states on Cu(111). *Phys. Rev. B - Condens. Matter Mater. Phys.* **84,** 13–15 (2011).

35. Davison, S. G. & Stęślicka, M. *Basic Theory of Surface States*. (Clarendon Press, 1992).

36. Echenique, P. M. & Pendry, J. B. The existence and detection of Rydberg states at surfaces. *J. Phys. C Solid State Phys.* **11,** 2065–2075 (1978).

37. Höfer, U. *et al.* Time-Resolved Coherent Photoelectron Spectroscopy of Quantized Electronic States on Metal Surfaces. *Science (80-.).* **277,** 1480–1482 (1997).

38. Search, H. *et al.* The existence and detection of Rydberg states at surfaces. **2065,** (1978).

39. Echenique, P. M. THEORY OF IMAGE STATES AT METAL SURFACES. **82,** (1990).

40. Echenique, P. M. *et al.* Decay of electronic excitations at metal surfaces. *Surf. Sci. Rep.* **52,** 219–317 (2004).

41. Marks, M., Schwalb, C. H. & Schubert, K. Quantum-beat spectroscopy of image-potential resonances. **245402,** 1–12 (2011).

42. Lingle, R. L., Padowitz, D. F., Jordan, R. E., McNeill, J. D. & Harris, C. B. Two-dimensional localization of electrons at interfaces. *Phys. Rev. Lett.* **72,** 2243–2246 (1994).

43. Reinert, F. & Hüfner, S. Photoemission spectroscopy - From early days to recent applications. *New J. Phys.* **7,** (2005).

44. Gauyacq, J. P. & Kazansky, A. K. Modelling of interferometric multiphoton photoemission. *Appl. Phys. A Mater. Sci. Process.* **89,** 517–523 (2007).

45. Cui, X. *et al.* Transient excitons at metal surfaces. *Nat. Phys.* **10,** 505–509 (2014).

46. Petek, H. & Ogawa, S. Femtosecond time-resolved two-photon photoemission studies of electron dynamics in metals. *Prog. Surf. Sci.* **56,** 239–310 (1997).

47. Argondizzo, A. *et al.* Ultrafast multiphoton pump-probe photoemission excitation pathways in rutile TiO2(110). *Phys. Rev. B - Condens. Matter Mater. Phys.* **91,** 1–10 (2015).

48. Wang, Y. H., Steinberg, H., Jarillo-Herrero, P. & Gedik, N. Observation of Floquet-Bloch States on the Surface of a Topological Insulator. *Science (80-.).* **342,** 453–457 (2013).

49. Homann, C., Schriever, C., Baum, P. & Riedle, E. Octave wide tunable UV-pumped NOPA: pulses down to 20 fs at 0.5 MHz repetition rate. *Opt. Express* **16,** 5746–5756 (2008).

50. Pontius, N., Sametoglu, V. & Petek, H. Simulation of two-photon photoemission from the bulk sp-bands of Ag(111). *Phys. Rev. B - Condens. Matter Mater. Phys.* **72,** 1–9 (2005).

51. Damascelli, A. Probing the Electronic Structure of Complex Systems by ARPES. *Phys. Scr.* **T109,** 61–74 (2003).

52. Liu, H., Yao, J., Ashok, P. & Puri, A. Second and third harmonic generation in BBO by femtosecond Ti:sapphire laser pulses. *Opt. Commun.* **109,** 139–144 (1994).

53. Demtröder, W. *Laser Spectroscopy*. (Springer, 2014). doi:10.1007/978-3-540-73418-5

54. Chulkov, E. V., Silkin, V. M. & Echenique, P. M. Image potential states on metal surfaces: Binding energies and wave functions. *Surf. Sci.* **437,** 330–352 (1999).

55. Fattal, E. The Mapped Fourier Grid Method in Electron-Nuclear Quantum Dynamics. *Ph. D. Thesis* (1996).

56. Kokoouline, V., Dulieu, O. & Kosloff, R. Mapped Fourier methods for long-range molecules : Application to perturbations in the Rb 2 (0 u +) photoassociation spectrum Mapped Fourier methods for long-range molecules : Application to perturbations in the Rb 2 „ 0 ⁒ u … photoassociation spectrum. *J. Chem. Phys.* **2,** 9865 (1999).

57. Marston, C. C. & Balint-Kurti, G. G. The Fourier grid Hamiltonian method for bound state eigenvalues and eigenfunctions. *J. Chem. Phys.* **91,** 3571–3576 (1989).

58. Diels, J.-C. & Rudolph, W. *Ultrashort Laser Pulse Phenomena*. (Academic Press, 2006).

59. Ogawa, S., Nagano, H., Petek, H. & Heberle, A. P. Optical Dephasing in Cu(111) Measured by Interferometric Two-Photon Time-Resolved Photoemission. *Phys. Rev. Lett.* **78,** 1339–1342 (1997).

60. Schoenlein, R. W., Fujimoto, J. G., Eesley, G. L. & Capehart, T. W. Femtosecond relaxation dynamics of image-potential states. *Phys. Rev. B* **43,** 4688–4698 (1991).

61. Marks, M., Schwalb, C. H., Schubert, K., Güdde, J. & Höfer, U. Quantum-beat spectroscopy of image-potential resonances. *Phys. Rev. B - Condens. Matter Mater. Phys.* **84,** 1–12 (2011).

62. Hulbert, S. L., Johnson, P. D., Stoffel, N. G. & Smith, N. V. Unoccupied bulk and surface states on Ag(111) studied by inverse photoemission. *Phys. Rev. B* **32,** 3451–3455 (1985).

63. Andres, P. De. two-dimensional image-potential-induced P. **35,** 9–12 (1987).

64. Tsirkin, S. S. *et al.* Temperature dependence of the dynamics of the first image-potential state on Ag(111). *Phys. Rev. B - Condens. Matter Mater. Phys.* **86,** 1–7 (2012).

65. Elliott, R. J. Intensity of optical absorption by excitons. *Phys. Rev.* **108,** 1384–1389 (1957).

66. Hopfield, J. J. Theory of the contribution of excitons to the complex dielectric constant of crystals. *Phys. Rev.* **112,** 1555–1567 (1958).

67. Dresselhaus, G. Absorption Coefficients for Exciton Absorption Lines. *Phys. Rev.* **106,** 76 (1957).

68. Edwards, P. P., Lodge, M. T. J., Hensel, F. & Redmer, R. '... a Metal Conducts and a Non-Metal Doesn'T'. *Philos. Trans. A. Math. Phys. Eng. Sci.* **368,** 941–65 (2010).

69. Li, Y., Luo, X. & Kroger, H. Bound States and Critical Behavior of the Yukawa Potential ∗. *Sci. China Ser. G* **49,** (2006).

70. Mueller, F. M. & Phillips, J. C. Electronic spectrum of crystalline copper. *Phys. Rev.* **157,** 600–607 (1967).

71. Schöne, W.-D. & Edkardt, W. No Title. *Phys. Rev. B* **62,** 13464 (2000).

72. Schöne, W.-D. & Ekardt, W. Transient excitonic states in noble metals and Al. *Phys. Rev. B* **65,** 6–8 (2002).

73. Marini, A. & Sole, R. Del. Dynamical Excitonic Effects in Metals and Semiconductors. 11–14 (2003). doi:10.1103/PhysRevLett.91.176402

74. Gumhalter, B., Lazić, P. & Došlić, N. Excitonic precursor states in ultrafast pump-probe spectroscopies of surface bands. *Phys. Status Solidi Basic Res.* **247,** 1907–1919 (2010).

75. Bisio, F., Winkelmann, a, Chiang, C.-T., Petek, H. & Kirschner, J. Band structure effects

in above threshold photoemission. *J. Phys. Condens. Matter* **23,** 485002 (2011).

76. Harris, F. J. On the use of windows for harmonic analysis with the discrete Fourier transform. *Proc. IEEE* **66,** 51–83 (1978).

77. Yalunin, S., Gulde, M. & Ropers, C. Strong-field photoemission from surfaces: Theoretical approaches. *Phys. Rev. B* **84,** 1–14 (2011).

78. Schafer, K. J., Yang, B., Dimauro, L. F. & Kulander, K. C. Above threshold ionization beyond the high harmonic cutoff. *Phys. Rev. Lett.* **70,** 1599–1602 (1993).

79. Winkelmann, A. *et al.* Higher Order Photoemission from Metal Surfaces. *Dyn. Solid State Surfaces Interfaces* **1,** 33–51 (2010).

80. Fann, W. S., Storz, R. & Bokor, J. Observation of above-threshold multiphoton photoelectric emission from image-potential surface states. *Phys. Rev. B* **44,** 10980–10982 (1991).

81. Petek, H. *et al.* Optical Phase Control of Coherent Electron Dynamics in Metals. *Phys. Rev. Lett.* **79,** 4649–4652 (1997).

82. Winkelmann, A. *et al.* Resonant coherent three-photon photoemission from Cu(001). *Phys. Rev. B - Condens. Matter Mater. Phys.* **80,** 1–9 (2009).

83. Heberle, a. P., Ogawa, S. & Petek, H. Coherent control of electron dynamics in metals. *Tech. Dig. Summ. Pap. Present. Quantum Electron. Laser Sci. Conf.* 4649–4652 (1999). doi:10.1109/QELS.1999.807396

84. Lupke, G., Bottomley, D. J. & Driel, H. M. Van. Resonant second-harmonic generation on Cu(111) by a surface-state to image-potential-state transition. **49,** 15–18 (1994).

85. Wallauer, W. & Fauster, T. Two-photon excitation processes and linewidths of surface and image states on Cu(111). *Surf. Sci.* **374,** 44–50 (1997).

86. Petek, H., Nagano, H., Weida, M. . & Ogawa, S. The role of Auger decay in hot electron excitation in copper. *Chem. Phys.* **251,** 71–86 (2000).

87. Ogawa, S., Nagano, H. & Petek, H. Hot-electron dynamics at Cu(100), Cu(110), and Cu(111) surfaces:mComparison of experiment with Fermi-liquid theory. *Phys. Rev. B* **55,** 10869–10877 (1997).

88. Fuyuki, M., Watanabe, K., Ino, D., Petek, H. & Matsumoto, Y. Electron-phonon coupling at an atomically defined interface: Na quantum well on Cu(111). *Phys. Rev. B - Condens. Matter Mater. Phys.* **76,** 1–5 (2007).

89. Weinelt, M. Time-resolved two-photon photoemission from metal. **1099,**

90. Weida, M. J., Ogawa, S., Nagano, H. & Petek, H. Ultrafast interferometric pump–probe

correlation measurements in systems with broadened bands or continua. *J. Opt. Soc. Am. B* **17,** 1443 (2000).

91. Johnson, P. D. & Smith, N. V. Image-potential states and energy-loss satellites in inverse photoemission spectra. *Phys. Rev. B* **27,** 2527–2530 (1983).

92. Berland, K., Einstein, T. L. & Hyldgaard, P. Response of the Shockley surface state to an external electrical field: A density-functional theory study of Cu(111). *Phys. Rev. B - Condens. Matter Mater. Phys.* **85,** 47–49 (2012).

93. Pagliara, S. *et al.* Angle resolved photoemission study of image potential states and surface states on Cu(111). *Surf. Sci.* **600,** 4290–4293 (2006).

94. Chulkov, E. V., Silkin, V. M. & Echenique, P. M. Image potential states on metal surfaces: binding energies and wave functions. *Surf. Sci.* **437,** 330–352 (1999).

95. Güdde, J., Rohleder, M., Meier, T., Koch, S. W. & Höfer, U. Time-Resolved Investigation of Coherently Controlled Electric Currents at a Metal Surface. *Science (80-.).* **318,** 1287 (2007).

96. Schubert, K. *et al.* Momentum-resolved electron dynamics of image-potential states on Cu and Ag surfaces. *Phys. Rev. B - Condens. Matter Mater. Phys.* **85,** 1–9 (2012).

97. Arimondo, E., Clark, C. W. & Martin, W. C. Colloquium: Ettore Majorana and the birth of autoionization. *Rev. Mod. Phys.* **82,** 1947–1958 (2010).

98. Miroshnichenko, A. E., Flach, S. & Kivshar, Y. S. Fano resonances in nanoscale structures. *Rev. Mod. Phys.* **82,** 2257–2298 (2010).

99. Revie, P. Layer-resolved shifts. **33,** (1986).

100. Mahan, G. D. Collective excitations in x-ray spectra of metals* G. *P Hysica L Rev. B* **11,** 592–609 (1975).

101. Nozières, P. & De Dominicis, C. T. Singularities in the X-ray absorption and emission of metals. III. One-body theory exact solution. *Phys. Rev.* **178,** 1097–1107 (1969).

102. Anderson, P. W. Infrared catastrophe in fermi gases with local scattering potentials. *Phys. Rev. Lett.* **18,** 1049–1051 (1967).

103. Perakis, I. E. & Shahbazyan, T. V. Many-body correlation effects in the ultrafast non-linear optical response of confined Fermi seas. *Surf. Sci. Rep.* **40,** 1–74 (2000).

104. Shabaev, A., Efros, A. L. & Nozik, A. J. Multiexciton Generation by a Single Photon in Nanocrystals. (2006).

105. Chan, W.-L. *et al.* Observing the multiexciton state in singlet fission and ensuing ultrafast multielectron transfer. *Science* **334,** 1541–5 (2011).

106. Huber, R., Tauser, F., Brodschelm, A. & Leitenstorfer, A. Femtosecond buildup of a many-body resonance observed via two-dimensional THz time-domain spectroscopy. *Phys. Status Solidi Basic Res.* **234,** 207–214 (2002).

107. Cui, X. *et al.* Transient excitons at metal surfaces. **10,** 505–509 (2014).

108. Petek, H. Photoexcitation of adsorbates on metal surfaces: One-step or three-step. *J. Chem. Phys.* **137,** (2012).

109. Ogawa, S., Nagano, H. & Petek, H. Phase and Energy Relaxation in an Antibonding Surface State : Cs ¯Cu (111). 1931–1934 (1999).

110. Zhao, J. *et al.* Electronic potential of a chemisorption interface. *Phys. Rev. B* **78,** 1–7 (2008).